Frequency Shifting a Single Photon by Electro-Optic Modulation

by

Michael Kobierski

A thesis
presented to the University of Waterloo
in fulfillment of the
thesis requirement for the degree of
Master of Applied Science
in
Electrical and Computer Engineering (Quantum Information)

Waterloo, Ontario, Canada, 2020

© Michael Kobierski 2020

This thesis consists of material all of which I authored or co-authored: see Statement of Contributions included in the thesis. This is a true copy of the thesis, including any required final revisions, as accepted by my examiners.

I understand that my thesis may be made electronically available to the public.

Statement of Contributions

The content in chapter 3 was adapted from my final project for ECE 672 in Winter 2018, taught by Dayan Ban, with his permission as well as Michael Reimer's, my academic supervisor. Andreas Fognini and Simon Daley had a significant hand in the experimental effort for chapter 4, and I had help from Turner Garrow when collecting the results in chapter 5. The image in Figure 5.1 was taken by Arash Ahmadi. I am the sole author of all the written content in this thesis.

Abstract

Entanglement is a rare resource only a select few people worldwide can create. Its fundamentally non-classical behavior seeds a tree of ideas from which transformative technologies in information processing, communication, and imaging grow. Particularly interesting is entanglement between photons in a pair made by a quantum dot, the most competitive contender among quantum photonic devices.

A strength of semiconductor quantum dots is their deterministic reliability and potential for production at scale. The associated price is anchored in their inherent flaw: sensitivity to imperfections in their shape puts the entanglement they generate in motion. Thus, unless a specific entangled photon pair is caught at just the right moment, it will appear as though it is in fact not entangled at all.

Ingenious methods for making quantum dots perfect again have been devised, almost exclusively built around reshaping the dot by physical, electric, or magnetic means. One completely different proposal stands out, which instead stops the entanglement's motion once it has already been created. As a purely optical technique it can be used for any quantum dot and is completely non-intrusive. This is the method of the rotating half-wave plate [1].

The entanglement between photons in a pair revolves up to a few billion times per second and halting it requires a correction one-half that rate. Physically spinning a crystal waveplate at that tremendous speed is impossible, but if the *properties* of a crystal are spun in an identical way such quickly varying entanglement can be restored to its starting point with ease. This is the principle of electro-optic modulation.

This thesis shows the very first demonstration of slowing the frequency of single photons in a stream by using an electro-optical rotating half-wave plate prototype. Initial results show a reduction in frequency by 127.75 million oscillations per second. Any quantum dot whose entanglement precesses no more quickly than 255.5 MHz can thus directly make use of the technique contained herein.

Acknowledgements

Many people made this thesis possible. First and foremost I'd like to thank Laurence Roy for her unwavering support. My parents Karen and Bob for always believing in me. Michael Reimer, whose fantastic supervision and even better intuition provided me the motivation for a sensational experimental demonstration. Simon Daley, who taught me so much about the way of experimental research in physics and engineering. Nachiket and Morgan for brain-expanding lunchroom conversations. Brad for the relaxed vibe in our shared office space. Arash and Zeeshan for the always trustworthy guidance. Turner for patient and dependable help. Sara for saving me on the weekend when I locked my keys in the lab. Lin and François for the encouragement and lab-schedule flexibility.

Pam, thank you for your guidance and support from before the beginning of my degree right through its completion. Also to Mathieu Walsh Moreau, Tommy Labbé, and Pier-Luc Moreau, you guys are great.

Dedication

To Laurence, whose joy and good company enriched the Waterloo experience.

Table of Contents

List of Tables

List of Figures

Abbreviations

GaAs gallium arsenide 26, 27

InAsP indium arsenide phosphide 26, 27

InAs indium arsenide 26, 27

InP indium phosphide 26, 27

AC alternating current 74, 78

APD avalanche photodiode 102, 104, 105, 107, 112, 114, 116

CCD charge coupled device 94, 99, 100, 103–105, 116

CPS counts per second 31, 100

DAC digital-to-analog converter 86, 114

DBR distributed Bragg reflector 31, 32

DC direct current 74, 78, 83, 90

EOM electro-optic modulator 69, 70, 73–75, 78–80, 83, 85–88, 90, 92–101, 103, 105–107, 111, 114, 116

FP Fabry-Perot 75, 83, 84, 86, 90, 98, 100, 102–105, 107, 109, 112, 116, 117

FSR free spectral range 75, 84, 90, 102, 107, 109, 117

FSS fine structure splitting 48, 102, 105–107, 109–112, 117

HBT Hanbury Brown–Twiss 27, 28, 34, 35, 37, 38

HOM Hong–Ou–Mandel 39, 40

HWP half-wave plate 2, 74, 78, 106, 107, 112

LOQC linear optical quantum computing 39

MFD mode field diameter 76, 94, 97

NA numerical aperture 76, 94, 95

NV nitrogen vacancy 22–25, 43

OSLO Optics Software for Layout and Optimization 96, 97

PBS polarizing beam splitter 74, 83, 90, 106, 107, 112

QD quantum dot 27, 34, 43, 74, 93–96, 102, 111

QWP quarter-wave plate 74, 90, 112

RF radio frequency 24

SIL solid immersion lens 32

SPDC spontaneous parametric down-conversion 30

WD working distance 95

Chapter 1

Introduction: Quantum Information and Entanglement

Light is a physical phenomenon abundant in daily life, often taken for granted without a further thought yet laden with clues about our universe which the curious can endlessly explore. Its intriguing nature has captured significant attention from thinkers seeking to characterize the sense of sight: Euclid's *Optics* circa 300 BC was perhaps the first mathematical treatment on the subject. A progression of understanding led scientists to two central and seemingly incompatible theories, and concurrently contributed to creations like magnifying telescopes and cameras.

The first theory is founded on the idea that light is composed of particles, and was supported by Newton in his 1704 book *Opticks*. The competing theory presents light as wave-like, which Huygens elaborates in the 1690 publication of *Traité de la Lumière*. Support for the two theories was divided, and as experimental observations of interference emerged from Young's double-slit experiment in 1801, an impossibility if light were made of particles, the wave theory gained wider acceptance. The competing theories would not be reconciled until the emergence of a quantum theory for light in the early 1900s. Therein, indivisible photons, the "particles" or quanta of light energy proposed by Einstein [2], also exhibit wave behavior.

Before the quantum theory was formed, though, Maxwell bolstered the wave theory of

light when his work on electromagnetism led him to determine electromagnetic waves can propagate self consistently, and at a calculated speed in agreement with measured values for the speed of light [3]. Visible light, fundamental for sight, is then a specific range of frequencies of electromagnetic radiation that human vision perceives as colors, showing there is a deeper relationship between electricity, magnetism, and light than initially meets the eye. Indeed, Maxwell's equations are directly responsible for phenomenal advances in electrical engineering like wireless radio communication and electric motors.

This thesis gives experimental proof of a new way to change the color of single photons in a precise and tunable manner using electricity, bringing together electrical engineering from Maxwell, optics from Newton and Huygens, and quantum principles from Einstein. The technique can be applied universally to any photon making it super, positioning it as an integral tool in the quantum mechanic's toolbox. Of particular relevance is a proposal that uses the color conversion here demonstrated to freeze the entanglement between two photons to a most desirable and high-quality reference state [1], thereby delivering abundant and reliable on-demand quantum entanglement as a resource, for which no current satisfactory solution exists. Cutting-edge revolutionary technologies for which entanglement is a prerequisite will then be made feasible.

The five chapters which follow build the background and framework for the climactic result just described. The reader will find an overview of the field of quantum information in this chapter, including an introduction to qubits and motivation for entanglement. Chapter 2 follows with a foray into the field of nanowire quantum dots, whence entangled photon pairs emerge. A change of pace in chapter 3 reviews electrically induced alterations in the optical properties of crystals, with specific focus on the necessary conditions for creating a rotating half-wave plate (HWP) with lithium niobate ($LiNbO_3$). The theory is then put to the test in chapter 4, where frequency shifting is evidenced with experimental observations showing 92% conversion efficiency. Finally, a complete assembly combining the critical components results in conclusive data corroborating the color change challenge in chapter 5.

1.1 The Qubit

The launch point for a discussion on quantum information is necessarily the qubit. With a name as imagination-inciting as it is descriptive, the qubit, or quantum bit, builds on the classical concept most familiar in the digital age. Where a classical bit represents a yes or a no, a 1 or a 0, qubit can represent the same, with a $|1\rangle$ and $|0\rangle$ state holding the yes-or-no information. The $|x\rangle$ notation represents a quantum state with the label x, and can be thought of as a vector. The notation will be used throughout this chapter, with examples demonstrating its usage.

The qubit is more complex than, and arguably more capable than a classical bit is, for any one qubit can also represent information "between" $|1\rangle$ and $|0\rangle$. A unique property about information stored in a quantum way is the necessity of explicitly considering measurement as part of the process: an answer becomes definite when it is inquired of.

Starting simply, in the case of the $|1\rangle$ qubit prepared over and over, every measurement will always come back "yes" for a one will be found. Conversely, a zero will always appear when looking at a $|0\rangle$ qubit. In our quantum computer holding a qubit with something that is not exactly a $|1\rangle$ nor a $|0\rangle$ we will still be limited to measuring only one or zero in any single measurement.

Determining a qubit state precisely when it is prepared to some specific intermediate value as we are imagining requires repeatedly measuring and collecting the findings into a table. As more trials are recorded, a clear trend will begin to emerge, for example that the value 1 appears 64 out of every 100 trials, while the other 36 give a zero. Logically, with this information in hand we can determine we must be dealing with a process probabilistic in nature.

The qubit just described could be given a name a and written mathematically as

$$|a\rangle = \frac{8}{10}|1\rangle + \frac{6}{10}|0\rangle. \tag{1.1}$$

Each of $|1\rangle$ and $|0\rangle$ has a coefficient called a probability amplitude that, when squared, gives their observed probabilities of 0.64 ($^{64}/_{100}$) and 0.36 ($^{36}/_{100}$) respectively. Also, as a sanity check, the sum of the two is exactly unity, meaning we never measure something

other than zero or one. Confusingly, the same observed distribution of results would be found by applying the above rule for a different state b written as

$$|b\rangle = \frac{8}{10}|1\rangle - \frac{6}{10}|0\rangle$$

since squaring $^{-6}/_{10}$ equally gives a probability of $^{36}/_{100}$.

This begs the following question: if only ones and zeros can be found upon measurement of $|a\rangle$ or $|b\rangle$ and their statistics are identical, is there any way to distinguish one from the other? The answer is affirmative, and the remarkable result uniquely quantum. The next section establishes some mathematics and visualizations for imagining qubit states that will help answer the question. Following that, subsection 1.1.2 describes probability amplitudes and their relationship to measurement probabilities more rigorously, going beyond the simplified scenario just described.

1.1.1 Poincaré Sphere

So far, the qubit has been discussed in the abstract, and most textbooks on quantum information continue as such. This thesis is about experimentation, though, so here is the perfect opportunity to position the photon as an implementation for a qubit. Whereas photons have many degrees of freedom in which to express quantum information, we will only consider encoding information in polarization.

The polarization of a photon describes its direction of electric field as it propagates through space. A convention must be chosen, so throughout this thesis an electric field that remains parallel to the floor is called horizontal, while the vertical polarization points up and down. A qubit's $|0\rangle$ and $|1\rangle$ states can be mapped from the photon's polarization as

$$|H\rangle \mapsto |0\rangle, \qquad |V\rangle \mapsto |1\rangle.$$

A measurement is done by passing the photon qubit through a polarizing filter followed by a single photon detector. For example, setting the polarizer such that it only passes light with an electric field oriented in the horizontal direction $|H\rangle$ means a detector click will tell us we measured a zero. Under ideal conditions, the absence of a click means we

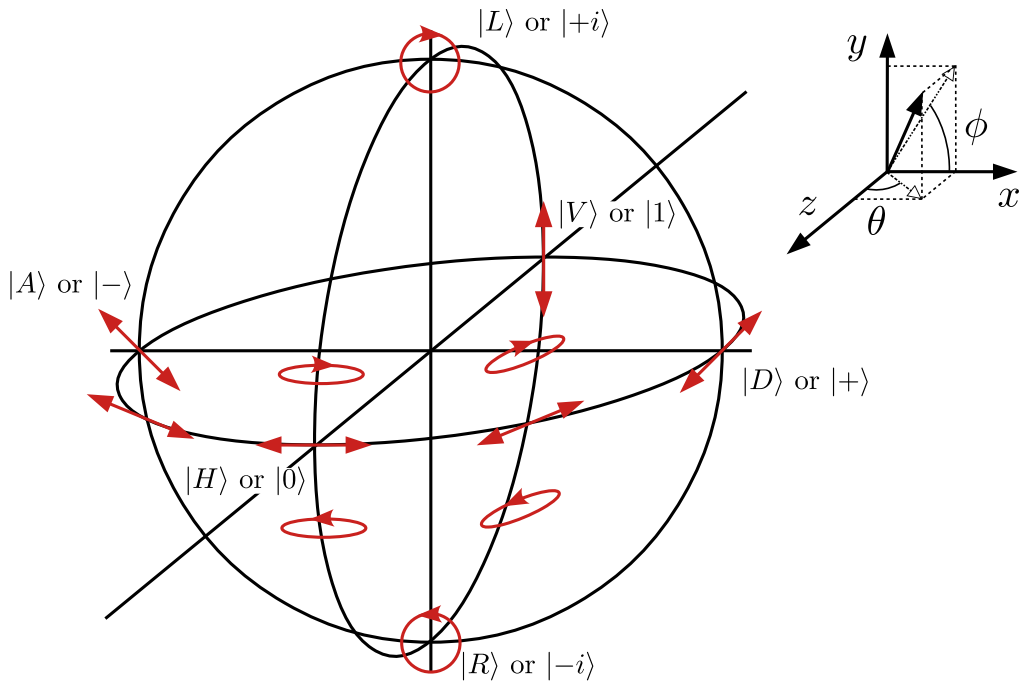

Figure 1.1: The Poincaré sphere pictured with various polarizations and their associated qubit representations.

measured a one. We could equivalently have set the polarizer so it passes the vertical polarization $|V\rangle$ such that a click instead represents measuring a one.

Returning to the example of $|a\rangle$ and $|b\rangle$, each can be written in terms of polarization as

$$|a\rangle = \frac{6}{10}|H\rangle + \frac{8}{10}|V\rangle, \qquad |b\rangle = -\frac{6}{10}|H\rangle + \frac{8}{10}|V\rangle.$$

Each of $|a\rangle$ and $|b\rangle$ now looks like a linear combination of horizontal and vertical polarizations. Indeed, $|H\rangle$, $|V\rangle$, and any other general qubit state $|\psi\rangle$ are in fact unit vectors in a two-dimensional space, and follow the familiar rules of linear algebra. The notation $|\cdot\rangle$ is called a *ket* and was popularized by Dirac. It is conventional to choose the kets $|H\rangle$ and $|V\rangle$ as the basis vectors

$$|H\rangle = \begin{bmatrix} 1 \\ 0 \end{bmatrix}, \qquad |V\rangle = \begin{bmatrix} 0 \\ 1 \end{bmatrix},$$

which are orthogonal and normalized to a length of 1.

A different orthonormal basis could equally be chosen for the two dimensional vector space, such as the vectors

$$|D\rangle = \frac{1}{\sqrt{2}}\begin{bmatrix} 1 \\ 1 \end{bmatrix} = \frac{1}{\sqrt{2}}\left(\begin{bmatrix} 1 \\ 0 \end{bmatrix} + \begin{bmatrix} 0 \\ 1 \end{bmatrix}\right) = \frac{1}{\sqrt{2}}\left(|H\rangle + |V\rangle\right),$$
$$|A\rangle = \frac{1}{\sqrt{2}}\begin{bmatrix} 1 \\ -1 \end{bmatrix} = \frac{1}{\sqrt{2}}\left(\begin{bmatrix} 1 \\ 0 \end{bmatrix} - \begin{bmatrix} 0 \\ 1 \end{bmatrix}\right) = \frac{1}{\sqrt{2}}\left(|H\rangle - |V\rangle\right).$$

The two states $|D\rangle$ and $|A\rangle$ represent diagonal and anti-diagonal polarizations where the diagonal polarization is rotated positively from horizontal by 45°. The associated abstractly-named qubit vectors are $|+\rangle$ and $|-\rangle$ for obvious reason, thus

$$|D\rangle \mapsto |+\rangle = \frac{1}{\sqrt{2}}\left(|0\rangle + |1\rangle\right), \qquad |A\rangle \mapsto |-\rangle = \frac{1}{\sqrt{2}}\left(|0\rangle - |1\rangle\right).$$

One can reverse the relationship and instead write $|H\rangle$ and $|V\rangle$ in terms of $|D\rangle$ and $|A\rangle$

$$|H\rangle = \frac{1}{\sqrt{2}}\left(|D\rangle + |A\rangle\right), \qquad |V\rangle = \frac{1}{\sqrt{2}}\left(|D\rangle - |A\rangle\right).$$

With polarization qubits it is easy to directly measure in the $\{|D\rangle, |A\rangle\}$ basis: one just rotates the polarizing filter in front of the photon detector by 45° to align with $|D\rangle$. Passing

a photon through the measurement system will then give a click if a diagonal polarization was measured, and no click otherwise. Writing each of $|a\rangle$ and $|b\rangle$ in terms of $|D\rangle$ and $|A\rangle$ is a linear-algebraic exercise of change of basis and results in

$$\begin{aligned}
|a\rangle &= \frac{6}{10}|H\rangle + \frac{8}{10}|V\rangle \\
&= \frac{6}{10}\frac{1}{\sqrt{2}}\left(|D\rangle + |A\rangle\right) + \frac{8}{10}\frac{1}{\sqrt{2}}\left(|D\rangle - |A\rangle\right) \\
&= \frac{\sqrt{2}}{10}\left(3|D\rangle + 3|A\rangle + 4|D\rangle - 4|A\rangle\right) \\
&= \frac{7\sqrt{2}}{10}|D\rangle - \frac{\sqrt{2}}{10}|A\rangle \\
|b\rangle &= -\frac{6}{10}|H\rangle + \frac{8}{10}|V\rangle \\
&= -\frac{6}{10}\frac{1}{\sqrt{2}}\left(|D\rangle + |A\rangle\right) + \frac{8}{10}\frac{1}{\sqrt{2}}\left(|D\rangle - |A\rangle\right) \\
&= \frac{\sqrt{2}}{10}\left(-3|D\rangle - 3|A\rangle + 4|D\rangle - 4|A\rangle\right) \\
&= \frac{\sqrt{2}}{10}|D\rangle - \frac{7\sqrt{2}}{10}|A\rangle
\end{aligned} \tag{1.2}$$

Now it is clear that the measurements looking for $|D\rangle$ on photons carrying state $|a\rangle$ will click almost incessantly since squaring the $|D\rangle$ coefficient results in a click probability of $\left(\frac{7\sqrt{2}}{10}\right)^2 = \frac{98}{100}$. On the contrary, the detector will click only twice for every 100 trials if the state was initially $|b\rangle$. Therefore it is now clear that although $|a\rangle$ and $|b\rangle$ were indistinguishable when measured in the $|0\rangle$ and $|1\rangle$ or equivalently $|H\rangle$ and $|V\rangle$ basis, they give completely different results when the measurement basis is changed.

The various possible polarizations can be pictured on the Poincaré sphere, shown in Figure 1.1. While the sphere usually bears Poincaré's name for polarization states of light, qubit states can be represented in the abstract on a similar sphere using combinations of $|0\rangle$ and $|1\rangle$. This is instead known as the Bloch sphere, and is more often used when referring to spin-$\frac{1}{2}$ quantum systems like electron spins. For clarity, the labels in Figure 1.1 show both the polarization and qubit states.

The Bloch sphere is a very powerful visualization tool for a single qubit. Any pure qubit state $|\psi\rangle = \alpha|0\rangle + \beta|1\rangle$ can be decomposed into spherical coordinates r, θ, ϕ with

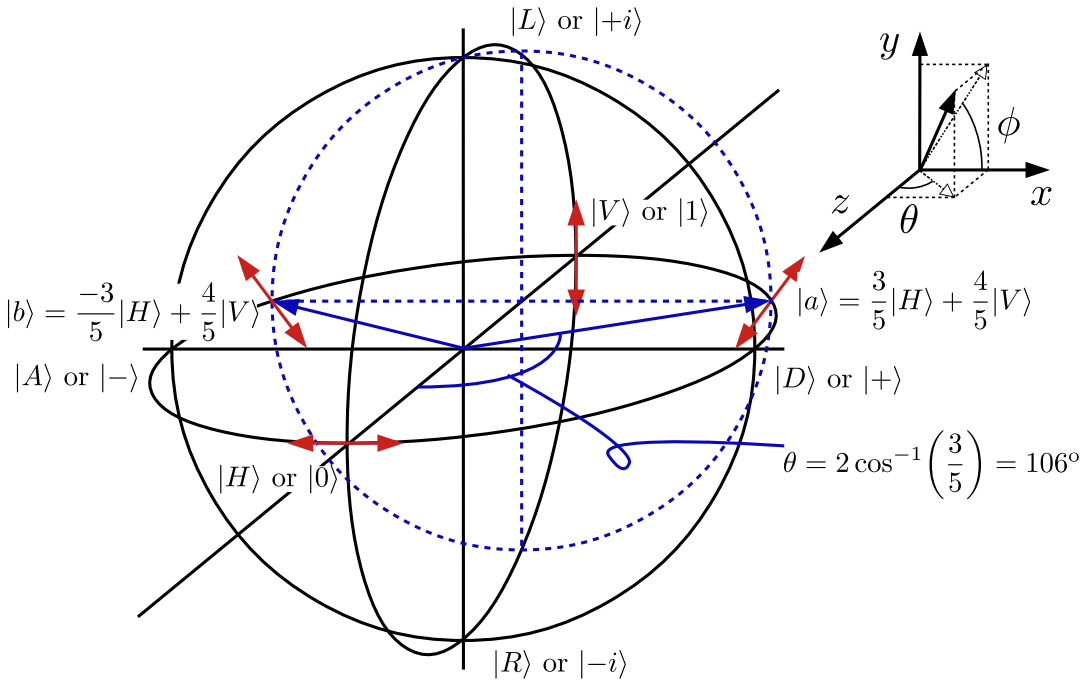

Figure 1.2: The two states $|a\rangle$ and $|b\rangle$ shown on the Poincaré sphere.

$r = 1$ that mark a point on the surface of the Bloch sphere. A statistical mixture of qubits, for example $|a\rangle$ half of the time and $|b\rangle$ the other half, will appear inside the block sphere, with $r \leq 1$. The relationship between α, β, θ, and ϕ is

$$\alpha = \cos\left(\frac{\theta}{2}\right), \qquad \beta = e^{i\phi}\sin\left(\frac{\theta}{2}\right).$$

The states $|a\rangle$ and $|b\rangle$ are shown as the two blue arrows in Figure 1.2. The arrows are known as Bloch vectors, and in this case have the spherical coordinates $(r, \theta, \phi)_{|a\rangle} = (1, 106^{\circ}, 0^{\circ})$ and $(r, \theta, \phi)_{|b\rangle} = (1, -106^{\circ}, 0^{\circ})$ respectively. Until now we have only considered real-valued probability amplitudes which represent the linear polarizations around the equator of the Poincaré sphere, but in general the amplitudes can be complex meaning the general state $|\psi\rangle$ is actually a vector in the two-dimensional complex vector space $\mathbb{C}^2$.

As such, the basis vectors

$$|+i\rangle = \frac{1}{\sqrt{2}}\left(|0\rangle + i|1\rangle\right), \qquad |-i\rangle = \frac{1}{\sqrt{2}}\left(|0\rangle - i|1\rangle\right)$$

are an equally valid choice, and can be mapped from left- and right-circularly polarized light respectively

$$|L\rangle \mapsto |+i\rangle, \qquad |R\rangle \mapsto |-i\rangle.$$

These basis vectors are drawn at the north and south poles of the Poincaré sphere in Figure 1.1.

A broken blue circle is drawn in Figure 1.2 on which the Bloch vectors for $|a\rangle$ and $|b\rangle$ lie. Returning to the initial question of distinguishing one state from the other given the ability to measure in the $\{|0\rangle, |1\rangle\}$ basis, it can now be noted that any state on this circle will also initially appear identical. The only way to distinguish among them is to also tabulate measurement results from the $\{|+\rangle, |-\rangle\}$ and $\{|+i\rangle, |-i\rangle\}$ bases. This process of determining a qubit's state by repeated measurement in various orthonormal bases is termed state tomography [4].

It was previously mentioned that measurement is a fundamental part of quantum mechanics. Proceeding with the newly established intuition about how information is stored in qubits and how we can retrieve it from them, the next section explores quantum measurement in more mathematical detail.

1.1.2 Qubit Measurement

Armed with the mathematical representation of a qubit set forth in subsection 1.1.1, a more formal description of the qubit measurement process can now be established. This section will introduce the three operators X, Y, and Z, and relate them to their observable measurement outcomes.

Referring back to Figure 1.1, it seems natural to describe the measurement process as determining "the amount" along each of the x, y, and z axes shown that contribute to a state given by a Bloch vector. We found that the state $|a\rangle$ introduced in Equation 1.1

seemed to have somewhat more of a contribution from $-z$ than $+z$ with a 64% to 36% split in measurement results, and decidedly more along $+x$ than $-x$ at 98%.

It was simple to compute the probabilities of measuring the two states $|0\rangle$ and $|1\rangle$ on opposite ends of the z-axis of the Bloch sphere given $|a\rangle$, whereas determining the probabilities for $|+\rangle$ and $|-\rangle$ along the x-axis took more work. The simplicity of the calculation for the z component stems from having been provided the state $|a\rangle$ in terms of the basis vectors $|0\rangle$ and $|1\rangle$, which are eigenvectors of the Z operator. This basis is sometimes termed the *computational basis*.

$$Z = \begin{bmatrix} 1 & 0 \\ 0 & -1 \end{bmatrix}, \qquad |0\rangle = \begin{bmatrix} 1 \\ 0 \end{bmatrix}, \qquad |1\rangle = \begin{bmatrix} 0 \\ 1 \end{bmatrix}, \qquad \begin{aligned} Z|0\rangle &= |0\rangle \\ Z|1\rangle &= -|1\rangle \end{aligned} \tag{1.3}$$

The eigenvectors of a linear operator are those that do not change "direction" when operated on, but are instead equal to the original vector up to a scalar factor called the eigenvalue. Here, the eigenvalues for $|0\rangle$ and $|1\rangle$ are $\lambda_0 = 1$ and $\lambda_1 = -1$ which can be verified by doing the matrix multiplication in Equation 1.3.

Before going further though it is worth pointing out some key characteristics the Z operator has. First, it is *Hermitian*, in that it is equal to its adjoint, otherwise know as the transpose of its complex conjugate

$$Z = Z^\dagger \quad \text{where} \quad Z^\dagger = (Z^*)^T.$$

It is also *normal*, as all Hermitian matrices are, which means that operating on a vector with Z and then $Z^\dagger$ gives an equivalent result to having done it the other way around

$$Z^\dagger Z = Z Z^\dagger.$$

Every normal matrix can be decomposed into a sum of orthogonal projectors onto its eigenspaces, with each projector scaled by its eigenvalue. It has already been determined that $|0\rangle$ and $|1\rangle$ are the eigenvectors with corresponding eigenvalues of $\lambda_0 = 1$ and $\lambda_1 = -1$ in Equation 1.3, so Z can be decomposed using the two projectors onto the eigenspaces for λ_0 and λ_1 spanned by $|0\rangle$ and $|1\rangle$ respectively. The associated projectors are

$$P_0 = |0\rangle\langle 0| = \begin{bmatrix} 1 & 0 \\ 0 & 0 \end{bmatrix}, \qquad P_1 = |1\rangle\langle 1| = \begin{bmatrix} 0 & 0 \\ 0 & 1 \end{bmatrix}$$

where the left-pointing $\langle 0|$ and $\langle 1|$ are called *bra*s and are the row vectors equal to the conjugate-transpose of the $|0\rangle$ and $|1\rangle$ column vectors.

$$\langle 0| = |0\rangle^\dagger = \begin{bmatrix} 1 & 0 \end{bmatrix}, \qquad \langle 1| = |1\rangle^\dagger = \begin{bmatrix} 0 & 1 \end{bmatrix}$$

The decomposition for Z then proceeds

$$\begin{aligned} Z &= \begin{bmatrix} 1 & 0 \\ 0 & -1 \end{bmatrix} \\ &= \begin{bmatrix} 1 & 0 \\ 0 & 0 \end{bmatrix} - \begin{bmatrix} 0 & 0 \\ 0 & 1 \end{bmatrix} \\ &= \begin{bmatrix} 1 \\ 0 \end{bmatrix} \begin{bmatrix} 1 & 0 \end{bmatrix} - \begin{bmatrix} 0 \\ 1 \end{bmatrix} \begin{bmatrix} 0 & 1 \end{bmatrix} \\ &= 1 \cdot |0\rangle\langle 0| + (-1) \cdot |1\rangle\langle 1| \\ &= 1 \cdot P_0 + (-1) \cdot P_1 \\ &= \sum_i \lambda_i P_i = \sum_i \lambda_i |i\rangle\langle i|, \quad i \in \{0, 1\}. \end{aligned}$$

With this new information in hand it is possible to return to the question of calculating the probability of measuring $|0\rangle$ or $|1\rangle$ given the state $|a\rangle$. The probability for an outcome is given by the overlap between the state in question before and after it has been projected onto the eigenspace for that outcome. For example, given the state $|0\rangle$, we may be interested in learning the probability of measuring a result from the λ_0 eigenspace. As just described, the projector to use is then P_0, and the resulting projected vector is $P_0|0\rangle$. The overlap between two states $|u\rangle$ and $|v\rangle$ is then their inner product given by $\langle u| \cdot |v\rangle = \langle u|v\rangle$.

Putting everything together, the probability for outcome 0 is found to be

$$p(0) = \langle 0| \cdot P_0|0\rangle = \langle 0| \cdot |0\rangle\langle 0|0\rangle = \langle 0| \cdot \langle 0|0\rangle|0\rangle = \langle 0| \cdot 1|0\rangle = \langle 0| \cdot |0\rangle = \langle 0|0\rangle = 1$$

where the inner product $\langle 0|0\rangle = \begin{bmatrix} 1 & 0 \end{bmatrix} \begin{bmatrix} 1 \\ 0 \end{bmatrix} = 1$ was used twice. Since the inner product is a scalar, it can be moved freely within the expression, shown in the third equality.

This result seems natural, and is what should be expected. Conversely, the probability for a measurement outcome of 1 given state $|0\rangle$ is

$$p(1) = \langle 0| \cdot P_1|0\rangle = \langle 0| \cdot |1\rangle\langle 1|0\rangle = \langle 0| \cdot \langle 1|0\rangle|1\rangle = \langle 0| \cdot 0|1\rangle = 0$$

since the vectors $|0\rangle$ and $|1\rangle$ are orthogonal and their inner product is zero, as can be verified by $\langle 0|1\rangle = \left[\begin{smallmatrix}1 & 0\end{smallmatrix}\right]\left[\begin{smallmatrix}0\\1\end{smallmatrix}\right] = 0$. It is also good to see that the total probability of measuring either a 0 or a 1 for our qubit is unity, for any other conclusion would certainly be suspect!

Using the same procedure on our vector of interest $|a\rangle = \frac{6}{10}|0\rangle + \frac{8}{10}|1\rangle$, we find

$$\begin{aligned}
p(0)_{|a\rangle} &= \langle a|P_0|a\rangle \\
&= \langle a|P_0\left(\frac{6}{10}|0\rangle + \frac{8}{10}|1\rangle\right) \\
&= \langle a|\left(\frac{6}{10}P_0|0\rangle + \frac{8}{10}P_0|1\rangle\right) \\
&= \langle a|\left(\frac{6}{10}|0\rangle\langle 0|0\rangle + \frac{8}{10}|0\rangle\langle 0|1\rangle\right) \\
&= \left(\left(\frac{6}{10}\right)^*\langle 0| + \left(\frac{8}{10}\right)^*\langle 1|\right)\frac{6}{10}|0\rangle\langle 0|0\rangle \\
&= \frac{6\cdot 6}{10\cdot 10}\langle 0|0\rangle\langle 0|0\rangle + \frac{8\cdot 6}{10\cdot 10}\langle 1|0\rangle\langle 0|0\rangle \\
&= \frac{36}{100}\langle 0|0\rangle\langle 0|0\rangle \\
&= \frac{36}{100}
\end{aligned}$$

in agreement with the probability initially found in section 1.1. Similarly, when measuring for a 1 instead the expected probability of $\frac{64}{100}$ is found.

$$p(1)_{|a\rangle} = \langle a|P_1|a\rangle = \langle a|\left(\frac{6}{10}P_1|0\rangle + \frac{8}{10}P_1|1\rangle\right) = \frac{8}{10}\langle a|1\rangle = \left|\frac{8}{10}\right|^2\langle 1|1\rangle = \frac{64}{100}$$

Performing the same calculation using state $|b\rangle = -\frac{6}{10}|0\rangle + \frac{8}{10}|1\rangle$ instead gives identical results to $|a\rangle$, which can be seen by going through the preceding procedure and observing that the negative sign cancels when the probability amplitudes for $\langle 0|$ and $|0\rangle$ are multiplied.

$$p(0)_{|b\rangle} = \langle b|P_0|b\rangle = \langle b|\left(\frac{-6}{10}P_0|0\rangle + \frac{8}{10}P_0|1\rangle\right) = \frac{-6}{10}\langle b|0\rangle = \frac{-6\cdot -6}{10\cdot 10}\langle 0|0\rangle = \frac{36}{100}$$

$$p(1)_{|b\rangle} = \langle b|P_1|b\rangle = \langle b|\left(\frac{-6}{10}P_1|0\rangle + \frac{8}{10}P_1|1\rangle\right) = \frac{8}{10}\langle b|1\rangle = \left|\frac{8}{10}\right|^2\langle 1|1\rangle = \frac{64}{100}$$

However, by using a measurement along the x axis it was shown that the two states $|a\rangle$ and $|b\rangle$ could be distinguished. This change of basis was done in Equation 1.2, where the kets $|D\rangle$ and $|A\rangle$ map to $|+\rangle$ and $|-\rangle$ and are the eigenkets of the X operator with eigenvalues $\lambda_+ = 1$ and $\lambda_- = -1$.

$$X = \begin{bmatrix} 0 & 1 \\ 1 & 0 \end{bmatrix}, \qquad |+\rangle = \frac{1}{\sqrt{2}} \begin{bmatrix} 1 \\ 1 \end{bmatrix}, \qquad |-\rangle = \frac{1}{\sqrt{2}} \begin{bmatrix} 1 \\ -1 \end{bmatrix}, \qquad \begin{aligned} X|+\rangle &= |+\rangle \\ X|-\rangle &= -|-\rangle \end{aligned}$$

The measurement for $|a\rangle = \frac{7\sqrt{2}}{10}|+\rangle - \frac{\sqrt{2}}{10}|-\rangle$ and $|b\rangle = \frac{\sqrt{2}}{10}|+\rangle - \frac{7\sqrt{2}}{10}|-\rangle$ then proceeds with probabilities

$$\begin{aligned} p(+)_{|a\rangle} &= \langle a|P_+|a\rangle \\ &= \langle a| \left(\frac{7\sqrt{2}}{10} P_+|+\rangle - \frac{\sqrt{2}}{10} P_+|-\rangle \right) = \langle a| \left(\frac{7\sqrt{2}}{10}|+\rangle\langle+|+\rangle - \frac{\sqrt{2}}{10}|+\rangle\langle+|-\rangle \right) \\ &= \frac{7\sqrt{2}}{10}\langle a|+\rangle = \left| \frac{7\sqrt{2}}{10} \right|^2 \langle+|+\rangle = \frac{98}{100} \end{aligned}$$

$$p(+)_{|b\rangle} = \langle b|P_+|b\rangle = \langle b| \left(\frac{\sqrt{2}}{10} P_+|+\rangle - \frac{7\sqrt{2}}{10} P_+|-\rangle \right) = \frac{\sqrt{2}}{10}\langle b|+\rangle = \left| \frac{\sqrt{2}}{10} \right|^2 \langle+|+\rangle = \frac{2}{100},$$

easily distinguishing one state from the other.

As has been done for the z and x axes of the Bloch sphere, a measurement can also be performed along y. Following the now-familiar steps, the Y operator has eigenstates along the y-axis of the Bloch sphere, which correspond to $|+i\rangle$ and $|-i\rangle$. These two vectors can be written in the $\{|0\rangle, |1\rangle\}$ basis as

$$\begin{aligned} |+i\rangle &= \frac{1}{\sqrt{2}} (|0\rangle + i|1\rangle) \\ |-i\rangle &= \frac{1}{\sqrt{2}} (|0\rangle - i|1\rangle) \end{aligned} \qquad \Longrightarrow \qquad \begin{aligned} |0\rangle &= \frac{1}{\sqrt{2}} (|+i\rangle + |-i\rangle) \\ |1\rangle &= \frac{-i}{\sqrt{2}} (|+i\rangle - |-i\rangle) \end{aligned}$$

leading to the Y operator

$$Y = \begin{bmatrix} 0 & -i \\ i & 0 \end{bmatrix}, \qquad |+i\rangle = \frac{1}{\sqrt{2}} \begin{bmatrix} 1 \\ i \end{bmatrix}, \qquad |-i\rangle = \frac{1}{\sqrt{2}} \begin{bmatrix} 1 \\ -i \end{bmatrix}, \qquad \begin{aligned} Y|+i\rangle &= |+i\rangle \\ Y|-i\rangle &= -|-i\rangle. \end{aligned}$$

Computing $|a\rangle$ in terms of $\{|+i\rangle, |-i\rangle\}$ gives

$$\begin{aligned}
|a\rangle &= \frac{6}{10}|0\rangle + \frac{8}{10}|1\rangle \\
&= \frac{6}{10\sqrt{2}}\left(|+i\rangle + |-i\rangle\right) - i\frac{8}{10\sqrt{2}}\left(|+i\rangle - |-i\rangle\right) \\
&= \frac{\sqrt{2}}{10}\left(3|+i\rangle + 3|-i\rangle - i4|+i\rangle + i4|-i\rangle\right) \\
&= \frac{(3-i4)\sqrt{2}}{10}|+i\rangle - \frac{(3+i4)\sqrt{2}}{10}|-i\rangle
\end{aligned}$$

which leads to the positive measurement probability along y of

$$\begin{aligned}
p(+i)_{|a\rangle} &= \langle a|P_{+i}|a\rangle \\
&= \langle a|\left(\frac{(3-i4)\sqrt{2}}{10}P_{+i}|+i\rangle - \frac{(3+i4)\sqrt{2}}{10}P_{+i}|-i\rangle\right) \\
&= \langle a|\left(\frac{(3-i4)\sqrt{2}}{10}|+i\rangle\langle+i|+i\rangle - \frac{(3+i4)\sqrt{2}}{10}|+i\rangle\langle+i|-i\rangle\right) \\
&= \langle a|\left(\frac{(3-i4)\sqrt{2}}{10}|+i\rangle\right) \\
&= \left(\frac{(3-i4)^*\sqrt{2}}{10}\langle+i| - \frac{(3+i4)^*\sqrt{2}}{10}\langle-i|\right)\left(\frac{(3-i4)\sqrt{2}}{10}|+i\rangle\right) \\
&= \frac{(3+i4)\sqrt{2}}{10}\cdot\frac{(3-i4)\sqrt{2}}{10} \\
&= \frac{2\cdot|3+i4|^2}{100} = \frac{2\cdot 5^2}{100} = \frac{2\cdot 25}{100} = \frac{50}{100}.
\end{aligned}$$

Therefore, there is an exactly even chance of making a $+i$ or $-i$ measurement. Looking back at Figure 1.2 this result works well with the intuition gained throughout subsection 1.1.1 as the Bloch vector for $|a\rangle$ sits precisely half way between the poles labeled $|+i\rangle$ and $|-i\rangle$.

The main point of this section was to tackle the idea of measuring a quantum state with more rigor, and a clear mathematical process has now been established. The three quantum operators which surfaced as useful in the context of describing a quantum state are in fact the Pauli spin matrices, and are important in describing quantum algorithms

and qubit control. Here they are again, summarized.

$$X = \begin{bmatrix} 0 & 1 \\ 1 & 0 \end{bmatrix}, \qquad Y = \begin{bmatrix} 0 & -i \\ i & 0 \end{bmatrix}, \qquad Z = \begin{bmatrix} 1 & 0 \\ 0 & -1 \end{bmatrix}.$$

Further information on these topics appears in, for example, ref. [5], which is highly encouraged reading.

The next section moves on to describe two-qubit quantum systems and introduces the idea of quantum entanglement, the pursuit of which the work in this thesis is positioned to accelerate.

1.2 Two-Qubit Systems and Quantum Entanglement

Just as in classical information systems where meaningful computation relies on many bits, quantum information systems also come into their own when data from two or more qubits can be combined together. The Bloch-sphere discussed in the previous section made it possible to visualize the state of a single qubit in 3 physical dimensions, and was helpful in determining the measurement statistics of a qubit. Since the same visualization technique does not naturally extend to multi-qubit states, it is helpful to rely more heavily on the mathematics which brings with it an understanding of these more complex systems.

For the purpose of this thesis, it is sufficient to investigate the dynamics of just two qubits, although the concepts as they are presented here do extend naturally to more qubits as well. The motivation for this specific choice of system is that the photonic sources featured in chapter 2 naturally produce entangled photon pairs, which are inherently two-qubit systems.

To begin, section 1.1 presented a single qubit state $|\psi\rangle_a$ as a two-dimensional unit vector in $\mathbb{C}^2_a$. Qubits a and b in states $|\psi\rangle_a$ and $|\phi\rangle_b$ when considered together have a combined state that resides in the four-dimensional complex vector space $\mathbb{C}^{2\cdot 2}_{ab} = \mathbb{C}^2_a \otimes \mathbb{C}^2_b$ formed from the tensor product of $\mathbb{C}^2_a$ and $\mathbb{C}^2_b$, where the label $\{a, b\}$ denotes which system the space belongs to. This new vector space grows exponentially as other qubits are added, with each new qubit q appending another tensor product $\otimes\mathbb{C}^2_q$.

The basis vectors for $\mathbb{C}^4_{ab}$ are composed of pairs of vectors with one element of the pair from an orthonormal basis on $\mathbb{C}^2_a$ and the other from an orthornormal basis on $\mathbb{C}^2_b$. For example, choosing the computational basis for each, an orthonormal basis set for the two-qubit state space is $\{(|0\rangle_a, |0\rangle_b), (|0\rangle_a, |1\rangle_b), (|1\rangle_a, |0\rangle_b), (|1\rangle_a, |1\rangle_b)\}$. The overall basis vector is written as the tensor product of the two vectors in the pair as in $|i\rangle_a \otimes |j\rangle_b \in \mathbb{C}^2_a \otimes \mathbb{C}^2_b$. Often, the $\otimes$ symbol is simply implied, and the two vectors can be combined like $|i\rangle_a \otimes |j\rangle_b = |i\rangle_a |j\rangle_b = |ij\rangle_{ab}$.

Tensor products between linear operators S and T, when written out in matrix form, feature a replica of the second operator T placed in a block matrix at every location (i, j) for the s_{ij} entries of the first operator S, and scaled by s_{ij}.

$$S = \begin{bmatrix} s_{00} & s_{01} & \cdots \\ s_{10} & s_{11} & \\ \vdots & & \ddots \end{bmatrix} \quad \longrightarrow \quad S \otimes T = \begin{bmatrix} s_{00}T & s_{01}T & \cdots \\ s_{10}T & s_{11}T & \\ \vdots & & \ddots \end{bmatrix}$$

Explicitly writing out the basis vectors gives a very nice computational basis over the whole two-qubit space.

$$|00\rangle = \begin{bmatrix} 1 \\ 0 \\ 0 \\ 0 \end{bmatrix}, \quad |01\rangle = \begin{bmatrix} 0 \\ 1 \\ 0 \\ 0 \end{bmatrix}, \quad |10\rangle = \begin{bmatrix} 0 \\ 0 \\ 1 \\ 0 \end{bmatrix}, \quad |11\rangle = \begin{bmatrix} 0 \\ 0 \\ 0 \\ 1 \end{bmatrix}.$$

Determining the measurement statistics of one of the two qubits proceeds almost identically as described in subsection 1.1.2. First, given a system with two qubits, one picks a qubit to measure as well as a basis to measure in. Say, for example, the state $|00\rangle$ is prepared, and the first qubit is sent to a measurement apparatus. This could be done with a pair of photons set up to encode qubits in their polarization like in section 1.1. The measurement would then proceed by sending the first photon through a polarizing filter to a photodetector. The photon state before detection would be $|HH\rangle \mapsto |00\rangle$. If measuring along Z with the polarizing filter set to pass $|H\rangle$, we find

$${}_{ab}\langle HH| \left(P_{Ha} \otimes \mathbb{I}_b\right) |HH\rangle_{ab} = {}_a\langle H|P_{Ha}|H\rangle_{ab} \langle H|\mathbb{I}_b|H\rangle_b = {}_a\langle H|H\rangle_{aa}\langle H|H\rangle_a \cdot 1_b = 1.$$

The projective measurement was only made on the subspace corresponding to qubit a by "filling out" the horizontal projection operator P_{Ha} to the full two-qubit state space using the identity operator $\mathbb{I}_b$ to act on the second qubit. The projection operator then only acts on a, while the identity only acts on b. It is clear that the discovered probability does not depend on the state of b in any way: it could equally have been set to an arbitrary state $|\psi\rangle_b$ since $\langle\psi|\mathbb{I}|\psi\rangle = 1$ for any normalized state $|\psi\rangle$. In the above equation, the subscript b on 1_b is included to explicitly label this result. Had we wished to measure b instead of a along Z, the measurement would have proceeded using the two-qubit operator $\mathbb{I}_a \otimes P_{Hb}$.

Since the preceding measurement was just on qubit a, it must still be possible to continue working with and eventually measure qubit b, which means the quantum system must still be in some state following the measurement. The post-measurement state is given for the measurement operator M by

$$\frac{M|\psi\rangle}{\sqrt{\langle\psi|M|\psi\rangle}}$$

where the square root factor in the denominator renormalizes the state so it remains a unit vector. For the example with the $|H\psi\rangle$ two-photon state we find

$$\frac{(P_{Ha}\otimes\mathbb{I}_b)\,(|H\rangle_a\otimes|\psi\rangle_b)}{\sqrt{{}_{ab}\langle H\psi|\,(P_{Ha}\otimes\mathbb{I}_b)\,|H\psi\rangle_{ab}}} = \frac{P_{Ha}|H\rangle_a\otimes\mathbb{I}_b|\psi\rangle_b}{\sqrt{1}} = |H\rangle_{aa}\langle H|H\rangle_a\otimes|\psi\rangle_b = |H\rangle_a\otimes|\psi\rangle_b$$

following a measurement. In other words, where the measured qubit was already exactly equal to the value the measurement was looking for, the entire post-measurement state is unchanged.

Trying the same calculation for the probability of measuring the first qubit in the horizontal polarization given the state $|D\psi\rangle_{ab}$ we find

$${}_{ab}\langle D\psi|\,(P_{Ha}\otimes\mathbb{I}_b)\,|D\psi\rangle_{ab} = {}_a\langle D|P_{Ha}|D\rangle_a = \frac{1}{\sqrt{2}\sqrt{2}}\,(\langle H|+\langle V|)\,P_H\,(|H\rangle+|V\rangle) = \frac{1}{2}$$

and a post-measurement state of

$$\frac{(P_{Ha}\otimes\mathbb{I}_b)\,(|D\rangle_a\otimes|\psi\rangle_b)}{\sqrt{{}_{ab}\langle D\psi|\,(P_{Ha}\otimes\mathbb{I}_b)\,|D\psi\rangle_{ab}}} = \frac{P_{Ha}\frac{1}{\sqrt{2}}\,(|H\rangle_a+|V\rangle_a)\otimes|\psi\rangle_b}{\sqrt{1/2}} = |H\rangle_a\otimes|\psi\rangle_b.$$

This time, when the first qubit was measured, the state of qubit b remains the same however a is changed from $|D\rangle$ to $|H\rangle$.

So far while measuring qubit a the two-qubit system has behaved as though qubit b could be ignored completely. Consider an example where the two qubit state $|\chi\rangle$ cannot be decomposed into a product state $|\alpha\rangle_a \otimes |\beta\rangle_b$. This is the case for the famous Bell states

$$\left|\Phi^+\right\rangle = \frac{1}{\sqrt{2}}\left(|HH\rangle_{ab} + |VV\rangle_{ab}\right) \qquad \left|\Psi^+\right\rangle = \frac{1}{\sqrt{2}}\left(|HV\rangle_{ab} + |VH\rangle_{ab}\right)$$
$$\left|\Phi^-\right\rangle = \frac{1}{\sqrt{2}}\left(|HH\rangle_{ab} - |VV\rangle_{ab}\right) \qquad \left|\Psi^-\right\rangle = \frac{1}{\sqrt{2}}\left(|HV\rangle_{ab} - |VH\rangle_{ab}\right).$$

The probability of measuring qubit a in the horizontal polarization is again considered, but this time using $|\Phi^+\rangle$.

$$\begin{aligned}
p(H)_a &= {}_{ab}\left\langle\Phi^+\right| \left[\left(P_{Ha}\otimes \mathbb{I}_b\right)\left|\Phi^+\right\rangle_{ab}\right] \\
&= {}_{ab}\left\langle\Phi^+\right| \left[\left(P_{Ha}\otimes \mathbb{I}_b\right)\frac{1}{\sqrt{2}}\left(|HH\rangle_{ab} + |VV\rangle_{ab}\right)\right] \\
&= {}_{ab}\left\langle\Phi^+\right| \left[\frac{1}{\sqrt{2}}\Big(\left(P_{Ha}\otimes \mathbb{I}_b\right)|HH\rangle_{ab} + \left(P_{Ha}\otimes \mathbb{I}_b\right)|VV\rangle_{ab}\Big)\right] \\
&= \frac{1}{\sqrt{2}}\left({}_{ab}\langle HH| + {}_{ab}\langle VV|\right)\left[\frac{1}{\sqrt{2}}|HH\rangle_{ab}\right] \\
&= \frac{1}{2}{}_{ab}\langle HH|HH\rangle_{ab} + \frac{1}{2}{}_{ab}\langle VV|HH\rangle_{ab} \\
&= \frac{1}{2}{}_{a}\langle H|H\rangle_{ab}\langle H|H\rangle_{b} + \frac{1}{2}{}_{a}\langle V|H\rangle_{ab}\langle V|H\rangle_{b} \\
&= \frac{1}{2}
\end{aligned} \tag{1.4}$$

Thus we find a similar measurement probability to when the first qubit was in $|D\rangle$. What makes this Bell state more interesting becomes clear by inspecting the state once the first qubit is found to be horizontally polarized.

$$\frac{\left(P_{Ha}\otimes \mathbb{I}_b\right)\left|\Phi^+\right\rangle_{ab}}{\sqrt{{}_{ab}\langle\Phi^+|\left(P_{Ha}\otimes \mathbb{I}_b\right)\left|\Phi^+\right\rangle_{ab}}} = \frac{1}{\sqrt{1/2}}\left[\frac{1}{\sqrt{2}}|HH\rangle_{ab}\right] = |HH\rangle_{ab}. \tag{1.5}$$

It is now clear that if one checks the polarization for qubit b it will most definitely register as horizontally polarized as well! It can be checked that if the first qubit were to

be measured as vertically polarized, so too would the second. Therefore, the results for the two qubits are very correlated.

As great as this result is, though, one could achieve the same thing by getting a classical computer to generate two-bit strings from the set $\{00, 11\}$ with equal probability and then have a look whether or not the first bit was on. A second person could inspect the second bit, and record the result. Each of the two people would find that their bit was off half of the time and on the other half, which is the same as we found for the probability of seeing the first qubit horizontally polarized. With enough trials, it would also become clear to the two experimenters that the first and second bits were perfectly correlated, which is the same conclusion we drew about the $|\Phi^+\rangle$ Bell state.

What makes the quantum case intriguing is that there are other choices for measurement bases, as was seen in subsection 1.1.2, and nothing requires that the two qubits be measured in the same basis as was just done. This same freedom is not available to the two experimenters studying their classical bits.

If, for example, one experimenter was given qubit a and measured it to be horizontally polarized, a second experimenter, looking for $|D\rangle$ in b, would succeed with a probability, starting from the result in Equation 1.5, of

$$_{ab}\langle HH| \left(\mathbb{I}_a \otimes P_{Db}\right) |HH\rangle_{ab} = {}_a\langle H|P_{Da}|H\rangle_a = \frac{1}{\sqrt{2}\sqrt{2}} \left(\langle D| + \langle A|\right) P_D \left(|D\rangle + |A\rangle\right) = \frac{1}{2}.$$

Recalling that the initial probability of the first experimenter finding a in $|H\rangle$ was also $\frac{1}{2}$, the two experimenters will find no correlations at all: each of their results are entirely random.

As written, the Bell states are in the basis of the Z operator, but just as single qubit states could be expanded into the bases of X or Y instead, so too can the two-qubit states. For $|\Phi^+\rangle$, this looks like

$$\left|\Phi^+\right\rangle = \frac{1}{\sqrt{2}} \left(|HH\rangle + |VV\rangle\right) = \frac{1}{\sqrt{2}} \left(|DD\rangle + |AA\rangle\right) = \frac{1}{\sqrt{2}} \left(|RL\rangle + |LR\rangle\right)$$

from which one can gather by following a similar line of thinking that the correlations in measurement aren't limited to just the $\{|H\rangle, |V\rangle\}$ basis: choosing to measure a and b both in the $\{|D\rangle, |A\rangle\}$ or $\{|L\rangle, |R\rangle\}$ bases will also reveal strong correlations.

In addition, it is worth underscoring that the correlations remain regardless of which basis the state was originally prepared in. This is an example where the experimenters' observations go well beyond the realm of the classically explainable, and for this reason the Bell states are said to have quantum entanglement. Even stronger than that, no other two-qubit state can be more entangled than the Bell states, thus they are sometimes called the *maximally entangled states*.

The maximally entangled state is essential for some applications of quantum information processing, including superdense coding or quantum teleportation. Solutions to some traditional classical problems can also be improved when quantum entanglement is permitted, making the maximally entangled quantum state a desirable resource to have.

In general, it is experimentally difficult to create an exact Bell state. A few different measures are available for researchers to quantify created entangled states, including concurrence and fidelity. Just as it was mentioned the Bell states cannot be written as a product of two pure states, concurrence quantifies to what degree a state is separable into a product. Highly entangled states are not separable, so a high concurrence reveals the state under study is entangled.

Fidelity is instead a measure of how easily two quantum states can be confused by measurement. Given two qubits with density matrices ρ and σ, the fidelity of one to the other is given by

$$F(\rho, \sigma) \equiv \mathrm{tr}\sqrt{\rho^{1/2}\sigma\rho^{1/2}}.$$

A common way of applying fidelity is to choose the reference state σ as one of the Bell states. The resulting number is then stated as "the fidelity to $|\Phi^+\rangle$", for example.

The purpose of this chapter was to establish what quantum entanglement is and why it is a worthwhile resource to create. Chapter 2 pivots the discussion about creating entanglement into the physical world, investigating the evolution of systems which can produce entangled photon pairs. As will be seen, quantum dots are attractive sources of entanglement, but in general produce entangled states that carry an undesirable time dependence like $|\psi(t)\rangle = \frac{1}{\sqrt{2}}\left(|HH\rangle + e^{\frac{i}{\hbar}\delta t}|VV\rangle\right)$. The motivation for the fast rotating half-wave plate in chapter 3 is that it can counter the time-dependent phase, consistently returning the entangled state to the Bell state $\frac{1}{\sqrt{2}}(|HH\rangle + |VV\rangle)$.

Chapter 2

Quantum Photonic Devices

Through the evolution of physical understanding in the early 20th century came the idea that the smallest energy packets of light, called photons, behaved in ways unexplainable by everyday experience. Chapter 1 introduced the wave-particle duality of photons, which has since been the subject of rigorous experimental testing using a wide variety of techniques for photon creation. The first conclusive demonstration of a single photon emitter that refutes any classical description was by Clauser in 1974 [6] using an atomic cascade in mercury atoms, so is a good starting point for a discussion about quantum photonic devices.

This chapter reviews the progress made since then focusing specifically on quantum dots embedded in semiconducting nanowire antennas as the prime candidate for a modern source able to create photon pairs entangled in the Bell state introduced in section 1.2. As will be seen, the fabrication process for quantum dots can create an undesired physical asymmetry in the dot that makes its entangled state depend on the elapsed time between the first and second photons in a photon pair. The technology studied in the remainder of this thesis seeks to offer a corrective tool for precisely this difficulty, and will be equally effective for nanowire quantum dots as for any other.

2.1 Photon Sources

2.1.1 Emission from Atoms

The photon emission mechanism for atoms involves the transition of an electron from a higher energy orbital to one with lower energy. Obeying energy conservation, the lost energy, equal to $E_{\text{photon}} = h\nu = \frac{hc}{\lambda}$ with ν the frequency in Hz and λ the wavelength, is radiated from the atom in the form of a photon, which for certain atomic transitions is in the visible spectrum. For example, the atomic transitions involved in the cascade for mercury in ref. [6] create a yellow and a violet photon with wavelengths $\lambda_1 = 567.6\,\text{nm}$ and $\lambda_2 = 435.8\,\text{nm}$.

For this transition to happen two electrons must first acquire extra energy so they can reside in the higher energy orbital. Electron bombardment is one technique for delivering the requisite energy surplus and was used in ref. [6] and [7], while other schemes rely on photon absorption, that is the reverse process of emission, as in the 1981 experiment by Aspect *et at.* where atoms were used in an experimental violation of the generalized Bell's inequalities [8]. In either case the experimenter must hold the emitting atom at a specific region in space where the excitation can take place and the emission occur.

All three of the experiments just cited achieve this by creating a cloud of atoms inside a vacuum tube where the vapor pressure is low enough that only a single atom will be excited at a time. A different approach was used by Kimble, Dagenais, and Mandel in 1977 where a sparse stream of sodium atoms was fired through a precisely tuned excitation laser such that only a single atom was excited by the laser while passing through it [9].

The trouble with using atoms as a single photon source is they tend not to stay still, making it difficult to isolate just a single one. Single photon sources embedded in crystal avoid this problem by their nature of being at a fixed location in space, an idea which has gained significant traction in the past two decades. The leading two technologies are formed from defects in crystals, like nitrogen vacancy (NV) centres in diamond, and quantum dots. Quantum dots will be the main focus of this chapter, but before investigating them in more depth it is rewarding to take a brief tour of diamond quantum emitters.

2.1.2 Emission from Nitrogen Vacancy Centres in Diamond

Diamond is a dense crystal structure of carbon in which is it possible to embed different isolated atoms such as nitrogen. Where carbon has four valence electrons each participating in a covalent bond with a neighboring carbon, nitrogen has five electrons and thus disrupts the crystal structure. Carbon atoms can be missing in the lattice structure and this kind of crystal defect is known as a vacancy. At 800 °C vacancies within the carbon lattice are mobile and tend to shift toward an embedded nitrogen atom [10]. Three of the nitrogen's electrons participate in covalent bonding with neighboring carbon atoms while the remaining two are non-bonding.

The vacancy located beside the nitrogen would have previously been occupied by a carbon atom again with four covalent bonds. With the carbon absent at the vacancy site next to the nitrogen, one of the four bonds was replaced by the lone nitrogen pair, meaning three sp^3 electrons are to be accounted for from the remaining carbon neighbors of the vacancy site. It is understood that NV centres become negatively charged, for example if an electric bias is applied to the crystal or when a neighboring nitrogen donates its additional free electron, resulting in a total of six electrons in the lattice vacancy.

The electronic structure in a negatively charged NV centre can be analyzed as though the six electrons are represented instead by two holes with quantized orbitals and a total magnetization spin of $S = 1$ [10] [11]. The result is two singlet-triplets with the lower-energy triplet as the ground state and an energy separation in the optical spectrum. Optical excitation and emission happens between lower and higher energy triplets as well as between the singlets. Since NV centers have quantized energy levels like the electron orbitals in single atoms they can be used for single photon generation.

The first demonstration of non-classical light using a single NV center in diamond was by Kurtsiefer *et al.* in 2000 [12]. Their results showed clear photon antibunching in a Hanbury Brown–Twiss experiment with a $g^{(2)}(\tau{=}0) = 0.26$, a measure of how "single" a single photon is. Pure single photons have a $g^{(2)}(0) = 0$, while light in the classical picture always has $g^{(2)}(0) \geq 1$. A key figure of merit for sources of single photons is then how low $g^{(2)}(0)$ can be reduced.

[1]Reprinted by permission from Springer Nature Customer Service Centre GmbH: Springer Nature,

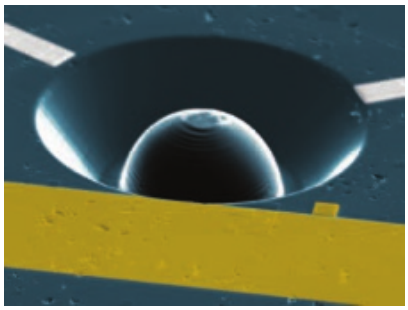

Figure 2.1: A diamond with one NV centre embedded in it is shown. The dome-like structure is a lens for improving the light collection efficiency of the NV centre's photons. A pair of grey electrodes at the image's top create an electrical bias across the crystal so the NV center becomes negatively charged. The gold electrode on the bottom is used to transition the qubit's state between levels in the ground triplet by driving it with RF signals. The crystal was used for the spin-spin entanglement experiment from [13][1].

Nitrogen vacancy centres in diamond have been a gem in experimental quantum information processing yielding brilliant results due to their stability as compared to natural atoms, relative ease of fabrication, pure single-photon emission, and provision of an accessible nuclear spin qubit memory in addition to the already discussed electron spin qubit. They have been used to generate entanglement between a photon and an NV centre spin [14], a prerequisite for follow-up experiments that necessitate entanglement.

For example, in 2013 a pair of NV centres were used to transfer the entanglement between a spin and photon from each into entanglement between the spin of one and the spin of the other three metres away [13]. Additionally using the nuclear spin of the adjacent nitrogen atom as a qubit, a 2014 study showed teleportation of the nitrogen's quantum state across a similar three meter distance [15]. Finally, NV centres were the workhorse in a noteworthy publication from 2015 showing entanglement between states separated by 1.3 km in a loophole-free violation of the CHSH-Bell inequality [16].

Although NV centres offer entangled states to the experimenter, they do so only in the form of spin-to-photon entanglement and do not produce entangled photon pairs. This means NV centres cannot easily be used as a source for distributing entanglement to two remote parties, unlike natural atoms in subsection 2.1.1 for which this is possible. This naturally raises the question about what other solid state quantum sources can be conceived for entangled photon-pair creation that more similarly mimic the behavior of a natural atom. Quantum

[1] "Heralded entanglement between solid-state qubits separated by three metres", H. Bernien *et al.*, Copyright 2013.

dots are the answer, and are the feature of the next section.

2.1.3 Emission from Quantum Dots

Atoms can create entangled photon pairs by a cascade in electron configurations from a high energy state to a ground state via an intermediate orbital, however engineering the isolation of individual atoms is experimentally difficult to achieve. NV centers resolve this by the tangible macroscopic nature of their host material, but do not feature the same photon cascade offered by individual atoms. Quantum dots, sometimes called artificial atoms, strike a balance by creating an imitation of the electron orbitals found in a single atom except within the solid confines of a semiconducting crystal.

Quantum dots and atoms are similar in that they create an electrical potential in space which is an attractive place for electrons to reside. In the case of an atom, a positively charged nucleus creates an electrically attractive force for negatively charged electrons, which then fill quantized orbitals until the atom's overall charge is neutralized. Said equivalently, the atom creates a potential energy well, or a region of lower total potential energy, for the electron to become trapped in. The electrons can transition between higher and lower orbitals as they gain or lose energy, for example by heat or by external optical pumping.

In an analogous way, electrons in a semiconducting crystal lattice are subject to variations in electrical potential that is a function of material composition, shape, and strain, as well as other factors including electric field. In a perfect crystal such as the diamond discussed in subsection 2.1.2, each atom will be bound to its neighbors through covalent bonds formed from one atom's electrons and the next.

The energy required to break a bond depends on the atoms involved and their structure, and is a defining property of semiconductors called the band gap E_g. Using diamond as an example with strong bonds, a lot of energy is required to free a bound electron, leaving behind an electronic *hole*, so the band gap in diamond is very large around $E_g \approx 5.5\,\text{eV}$. That corresponds to the energy carried by ultraviolet light with a wavelength of $\lambda = 225\,\text{nm}$. Band gaps for various semiconductors are shown with respect to their lattice constants in Figure 2.2.

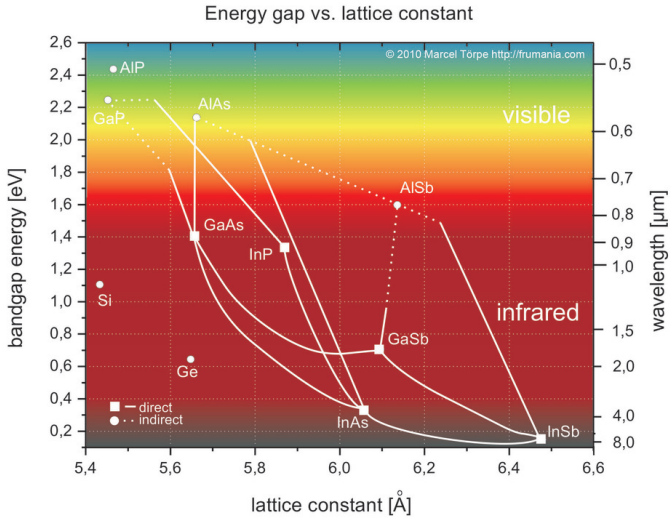

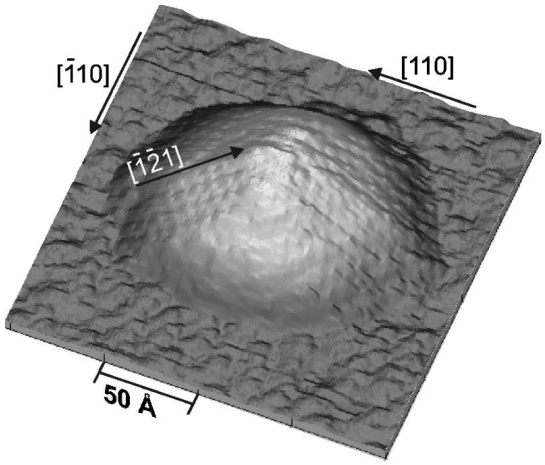

Figure 2.2: [Left] Semiconductor bandgaps depend on material composition. Nanowire quantum dots can be made from a small InAsP section embedded in an InP nanowire waveguide. InP can be seen at the centre of the figure. By Marcel Törpe. Reproduced from [17] under the Creative Commons CC BY-NC-ND 4.0 Licence.

Figure 2.3: [Right] A scanning tunneling microscope image of a quantum dot made from InAs on top of GaAs before a top layer of more GaAs is added. The dot forms by itself due to the lattice constant mismatch between the two crystals and is thus called a self-assembled quantum dot. Reprinted from J. Márquez *et al.*, "Atomically resolved structure of InAs quantum dots," Applied Physics Letters, vol. 78, no. 16, pp. 2309–2311, 2001, with the permission of AIP Publishing [18].

For this reason diamond does not absorb lower-energy light and is thus transparent in the visible spectrum. By contrast, the semiconducting nanowire photonic device studied in this thesis is made of pure wurtzite InP, with exception of the quantum dot embedded in it, and has a near-infrared bandgap of $E_g \approx 1.50\,\mathrm{eV}$ meaning electrons can be energized to the conduction band and leave behind a hole quite easily [19]. This efficient electron-hole creation mechanism is called *above-band optical excitation*.

Embedding a different material inside the InP nanowire with an even lower bandgap, like InAsP, creates a localized potential well. When the InAsP crystal is sufficiently small in size and completely surrounded in all directions by InP, the electron wavefunctions are restricted to quantized energy levels which can each be occupied by at most two electrons of opposite spin due to the Pauli exclusion principle. This is the essence of a quantum dot. The image in Figure 2.3 shows an InAs quantum dot on a GaAs substrate from [18].

An inverted potential well in the valence band can trap holes, which are also quantized and follow the Pauli exclusion principle, in the same restricted region as the trapped electrons. An electron in the quantum dot can then recombine with a hole, falling from a high energy configuration to a lower one and radiating the lost energy in the form of a photon. Two opposite-spin electrons in the lowest energy level of the conduction band can each recombine with two holes confined to the highest energy level of the valence band, creating a pair of photons in the process.

Each photon in the pair will be a slightly different energy, since the presence of an electron in the quantum dot changes the potential energy seen by the second electron just slightly through a Coulomb interaction. The same is true for the two positively charged holes. The two photons can be distinguished by their energy, thus very pure single-photon emission can be created by filtering on wavelength: the single photon nature is guaranteed by the quantized energy levels in the quantum dot as long as the quantum dot (QD) is not re-excited while the emission is happening.

The first demonstration of single-photon emission from a QD was at room temperature in 2000 by Michler *et al.* using small amounts of CdSe in ZnS. The photons were sent to a Hanbury Brown–Twiss (HBT) experiment and a clear dip in the second order correlation was observed, for a $g^{(2)}(0) = 0.47(2)$. Quickly thereafter, Michler *et al.* published a single

photon emitter with a quantum dot coupled to a high-Q resonator. Their device was cooled to 4 K and pumped with a continuous-wave laser. Again by way of a HBT experiment they found an exciton $g^{(2)}(0) \approx 0.25$.

Of specific appeal is that the two photons produced in the biexciton-exciton cascade are entangled in polarization, as in the $|HH\rangle + |VV\rangle$ state discussed in section 1.2. With a high level understanding of the motivation and principles underlying quantum dot single-photon emitters in place, the following section proceeds with an overview of the functionality an ideal entangled photon source should offer as well as how individual characteristics can be quantified. Section 2.3 then delves further into a discussion of the theory behind the quantum dot confining potential and the resulting photon cascade.

2.2 Photon Source Wishlist

The three photonic platforms visited in section 2.1 each have advantages and disadvantages, and although the purpose was to explore the history of single photon emitters as well as some ways of quantifying their characteristics, not much detail was provided. It is important to develop standard language with which to discuss the attributes a certain photon source has and how it performs since doing so allows a fair comparison of competing technologies. In addition, each attribute should be determined in a consistent way so it's possible to measure progress and reward technological advances.

The purpose of this section is to summarize the key features a photon source should possess, as they have largely been agreed upon by the photonic community [20] [21] [22] [23] [24] [25] [26]. Although the success criteria for single- and entangled-photon sources differs slightly there is enough commonality between them that it makes sense to aggregate the two wishlists.

Eight different attractive properties for photonic devices are presented. The first is that photons should be produced on demand – flipping a switch causes a single photon to be emitted with high reliability. It should be possible to flip the switch often making the photon source bright, so it produces enough photons that it could be integrated into meaningful future technology. The photons it emits should be single, pure and simple.

Successive photons should not be distinguishable from one another. It should be possible to tune the energy of the emitted photons. Real-world integration of photon sources into new technologies will require coupling to fibre-optic cable, which necessitates a Gaussian far-field. Ideally, the photonic device meeting the criteria so far also emits entangled photon pairs. Finally, an electrical excitation scheme is desirable for its smaller form factor.

2.2.1 On Demand

A photon source is deemed on-demand if it produces a photon exclusively when triggered. The idea of a trigger is an abstraction from any specific physical implementation, but could be, for example, the rising edge of a digital clock. Equally, it could be a manual push-button that an experimenter controls, debatable in usefulness though that may be. In principle, any photonic device that is silent until a photon is requested of it, at which point only a single photon is produced, will be on-demand. Likewise, the principle of an on-demand source can be extended to entangled photon pairs, where instead of a single photon the experimenter receives two and they're entangled.

The primary motivation for the on-demand criteria is the deterministic ability to then produce quantum interference such as by overlapping photons at a beam splitter. Experiments like boson sampling [27] and linear optical quantum computing [28] [29] pass photons through an optical network and benefit directly if the precise timing of photon creation can be preset. Quantum repeaters, required to extend the distance entangled states can be distributed, rely on the same principle and again will be made significantly more successful with an on-demand source.

On-demand photon generation with quantum dots can largely be broken into two categories based on their excitation scheme. Optical excitation is done using a laser to create an electron-hole pair which then produce a photon upon recombination. By selecting a pulsed laser which delivers energy with a well-defined repetition rate the electron-hole pair will only be created when a pulse arrives, making an on-demand source possible. This strategy works for both single photon generation [30] [31] [32] [33] [34] [24] as well as for entangled photon pair sources [23] [35] [22] [25].

Alternatively, it is possible to create on-demand photons or photon pairs from quantum dots using electrical excitation [36] [37] [38]. Advantages of electrical generation is the flexible control over the excitation trigger, as well as higher trigger rates. Schemes using electrical excitation tend to cause fluctuations in the local charge environment of the quantum dot, though, which reduces indistinguishably.

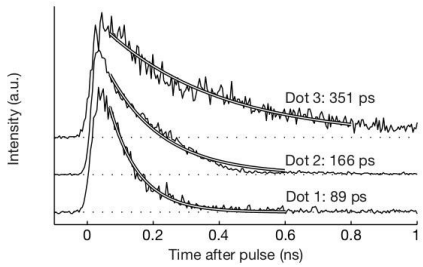

Figure 2.4: Lifetime measurements of three different quantum dots. Reproduced from [31][1].

One way to demonstrate that a particular photonic device is producing on-demand photons is to trigger one and start a timer, stopping it when a single photon detector clicks. Repeated trials can then be used to create a histogram of clicks versus delay time, an example of which is shown in Figure 2.4. The characteristic peak with an exponentially decaying tail represents the temporal profile of a single photon, where the 1/e point on the tail is the lifetime of the electron-hole pair. A photon source that isn't deterministic would not show a clear correlation between start time and photon detection.

Spontaneous parametric down-conversion (SPDC) in a nonlinear crystal is commonly used as a source of single photons or entangled photon pairs. The process is Poissonian in nature and thus creates photons in a probabilistic fashion. By contrast, the pulsed optical and electrical excitation schemes for quantum dots create photons in a triggered, deterministic way. Since the SPDC sources do not meet the on-demand criterion for an ideal single photon source, they are not considered any further in this thesis.

2.2.2 Bright

Somewhat related to the discussion about on-demand photon generation is the requirement that a photon source be bright. Whereas an on-demand source can create more intense

[1]Reprinted by permission from Springer Nature Customer Service Centre GmbH: Springer Nature, "Indistinguishable photons from a single-photon device", C. Santori *et al.*, Copyright 2002.

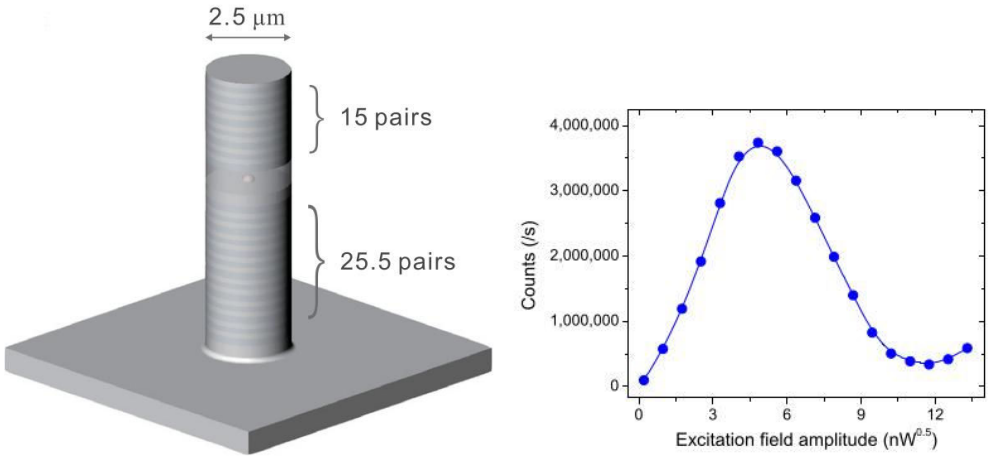

Figure 2.5: [Left] Schematic of a quantum dot embedded in a micropillar cavity with DBRs on the top and bottom. Photons are emitted upward. [Right] Variation in photons collected from a quantum dot embedded in a micropillar cavity as pump power is varied. The peak is exactly a π pulse, taking the Bloch vector from $|0\rangle$ to $|1\rangle$. Reprinted figure with permission from [33]. Copyright 2016 by the American Physical Society.

light, characterized by a higher photon flux or photon counts per second (CPS), by increasing the frequency at which it is triggered, this does little good if only a small fraction of the photons are captured into an optical system for real use. Bright photon sources are thus those for which a high percentage of emitted photons are directed into an operator's lens, rendering them available for him to use, which in turn boosts the on-demand photon production probability to unity.

The brightness of a photonic source is characterized by the fraction of photons coupled into the first lens of a measurement system for a given triggered pulse. Two main factors come into play for overall source efficiency: how well an excited state is populated, and how well the resulting photon can be collected. The overall efficiency is then formed from the product of these two.

Improvements to the population efficiency in a quantum dot are done through precise choice of excitation method. For example, with resonant pulsed excitation as in refs. [32], [33], and [23], the power for the laser pulse is chosen so as to maximally populate the

quantum dot's excited state. An example of counts vs excitation power is shown at right in Figure 2.5.

Extraction efficiency for quantum dots embedded in their bulk material is extremely poor, as the semiconductors in question have a high index of refraction and the quantum dots emit photons in all directions. The semiconductor-air interface thus reflects most of the photons back into the bulk material due to total internal reflection, allowing only a small fraction photons emitted practically perpendicular to the boundary to escape. Of those, again only a fraction can be collected by a microscope objective lens.

Consider the quantum dot embedded in the micropost photonic device pictured in Figure 2.5. The DBRs on the top and bottom create a cavity into which the quantum dot can emit a photon, from where it escapes through the thinner top reflector. This design gives the photon a preferred direction which significantly boots the fraction that can be collected into a lens. At the optimal driving power more than 3.7 million photons per second are detected. The authors excite the quantum dot 81 million times per second, so the overall efficiency is 4.57%. They estimate the generation efficiency is 96% while the extraction efficiency is 66%.

A disadvantage of the micropillar approach is that the high Q-factor cavity shown can only be tuned to either the exciton or bi-exciton energy, but not both at the same time. This prohibits the entangled photon pairs from being emitted from the design as considered. Alternative strategies that boost collection efficiency of both photons in an entangled pair are termed *broadband* photonic devices. Several different proposals have been tested and Figure 2.6 shows three of the most promising ones.

Since the main challenge hindering high light extraction efficiency from a quantum dot is total internal reflection, one idea is to plaster a layer of quantum dots directly to the bottom of a small solid immersion lens (SIL), eliminating the air gap. This allows the light to escape the semiconductor crystal at a comparatively wide angle which can then be collected into a microscope objective. A mirror below the quantum dot layer additionally reflects downward-emitted light back up and into the first lens instead. Chen et al. studied a photonic device based on this exact design in 2018 with good results, achieving 65% single-photon extraction efficiency. Pair efficiency, where both the exciton and biexciton

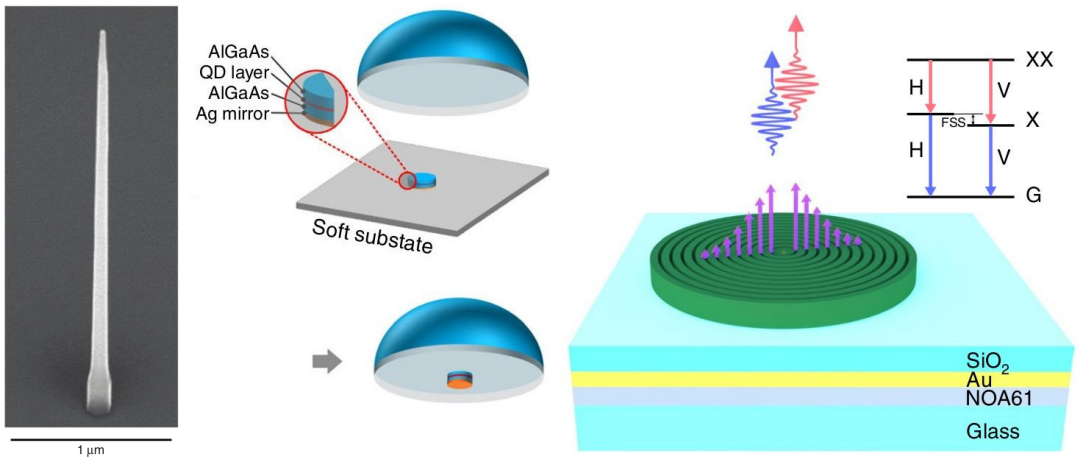

Figure 2.6: Three designs for broadband photon collection. [Left] A nano-scale photonic wire with a quantum dot embedded in it. This is the photonic device studied in chapter 5. Reproduced from [40] under the Creative Commons CC BY 4.0 license. [Center] A layer of self-assembled quantum dots, along with a bottom mirror, glued to a solid immersion lens. Reproduced from [39] under the Creative Commons CC BY 4.0 license. [Right] A broadband bullseye cavity with a quantum dot at the center. Reprinted by permission from Springer Nature Customer Service Centre GmbH: Springer Nature Nanotechnology, "A solid-state source of strongly entangled photon pairs with high brightness and indistinguishability" J. Liu *et al.*, Copyright 2019 [41].

are extracted, was found to be 37.2% [39]. A schematic is shown at centre in Figure 2.6.

The results presented in chapter 5 use the exciton from the nanowire quantum dot photon source at left in Figure 2.6. Its photon pair extraction efficiency is 18% [40].

2.2.3 Highly Pure

One killer application of single photon sources is the use in next-generation cryptographic schemes as a provably secure way of distributing encryption keys. The security of single-photon protocols like this relies on the fundamental indivisibility of a photon: if a receiver receives his photon he can be certain no one else has also previously measured it, or if they

have, the original photon's state could not have been identically replicated. As soon as more than one photon carries the same information, though, one can be intercepted in an attack called *photon splitting*.

This motivates the criteria of high photon purity. A pure photon source will emit only one photon at a time, meaning that two or more photons should never emerge from it in unison. Quantum dots provide this guarantee due to the Pauli exclusion principle, which limits the number of electron-hole pairs in the s-shell of the QD to two. Since the energies of the biexciton and exciton photons are slightly different, they can each be isolated by spectral filtering and thus are each pure single photons.

Single photon purity is measured by way of an HBT setup [42] [9]. The purpose of the original experiment was to use two different detectors separated by some distance to observe the star Sirius in the night sky with better resolution than was possible at the time. Correlating the results from the two detectors gave Hanbury Brown and Twiss the possibility of measuring Sirius' precise size. This principle was based on the tendency of photons from a thermal source like a star to arrive in bunches, resulting in positive correlation events.

The opposite effect is expected from a pure single-photon source, where photons should have strong anti-bunching, or anti-correlation events. Qualitatively this means that one should not be able to measure a second photon from a single photon source in the same time interval as one was just found. To test this, a stream of single photons is sent through a beam splitter with one single-photon detector at each output port, as shown in Figure 2.7. The two detectors then register clicks, and the time difference between two clicks is recorded. A designated detector is defined as the zero reference meaning a positive delay is recorded if it clicks first; otherwise the delay is negative. The resulting histogram should be symmetric, with $g^{(2)}(\tau) = g^{(2)}(-\tau)$.

The key indicator of anti-bunched light is the absence of two simultaneous photon detection events. At right in Figure 2.7, the biexciton and exciton from the bullseye quantum dot source in Figure 2.6 were each correlated individually in HBT experiments. The absence of a centre peak for both cases shows very pure single photon creation. This is quantified by the second order correlation $g^{(2)}(\tau)$, with τ the delay time between detection

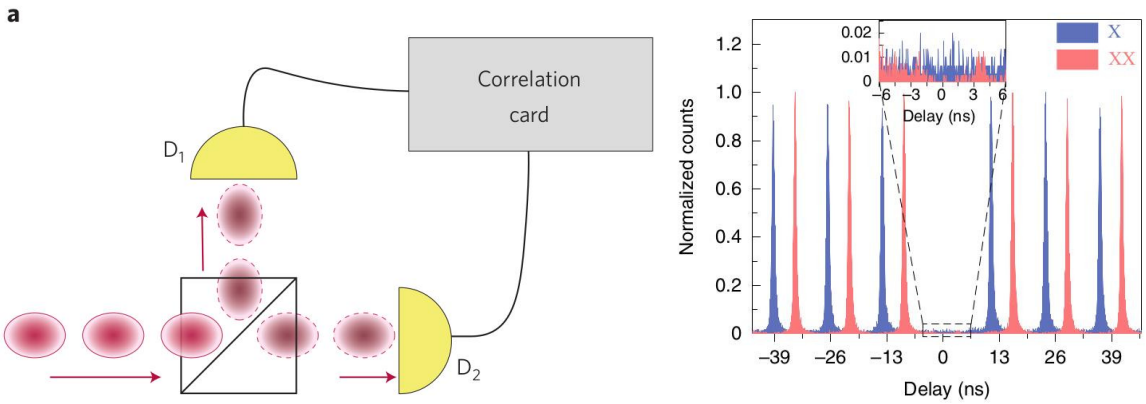

Figure 2.7: A schematic showing the measurement for quantifying single photon purity using a HBT experiment. Reprinted by permission from Springer Nature Customer Service Centre GmbH: Springer Nature Nanotechnology, "High-performance semiconductor quantum-dot single-photon sources" P. Senellart *et al.*, Copyright 2017 [25]. Results for both the biexciton (XX) and exciton (X) from the bullseye cavity at right in Figure 2.6. Reprinted by permission from Springer Nature Customer Service Centre GmbH: Springer Nature Nanotechnology, "A solid-state source of strongly entangled photon pairs with high brightness and indistinguishability" J. Liu *et al.*, Copyright 2019 [41].

events.

The HBT experiment is a means to an end, which is to determine whether a given state of light is single-photon or not. Mathematically the same information can be gained by studying the beam prior to it entering the beam splitter. In this scheme, a perfect single detector capable of multi-photon detection is placed in the beam and its clicks are recorded with their time.

Formally, for a classical field in front of the beam splitter, the second order correlation function gives the expected value of the joint intensities measured on the detector at time t and at time $t = \tau$, normalized to the product of the expected value of the intensity at each respective time $\langle I(t)\rangle = \langle I(t+\tau)\rangle = \bar{I}$. For a stationary beam, that is one whose intensity doesn't vary with time, the average intensity at two different times is equal, as

shown. Then,

$$g^{(2)}(\tau) = \frac{\langle I(t)I(t+\tau)\rangle}{\langle I(t)\rangle \langle I(t+\tau)\rangle} = \frac{\langle I(t)I(t+\tau)\rangle}{\bar{I}^2}.$$

When the expected intensities at time t and $t+\tau$ are uncorrelated, say for example when the time delay τ is much longer than the coherence time of the light under study τ_c, the numerator reduces to $\langle I(t)I(t+\tau)\rangle_{\tau \gg \tau_c} = \langle I(t)\rangle\langle I(t+\tau)\rangle = \bar{I}^2$ for a $g^{(0)}(\tau) = 1$.

In the opposite limit with $\tau = 0 < \tau_c$, the numerator becomes $\langle I(t)^2\rangle$, an average of the product of intensities. Splitting $I(t)$ into average and fluctuating parts as $I(t) = \bar{I} + \Delta I(t)$ results in

$$\langle I(t)^2\rangle = \left\langle (\bar{I} + \Delta I(t))^2 \right\rangle = \bar{I}^2 + 2\bar{I}\,\langle \Delta I(t)\rangle + \left\langle \Delta I(t)^2 \right\rangle = \bar{I}^2 + \left\langle \Delta I(t)^2 \right\rangle$$

where the fluctuation varies equally above and below zero for a time-averaged value of $\langle \Delta I(t)\rangle = 0$. The square of the fluctuation is always positive, though, meaning $\langle \Delta I(t)^2\rangle \geq 0$ with equality only if there is no fluctuation in intensity at all, say for a very stable monochromatic beam. Thus it is found that

$$g^{(2)}(\tau = 0) = \frac{\langle I(t)I(t+\tau)\rangle}{\bar{I}^2} = \frac{\bar{I}^2 + \langle \Delta I(t)^2\rangle}{\bar{I}^2} = 1 + \frac{\langle \Delta I(t)^2\rangle}{\bar{I}^2} \geq 1.$$

The conclusion is that classical light cannot have a $g^{(2)}(0) < 1$.

By contrast, after quantizing the electric field, $g^{(2)}(\tau)$ can be written in terms of the photon creation and annihilation operators $\hat{a}^\dagger$ and $\hat{a}$, and it will be found that the single-photon state $|1\rangle$ has a very characteristic nonclassical feature where $g^{(2)}(0) = 0$. The expected intensity in the quantum picture is proportional to the number of photons per unit time, or photon flux $\langle I(t)\rangle \propto \langle \hat{n}\rangle = \langle \hat{a}^\dagger \hat{a}\rangle$. Here, $\hat{n} = \hat{a}^\dagger \hat{a}$ is the photon number operator.

Similarly, investigating only the case for $\tau = 0$, the numerator of $g^{(2)}(0)$ is written $\langle \hat{a}^\dagger \hat{a}^\dagger \hat{a}\hat{a}\rangle$. The second order correlation function in the quantized theory is thus

$$g^{(2)}(0) = \frac{\langle \hat{a}^\dagger \hat{a}^\dagger \hat{a}\hat{a}\rangle}{\langle \hat{a}^\dagger \hat{a}\rangle^2} = \frac{\langle \hat{n}(\hat{n}-1)\rangle}{\langle \hat{n}\rangle^2}.$$

The last step used the commutation relation $[\hat{a}, \hat{a}^\dagger] = \hat{a}\hat{a}^\dagger - \hat{a}^\dagger\hat{a} = 1$. Here, the expectation values are all taken in their quantum-mechanical form as $\langle \hat{O}\rangle_\rho = \mathrm{tr}(\rho \hat{O})$ for the observable

$\hat{O}$. Using the photon number state $|n\rangle$ as the number of photons in a mode, some further properties of the creation and annihilation operators are

$$\begin{aligned} &\hat{a}|n\rangle = \sqrt{n}|n-1\rangle && (\hat{a}|n\rangle)^\dagger = \langle n|\hat{a}^\dagger = \sqrt{n}\langle n-1| \\ &\hat{a}^\dagger|n-1\rangle = \sqrt{n}|n\rangle && (\hat{a}^\dagger|n-1\rangle)^\dagger = \langle n-1|\hat{a} = \sqrt{n}\langle n| \\ &\hat{a}|\alpha\rangle = \alpha|\alpha\rangle \end{aligned}$$

where $|\alpha\rangle$ is the coherent state, produced by an ideal continuous-wave laser.

To gain some intuition about the $g^{(2)}(0)$ for the quantized field it helps to view some properties of the number operator $\hat{n}$ too.

$$\begin{aligned} &\hat{n}|n\rangle = n|n\rangle && \hat{n}(\hat{n}-1)|n\rangle = \hat{n}^2|n\rangle - \hat{n}|n\rangle = (n^2-n)|n\rangle \\ &\langle n|\hat{n}|n\rangle = n && \langle n|\hat{n}(\hat{n}-1)|n\rangle = n^2 - n \\ &\langle 0|\hat{n}(\hat{n}-1)|0\rangle = 0 && \langle 2|\hat{n}(\hat{n}-1)|2\rangle = 2 \\ &\langle 1|\hat{n}(\hat{n}-1)|1\rangle = 0 && \langle 3|\hat{n}(\hat{n}-1)|3\rangle = 6 \end{aligned}$$

A way to understand the expectation value in the numerator of $g^{(2)}(0)$ is as two times the rate at which the single-photon detectors click simultaneously for pairs of photons. The formula $\frac{1}{2}n(n-1)$ is recognizable as a specific case of n choose two, which gives the possible number of ways of forming pairs between photons. With $n = 1$, no pairs can be formed, while for $n = 2$ one pair is possible and $n = 3$ can have three pairs. There are then two photons in a pair contributing to that measured intensity, so the numerator values for states $|1\rangle$, $|2\rangle$, and $|3\rangle$ are $\langle\hat{n}(\hat{n}-1)\rangle_{|n\rangle} = 0, 2, 6$ respectively.

Thus, for the single photon state $|1\rangle$, it is now clear that only one detection event at time t is possible, meaning $g^{(2)}(0) = 0$, a nice nonclassical result.

Experimentally, it isn't possible to detect multiple photons with infinitesimal time resolution at the same location, so in practice the HBT configuration with a beam splitter and two detectors is used. The result is the same as can be confirmed by substituting the creation operators for the two output modes of the beam splitter $\hat{c}^\dagger$ and $\hat{d}^\dagger$ in place of $\hat{a}^\dagger$ as

$$\hat{c}^\dagger = \frac{1}{\sqrt{2}}\left(\hat{a}^\dagger - \hat{b}^\dagger\right) \qquad \hat{d}^\dagger = \frac{1}{\sqrt{2}}\left(\hat{a}^\dagger + \hat{b}^\dagger\right),$$

along with the vacuum input of $|0\rangle$ on port b. Here, a is the incoming port with the field of interest, b is the second beamsplitter input, c is the transmitted port from a while d is the last output.

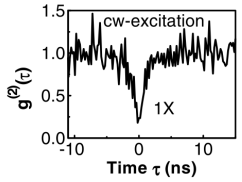

Figure 2.8: A $g^{(2)}(\tau)$ measurement for a turnstile quantum dot. The dip below 1 is characteristic of a nonclassical field. From P. Michler *et al.*, "A quantum dot single-photon turnstile device," Science, vol. 290, no. 5500, pp. 2282–2285, 2000 [43]. Reprinted with permission from AAAS.

With theory of the HBT experiment now well understood, the experimenter must determine how their $g^{(2)}(0)$ should be calculated in practice. The methodology is different for continuous wave excitation compared with pulsed excitation, since the pulsed case does not meet the criteria of a stationary field – one of the initial assumptions for this analysis of $g^{(2)}(\tau)$.

Under continuous wave excitation, one will collect a curve of coincidence counts that appears like in Figure 2.8. When properly normalized the $g^{(2)}(0)$ can be read from the height of the time bin at zero delay. A common strategy is to fit the dip with a pair of exponentials to extract the photon's lifetime.

A second order correlation measurement on a single photon source using resonant excitation will result in the histogram pictured in Figure 2.7. The main feature of this graph is a pulse train with the centre peak at $\tau = 0$ missing. The authors calculated $g_X^{(2)}(0) = 0.001$ and $g_{XX}^{(2)}(0) = 0.007$ by integrating the centre peak and dividing it by the mean of the neighboring peaks [41].

Resonant excitation is a great choice when considering alternative excitation methods as it very reliably populates just the energy levels used in creating the single photons. In addition, it significantly suppresses re-excitation of the quantum dot, which is a key contributor to multi-photon emission. As in [41], very low values for $g^{(2)}(0)$ are being demonstrated in state-of-the-art photonic devices.

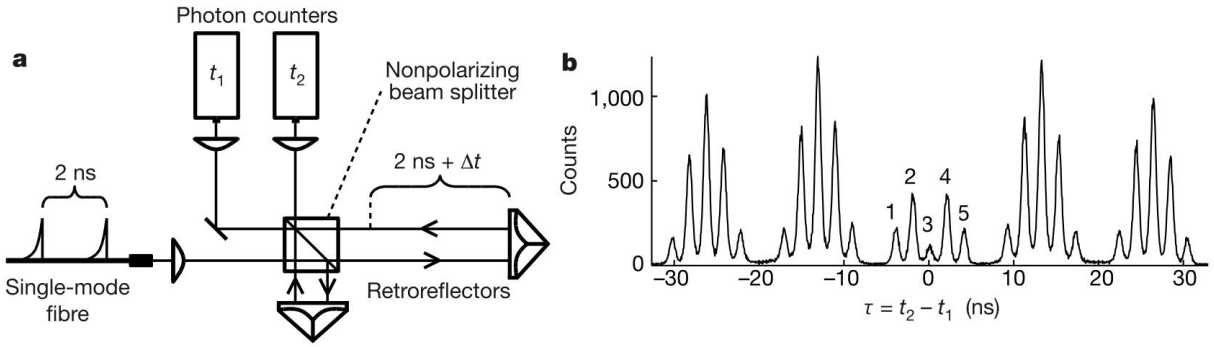

Figure 2.9: HOM experiment and example coincidence measurements for a single photon source in a micropillar cavity. Reprinted by permission from Springer Nature Customer Service Centre GmbH: Springer Nature, "Indistinguishable photons from a single-photon device", C. Santori *et al.*, Copyright 2002 [31].

2.2.4 Indistinguishable

A use case for single photons that has garnered a lot of attention is the prospect of using them for linear optical quantum computing (LOQC) [28] [29]. The gates implemented in LOQC in part depend on the quantum behavior of destructive interference photons exhibit when overlapped on a beam splitter. Hong, Ou, and Mandel first showed in 1987 that when indistinguishable, photons are observed to exit a beam splitter by a mutual port [44]. This interesting feature places some requirements on the photons in question, which will be discussed briefly.

Photons are said to be indistinguishable if they are the same in every respect. As mentioned in chapter 1, photons have many degrees of freedom in which quantum information can be encoded. That discussion proceeded assuming a qubit was stored using the polarization state of a photon. In addition, photons have a distribution of frequencies around a centre, a distribution of electric field in space, and a temporal shape. When none of these characteristics can be used to discern one photon's wave packet from another the two are said to be indistinguishable. Then, and only then, can the destructive interference of probability amplitudes at a beam splitter come into effect.

The typical method of quantifying indistinguishability is to use a similar correlating

technique as in subsection 2.2.3 with two detectors at the output of a beamsplitter, except with the modification that two separate photons are sent into the two input ports. When the two photons feature perfect wavefunction overlap they will both exit the beamsplitter on the same port and no two-photon coincidence measurements will take place. This is known as the HOM dip.

A schematic of the experiment is shown in Figure 2.9. A quantum dot is driven at 13 ns intervals by two pulses separated by 2 ns. Each of the two pulses creates a single photon, which are then sent through a beam splitter twice. The output from the first pass through the beam splitter is redirected back through it a second time, but with one arm at a 2 ns time delay. The second time through the beam splitter there is the potential for two successive photons to overlap.

The overlap will only occur under the condition that the first photon takes the longer delay path, transmitted straight through the beam splitter in the experiment. The second photon must then take the short path. Upon meeting at the beam splitter the two photons will overlap in time and will thus be given a chance to destructively interfere. When they do, they will both be directed toward the same photon counter, making only that single counter click.

Peak 3 in Figure 2.9b is at the middle of the centre grouping and corresponds to the two-photon coincidences. In this experiment it is visibly lower than the two adjacent peaks 2 and 4. A coincidence will occur in peak two and four if both photons take the same arm through the interferometer. Peaks one and five happen when the first photon takes the short arm and the second takes the long one.

Using the procedure described in [31] the authors calculated a wavepacket overlap of 0.81. This particular experiment was done using pulsed, but not resonant excitation. Switching to resonant excitation as well as designing the photonic devices to limit the charge noise contribution to dephasing and spectral walking has significantly increased the indistinguishability achievable from quantum dots, with recent reports as high as 0.9956(45) [34], an exceptional result.

2.2.5 Tunable

Traditional communication systems span vast distances. Whether in the form of radio waves in free space, electrical signals in cables, or light in fibre optic cable, the key to success on such a large scale is the ability to replicate data. This makes a faint signal recoverable through amplification and noise reduction. However, quantum states cannot be cloned and must thus be relayed by other means. This is especially true given that losses in optical fibre make long-distance communication infeasible over distances larger than one hundred kilometers.

Current proposals rely on entanglement swapping, whereby two remote sources of entangled flying qubits, like photons, each emit a pair of photons in lock step. One photon from the pair is sent to a receiving party while the second from each pair is overlapped on a beam splitter. Under the condition that it is impossible to determine which photon at the beam splitter's exit came from which of the two sources, the entanglement is transferred to the two remaining photons, now twice the distance apart.

The quantum interference at the beam splitter is of the same type as was described in subsection 2.2.4. One of the criteria for indistinguishability is that the photons in question must have identical frequencies. From subsection 2.1.3, the photons created in a quantum dot depend on the band gap of the material, so not all quantum dots will create photons at the same frequency. In addition, local fluctuations in the confining potential of the quantum dot or the electrostatic environment surrounding the quantum dot can vary photon frequency. For example, heating a crystal will cause it to undergo thermal expansion, increasing the size of the QD and thus reducing the confinement slightly. This then equivalently lowers the quantum dot's emission energy.

To meet the requirements of a quantum relay a photonic device should be able to have its photons tuned in energy without affecting the quality of entanglement. Several ideas have been demonstrated, such as tuning with temperature [43] [45] [46], a.c. Stark effect [47], electric field [48] [49] [50], magnetic field [51], strain [52] [38] [53] [54] [55], device shape [19] or even using the sidebands of the Mollow triplet [56] as a source of single photons. Each method complements other design choices, and the upshot is that quantum dot sources can be tuned sufficiently well for real-world applications.

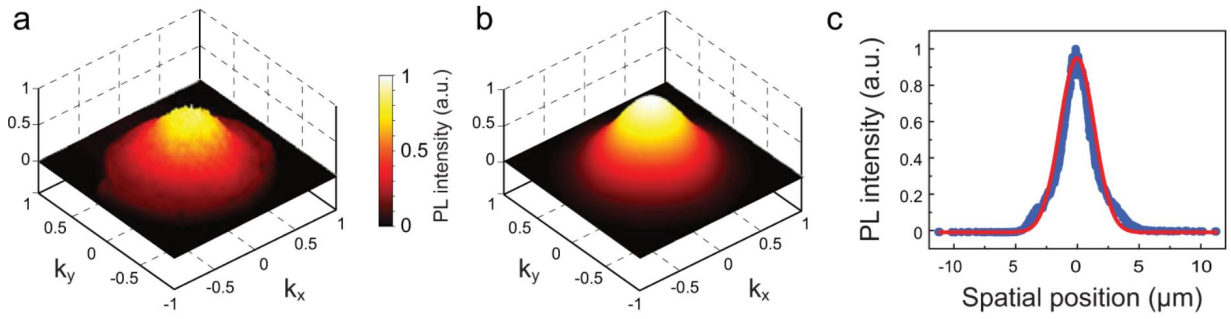

Figure 2.10: Image of a nanowire quantum dot's far field showing a very Gaussian shape. Reprinted (adapted) with permission from G. Bulgarini *et al.*, "Nanowire waveguides launching single photons in a gaussian mode for ideal fiber coupling," Nano Letters, vol. 14, no. 7, pp. 4102– 4106, 2014 [57]. Copyright 2014, American Chemical Society.

2.2.6 Gaussian Far-Field

One appeal of using light to carry a quantum state is its compatibility with the optical infrastructure already in place today. In order to interface with this existing optical technology it must be possible to extract the light from a photonic device and then couple it into a channel for processing and distribution.

Two main methods exist for achieving this goal. The first relies on the pattern of the far-field emission from the photonic device. If suitable, a fibre optic cable and in-coupling lens can be set up in the beam path from the photonic device to capture the emitted photons. A gaussian emission profile is highly desirable because it can be coupled into fibre optic cabling with high efficiency.

Integrated optics offers an alternative approach [58] [59]. Given that a photonic device is compatible with on-chip waveguides, photons can then be smoothly coupled into a fibre using existing fabrication techniques. Processing can also be done using on-chip components prior to sending a photon over large distances.

The image in Figure 2.10 is the mode profile emitted from a quantum dot in a tapered nanowire. It has a 98.8% overlap with Gaussian form, and the authors achieved fibre coupling efficiencies of the quantum dot's emission of 93.3%.

2.2.7 Entangled

Although already discussed in chapter 1, subsection 2.1.3, and subsection 2.2.2, the criteria of entanglement additionally deserves a place in the photonic device wishlist. The reason is that single photon sources can be very high quality but not emit entangled photons. NV centers fall into this category, as do the photonic devices with quantum dots embedded in micropillars such as ref. [34] or other high-Q cavities [24].

The entanglement-generating criterion often requires imposing compromises on the design of a photon source, as the parameters that would be optimal for one of the two photons in an entangled pair may not be optimal for the other. For example, in the quantum dot biexciton-exciton cascade, the two emitted photons do not have the same energy, which, for them to be bright, necessitates a broadband light extraction mechanism. QDs embedded in tapered nanowires are good broadband sources of entangled photons, but care must be taken when creating them to avoid introducing carrier traps in the vicinity of the QD [40] [60].

Reversing the perspective, it shouldn't be assumed that a photonic device which produces good entangled photon pairs is also a good single photon emitter. While the individual photons in a pair can be used separately, as has been done to demonstrate frequency shifting in chapter 5, the entangled-photon source may fall behind an optimized single-photon source on metrics such as purity, indistinguishability, and brightness.

Creating perfectly symmetric confining potentials for the QDs in a nanowire is challenging, so by their nature they have fine structure splitting which impacts the state of the emitted entangled photon pairs. This topic will be discussed further in section 2.3, but warrants mention here too.

2.2.8 Electrically Driven

While other items could also be considered for inclusion on a photonic source wishlist, the central outstanding item is that a photonic source be electrically driven. Such a source significantly advantages the form-factor and space imprint required to create single or entangled photon pairs. In addition, it gives the photonic device operator access to

extremely high repetition rates sooner limited by the lifetime of the quantum states than by the electronics involved.

Most experimental results for quantum dots are published using optical excitation. However, the technical requirements for optical excitation are relatively high, and make for a relatively large physical footprint of supporting equipment. Resonant excitation in particular necessitates tuning a laser to a very precise frequency and then carefully controlling its excitation power to deliver exactly a π-pulse.

Advances have been made on electrical excitation for quantum dots by bonding contacts to the photonic device [36] [37] [61] [38]. This excitation scheme usually relies on above band carrier injection, so although it can produce pulsed output there has to date not been a demonstration of electrical excitation with performance comparable to optical resonant excitation.

An alternative idea is to replace the large Ti:Sapphire laser that is a staple in optics laboratories by a small nW laser on the same chip as the quantum dot. The micro-laser could then be driven electrically and its output used to resonantly excite the single photon emitter.

This is a fascinating building block that could see accelerated adoption in a real-world setting, and has already been demonstrated in a proof-of-concept by ref. [62]. Their report is run at a 156 MHz repetition rate, whereas most Ti:Sapphire lasers are operated near 81 MHz. The microlaser and quantum dot source both still require cryogenic temperatures, necessitating quite a large operating footprint regardless.

Designing a photon source to meet all the requirements just presented is extremely challenging and there doesn't yet appear to be one clear dominant technology. Further discovery and technical ingenuity will certainly lead to refinements on existing form factors, as well as perhaps unearth previously unexplored avenues to single photon generation as well. For the remainder of the thesis the scope of discussion will be limited to the nanowire quantum dot photon source as it is a tried and true photonic device that has proven very good for the creation of engangled photon pairs [40] [60].

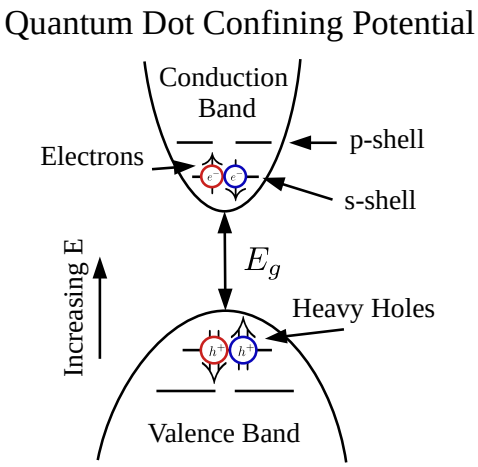

Figure 2.11: The confining potential in a semiconductor quantum dot is approximated by a harmonic oscillator. The s-shell in the conduction band can hold two electrons of opposite spin, while the valence band can hold two heavy holes also of opposite spin. The light holes have a lower energy still and do not enter the picture.

2.3 Nanowire Quantum Dots

The quantum photonic device featured in this thesis is a nanowire quantum dot. As briefly explained, the quantum dot creates a quantized energy level structure in a semiconductor crystal, limiting the energy levels electrons and holes can occupy. This is a result of its confining potential, approximated by a harmonic oscillator [63].

Created from adding a small amount of arsenic to InP, the quantum dot's energy transitions are found in the near-infrared around 890 nm. A diagram of the confining potential filled with an electron pair and a hole pair is shown in Figure 2.11. The electrons have an intrinsic angular momentum of $\frac{1}{2}$, so one electron in the s-shell will be spin-up with $S_z = +\frac{1}{2}$ while the other will be spin-down with $S_z = -\frac{1}{2}$. Conversely, the heavy holes are spin-$\frac{3}{2}$ quasiparticles and have spins of $S_z = \pm\frac{3}{2}$.

When combined, the total spin of an electron-hole pair, or exciton, can be -2, -1, 1 or 2. Only the spins of ± 1 from the $|\uparrow\Downarrow\rangle$ and $|\downarrow\Uparrow\rangle$ states couple to an optical field, and the ± 2 combinations like $|\uparrow\Uparrow\rangle$ and $|\downarrow\Downarrow\rangle$ are thus called the dark states. Note that the

light holes are also spin-$\frac{1}{2}$, so a bright state can also be created by $|\uparrow\Uparrow_{\frac{1}{2}}\rangle$ and $|\downarrow\Downarrow_{\frac{1}{2}}\rangle$, but since the light holes don't frequently appear with energies near the valence band edge this occurrence is rare. When it happens, the phenomenon is called heavy-light hole mixing.

The quantum dot emits light when an exciton recombines. As discussed in subsection 2.2.2, the typical semiconductors used for creating quantum dots have a high index of refraction which inhibits the created photons from being extracted. In the nanowire photonic source, the photons are given a preferred direction of emission along the length of the wire. A critical design parameter is the tapering angle on the top, which avoids an abrupt transition at the air interface and allows the electromagnetic field to leak out gradually, minimizing reflections.

Initially nanowires were created by locating a quantum dot on a layer of self-assembled quantum dots and etching a stucture around it. This top-down approach demonstrated the proof of principle but couldn't create the ideal tapering angle of 2°. Instead, a deterministic bottom-up growth technique was developed which could create the more gradual tapering angle [64].

A pioneering study of bottom-up pure-wurtzite nanowire quantum dot sources showed a $g^{(2)}(0) = 0.12$ under continuous-wave excitation, an exciton lifetime of $1.7(1)\,\text{ns}$, a 30% extraction efficiency, and significantly improved exciton linewidth [65] [66]. The mode was found to be very nearly Gaussian [57], and as a broadband photonic structure it produces high-quality entangled photon pairs [40] [60] [67]. The best values for $g^{(2)}(0)$ are found using quasi-resonant excitation at 870 nm to be $g_X^{(2)}(0) = 0.003 \pm 0.003$ and $g_{XX}^{(2)}(0) = 0.10 \pm 0.01$ for the exciton and biexciton respectively.

The entanglement between photons produced by this quantum dot source is a by product of the biexciton-exciton cascade, pictured in Figure 2.12. To start the cascade, the s-shell of the quantum dot's conduction band is filled with two electrons, while the valence band is occupied by two heavy holes. This is the biexciton state (XX). One of the electron hole pairs recombines and emits a circularly polarized photon, leaving just one remaining electron and hole in the confining potential as an exciton (X). A short time later the exciton recombines, emitting another circularly polarized photon with opposite polarization to the first.

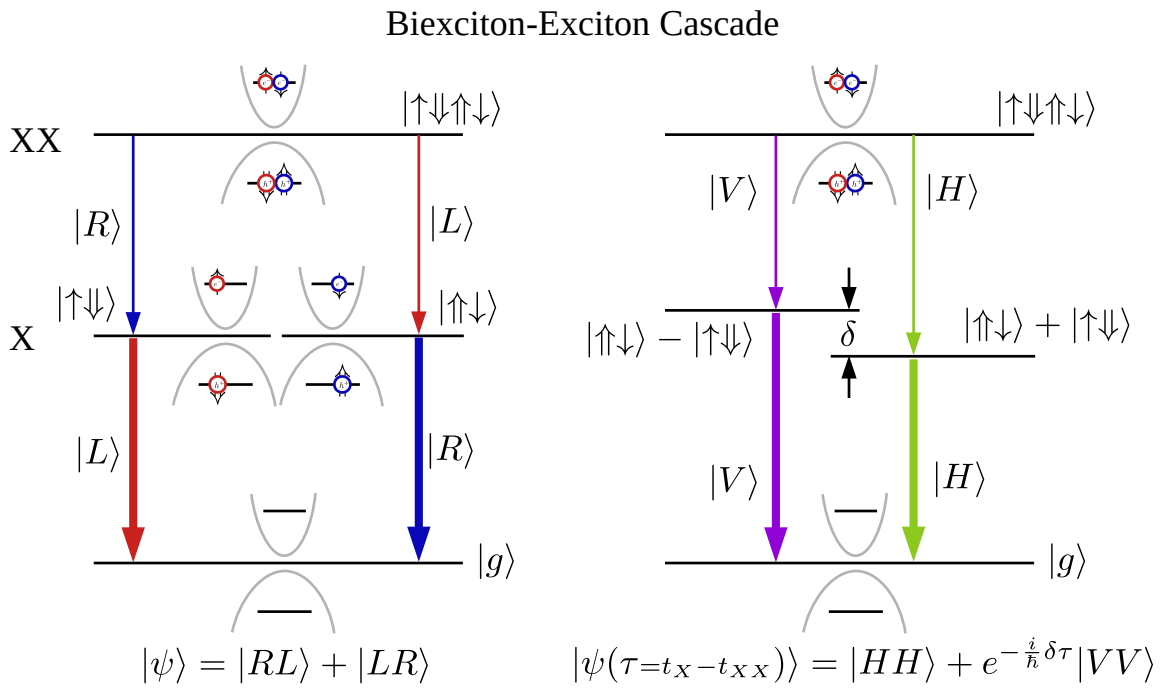

Figure 2.12: The biexciton-exciton cascade pictured without (left) and with (right) an energy splitting δ in the exciton's fine structure.

Two possibilities exist in the recombination of the first exciton pair. The initial state in the quantum dot is $|\uparrow\Downarrow\Uparrow\downarrow\rangle$ and the photons' mode is in the vacuum state $|0\rangle$, for a combined state of $|\uparrow\Downarrow\Uparrow\downarrow, 0\rangle$. Either the $|\uparrow\Downarrow\rangle$ or $|\downarrow\Uparrow\rangle$ electron-hole pair can recombine first, meaning the two possible exciton states are $|\uparrow\Downarrow, R_{XX}\rangle$ and $|\downarrow\Uparrow, L_{XX}\rangle$. Finally, after the second recombination takes place the system's state is $\frac{1}{\sqrt{2}}\left(|g, R_{XX}L_X\rangle + |g, L_{XX}R_X\rangle\right)$, with the quantum dot at its ground level and two photons entangled in polarization. This is the case shown at left in Figure 2.12.

It is expected that pure-wurtzite nanowires with a quantum dot embedded will not have any splitting in the fine structure, and measurements have confirmed that it is quite low at 1.2 µeV [40]. The quantum dot tested in chapter 5 has been found to have a fine structure splitting (FSS) of $\delta = 795.52(35)\,\mathrm{MHz}$ [67]. When this occurs the stationary states of the system are no longer in the $\{|R\rangle, |L\rangle\}$ basis, and are instead found in a rectilinear basis like $\{|H\rangle, |V\rangle\}$. This is due to the exchange interaction between the electron and heavy hole [68]. The energy diagram in this case is better represented by that on the right of Figure 2.12.

In both figures, the bold arrows show that the photon emitted by the exciton has a higher energy than the exciton from the biexciton. The difference stems from the Coulomb interaction between them. In the left figure, the arrows showing the transitions are related to the colors of the electrons and holes in the parabolic potentials. In the diagram with the fine structure the exciton level is represented by a pair of lines split by an energy δ. In this system the individual electron and hole spins are not good quantum numbers, and the stationary states are better represented by the superpositions $|\Uparrow\downarrow\rangle \pm |\uparrow\Downarrow\rangle$. This resulting two-photon state is still entangled, but precesses with time as indicated. The four arrows are no longer blue and red to show that the emission is not from any particular exciton, however the transitions with bold arrows remain higher energy.

To show that point, a spectrum was collected from the nanowire quantum dot studied in chapter 5 and is shown in Figure 2.13. It emits the first photon in a pair from the biexciton XX at $E_{XX} = 1.3867\,\mathrm{eV} \rightarrow \lambda_{XX} = 894.11\,\mathrm{nm}$ and the second from the exciton X at $E_X = 1.3889\,\mathrm{eV} \rightarrow \lambda_X = 892.67\,\mathrm{nm}$. The other sharp line is labeled X^- and is associated with the negatively charged exciton, where a recombination from the exciton happens in the presence of another electron.

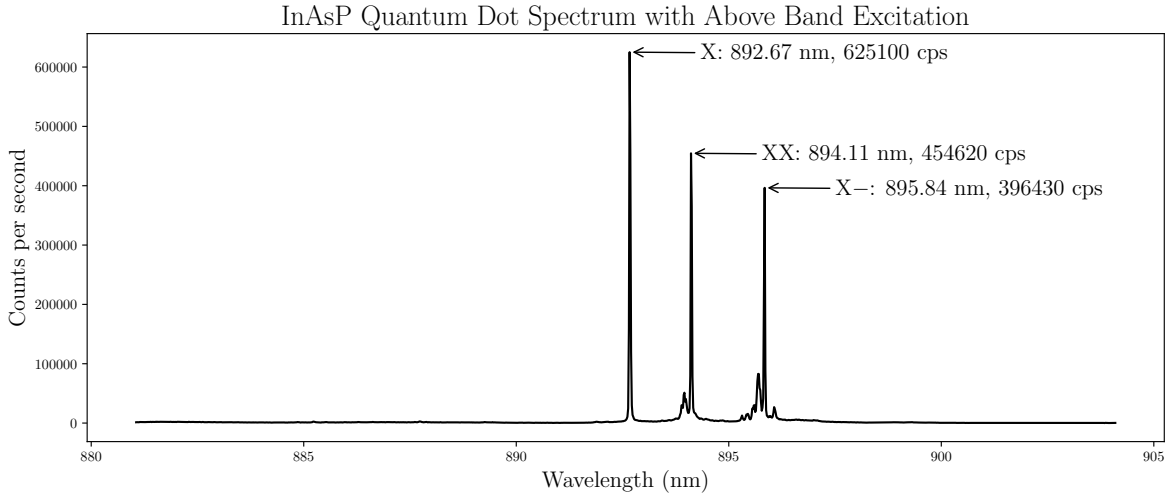

Figure 2.13: Spectrum collected from an InAsP quantum dot embedded in a pure wurtzite InP nanowire using above-band optical excitation at 830 nm. A pair of photons, one biexciton labeled "XX" and one exciton labeled "X" is emitted for every completed cascade.

The next chapter tackles the somewhat different topic of electro-optic modulation, with specific interest of using it to implement a rotating half-wave plate.

Chapter 3

Frequency Shifting by Electro-Optic Modulation: The Rotating Half-Wave Plate

3.1 Introduction

Crystals are considered precious in society due to their beauty in the presence of light. An engineer might instead wonder: given the properties of a crystal, what are the possible ways light can be strategically controlled with it? Many crystals are transparent in the optical or infrared spectrum, and due to their high index of refraction, feature good optical confinement. This chapter explores how one can up- or down-shift the frequency of light propagating through a lithium niobate ($LiNbO_3$) crystal waveguide by applying in-quadrature electric fields across the guiding region.

The most common example of guided light today is in the telecommunications industry, where optical fibres form the backbone of high-capacity links. These, however, are not made with crystals: most fibre-optic cables use silica glass for the core and cladding [69]. The guidance principles are similar for silica glass and lithium niobate, in that a waveguide core is doped to make its index of refraction higher than the surrounding material, which then

confines light due to total internal reflection. Crystal waveguides are typically inflexible, while silica glass can be bent, making the glass ideal for long fibre-optic cables.

On the other hand, lithium niobate is of particular interest as its index of refraction changes depending on an applied electric field. Additionally, the electric field's direction can control the birefringence of the crystal, making lithium niobate suitable for implementing a half-wave plate. A number of commercial optoelectronic devices, including amplitude and phase modulators, have been built based on these concepts ([70] Ch. 12, [71]).

The remainder of this chapter will present the mathematical concepts needed to show how a lithium niobate waveguide is capable of changing the frequency of light. First, in section 3.2 an introduction to the index ellipsoid and its relationship to electro-optically sensitive crystal waveguides is presented. Following that, section 3.3 discusses the Jones matrix approach to describing optical components and is used to show how a lithium niobate waveguide configured as a rotating half-wave plate changes an incident circularly-polarized beam. Section 3.4 goes on to discuss a specific physical implementation of the rotating half-wave plate.

3.2 Electro-Optic Effects in $LiNbO_3$

Maxwell's equations relate electric and magnetic fields $\mathbf{E}$ and $\mathbf{H}$ in a medium or free space. Electric fields result from the presence of electrical charges, and Gauss's law succinctly states that the divergence of the electric displacement flux density $\mathbf{D}$, related to electric field through the constitutive relationship $\mathbf{D} = \overline{\overline{\boldsymbol{\varepsilon}}}\,\mathbf{E}$, is equal to the charge density at the same point, that is $\Delta \cdot \mathbf{D} = \rho$. Here, $\overline{\overline{\boldsymbol{\varepsilon}}}$ is a rank two tensor describing the permittivity of the material and ρ is the charge density at the point in question. The permittivity of free space is a constant relative to which other material permittivities are defined, and has been measured to be $\varepsilon_0 \approx \frac{1}{36\pi} \times 10^{-9}\ \frac{\mathrm{F}}{\mathrm{m}}$.

Most of the time, Gauss's law is applied for isotropic materials, in other words, materials in which the relationship between electric field strength and displacement flux density is independent of direction. Under these conditions, $\mathbf{D} = \overline{\overline{\boldsymbol{\varepsilon}}}\,\mathbf{E}$ reduces to $\mathbf{D} = \varepsilon\,\mathbf{E}$, where ε is a scalar constant. The reason lithium niobate is chosen for creating a rotating half-wave

plate is that it is not isotropic, and beyond that the permittivity along various axes is controllable by applying an external electric field.

To gain an understanding of lithium niobate's unique properties, it serves to investigate its index ellipsoid. Chuang discusses the index ellipsoid in Ch. 6 and Ch. 12 of ref. [70], and some of the same steps are followed here.

3.2.1 The Index Ellipsoid

An index ellipsoid describes the directional-dependence of the index of refraction of a material. To begin, consider the diagonal permittivity tensor and its inverse, called the impermeability matrix $\overline{\overline{\mathbf{K}}}$, for a material whose permeability is the same as that of free space $\mu = \mu_0$. Using the definition for index of refraction $n_i = \sqrt{\frac{\varepsilon_i \mu_i}{\varepsilon_0 \mu_0}} = \sqrt{\frac{\varepsilon_i}{\varepsilon_0}}$ for $i \in \{x, y, z\}$, we find that

$$\overline{\overline{\boldsymbol{\varepsilon}}} = \begin{bmatrix} \varepsilon_x & 0 & 0 \\ 0 & \varepsilon_y & 0 \\ 0 & 0 & \varepsilon_z \end{bmatrix} = \varepsilon_0 \begin{bmatrix} n_x^2 & 0 & 0 \\ 0 & n_y^2 & 0 \\ 0 & 0 & n_z^2 \end{bmatrix}, \qquad \overline{\overline{\mathbf{K}}} = \overline{\overline{\boldsymbol{\varepsilon}}}^{-1} = \frac{1}{\varepsilon_0} \begin{bmatrix} \frac{1}{n_x^2} & 0 & 0 \\ 0 & \frac{1}{n_y^2} & 0 \\ 0 & 0 & \frac{1}{n_z^2} \end{bmatrix}.$$

In general, the permittivity tensor can be given with off-diagonal elements, however it is diagonalizable by choosing the right coordinate system for x, y, and z. This is called the principle coordinate system. Uniaxial medium have a recognizable optical axis in the principle coordinate system, a characteristic relationship captured by $\varepsilon_x = \varepsilon_y = \varepsilon \neq \varepsilon_z$.

The index ellipsoid is then defined using the impermeability matrix as $\varepsilon_0 \sum_{i,j=1}^{3} K_{ij} c_i c_j = 1$, where c_i represents the ith element of the tuple (x, y, z), and K_{ij} is the element from row i at column j of the impermeability matrix $\overline{\overline{\mathbf{K}}}$. Expanding in the principle axes for a uniaxial medium gives

$$\varepsilon_0 \sum_{i,j=1}^{3} K_{ij} c_i c_j = \frac{x^2}{n_o^2} + \frac{y^2}{n_o^2} + \frac{z^2}{n_e^2} = 1, \tag{3.1}$$

which is the equation for an ellipsoid in three dimensions. We have used the definition of $n_o = n_x = n_y$ for the ordinary wave solution and $n_e = n_z$ for the extraordinary wave. The distinction between ordinary and extraordinary waves is that the electric field of an

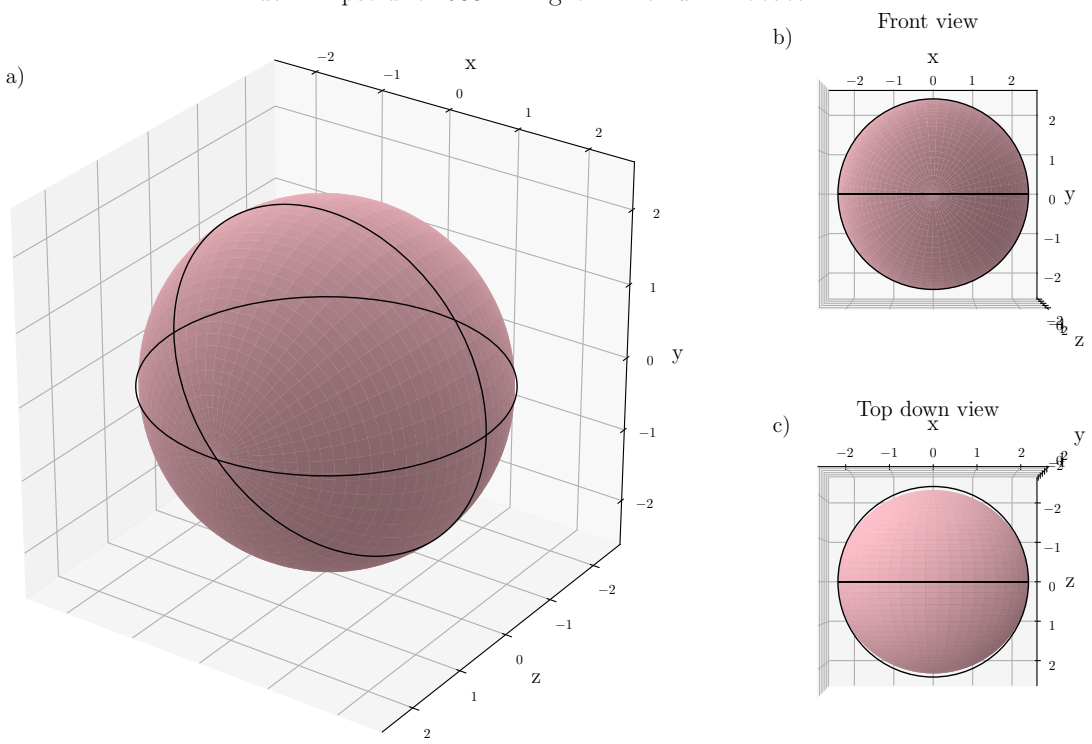

Figure 3.1: The index ellipsoid for lithium niobate.

ordinary wave has no component parallel to the optical axis. The shape of the ellipsoid helps gain intuition for how the index of refraction of a material is different for different directions of propagating electromagnetic waves.

The index ellipsoid for lithium niobate in the absence of an electric field is shown in Figure 3.1. The index of refraction for the ordinary and extraordinary waves have been measured for light at 633 nm to be $n_o = 2.297$ and $n_e = 2.208$. These two numbers are quite close in magnitude meaning the resulting ellipsoid is almost a sphere. Looking from the front as in Figure 3.1b one can see the ellipsoid fills a perfect circle, outlined in black. In contrast, the circle is not completely filled when looking from the top down in Figure 3.1c. This shows that the index ellipsoid is slightly compressed along the z-axis.

It starts to become interesting when the values K_{ij} depend on an external electric field applied to the crystal. To study this phenomenon, it helps to define $\overline{\overline{\mathbf{K}}} = \overline{\overline{\mathbf{K}}}_0 + \Delta\overline{\overline{\mathbf{K}}}$, where $\overline{\overline{\mathbf{K}}}_0$ is the impermeability matrix in the absence of an electric field and $\Delta\overline{\overline{\mathbf{K}}}$ describes the change when a field is present. Pockels characterized this relationship between the elements of $\Delta\overline{\overline{\mathbf{K}}}$ and an applied voltage $\mathbf{E} = E_x\hat{x} + E_y\hat{y} + E_z\hat{z}$ using what are now called Pockels' coefficients, r_{Ik}. The index I ranges from 1 to 6 instead of the usual 1 to 3, and in fact represents index pairs from our original ij labeling through the mapping

$$(ij) = \begin{bmatrix} 11 & 12 & 13 \\ 21 & 22 & 23 \\ 31 & 32 & 33 \end{bmatrix} \leftrightarrow \begin{bmatrix} 1 & 6 & 5 \\ 6 & 2 & 4 \\ 5 & 4 & 3 \end{bmatrix} = (I).$$

Only six indices are required for I as crystals exhibit symmetry in their structure, making the off-diagonal terms equivalent. Then $\Delta\overline{\overline{\mathbf{K}}}$, whose elements are given by $\Delta K_{ij} = \Delta K_I = \frac{1}{\varepsilon_0}\sum_{k=1}^{3} r_{Ik}E_k$, becomes

$$\begin{aligned}
\Delta\overline{\overline{\mathbf{K}}} =& \frac{1}{\varepsilon_0}\begin{bmatrix} r_{11}E_x + r_{12}E_y + r_{13}E_z & r_{61}E_x + r_{62}E_y + r_{63}E_z & r_{51}E_x + r_{52}E_y + r_{53}E_z \\ r_{61}E_x + r_{62}E_y + r_{63}E_z & r_{21}E_x + r_{22}E_y + r_{23}E_z & r_{41}E_x + r_{42}E_y + r_{43}E_z \\ r_{51}E_x + r_{52}E_y + r_{53}E_z & r_{41}E_x + r_{42}E_y + r_{43}E_z & r_{31}E_x + r_{32}E_y + r_{33}E_z \end{bmatrix} \\
= \begin{bmatrix} \Delta K_1 & \Delta K_6 & \Delta K_5 \\ \Delta K_6 & \Delta K_2 & \Delta K_4 \\ \Delta K_5 & \Delta K_4 & \Delta K_3 \end{bmatrix} \quad \longrightarrow \quad & \begin{bmatrix} \Delta K_1 \\ \Delta K_2 \\ \Delta K_3 \\ \Delta K_4 \\ \Delta K_5 \\ \Delta K_6 \end{bmatrix} = \frac{1}{\varepsilon_0}\begin{bmatrix} r_{11} & r_{12} & r_{13} \\ r_{21} & r_{22} & r_{23} \\ r_{31} & r_{32} & r_{33} \\ r_{41} & r_{42} & r_{43} \\ r_{51} & r_{52} & r_{53} \\ r_{61} & r_{62} & r_{63} \end{bmatrix}\begin{bmatrix} E_x \\ E_y \\ E_z \end{bmatrix}.
\end{aligned}$$

Pockel's coefficients are measured experimentally, and when needed are found in a database cataloging material properties. For lithium niobate, the nonzero Pockel's coefficients are, in units of $10^{-12}\,\mathrm{m\,V^{-1}}$: $r_{13} = r_{23} = 8.6$, $r_{33} = 30.8$, $r_{42} = r_{51} = 28$, $r_{22} = -r_{12} = -r_{61} = 3.4$, leading to the electro-optic tensor representation of $\Delta\overline{\overline{\mathbf{K}}}$ given

by

$$\begin{bmatrix}\Delta K_1\\ \Delta K_2\\ \Delta K_3\\ \Delta K_4\\ \Delta K_5\\ \Delta K_6\end{bmatrix} = \frac{1}{\varepsilon_0}\begin{bmatrix}0 & -r_{22} & r_{13}\\ 0 & r_{22} & r_{13}\\ 0 & 0 & r_{33}\\ 0 & r_{42} & 0\\ r_{42} & 0 & 0\\ -r_{22} & 0 & 0\end{bmatrix}\begin{bmatrix}E_x\\ E_y\\ E_z\end{bmatrix}$$

Therefore it is now possible to put all the pieces together and find the general index ellipsoid. First write $\overline{\overline{\mathbf{K}}}$ as

$$\overline{\overline{\mathbf{K}}} = \overline{\overline{\mathbf{K}}}_0 + \Delta\overline{\overline{\mathbf{K}}} = \frac{1}{\varepsilon_0}\begin{bmatrix}\frac{1}{n_o^2} & 0 & 0\\ 0 & \frac{1}{n_o^2} & 0\\ 0 & 0 & \frac{1}{n_e^2}\end{bmatrix} + \frac{1}{\varepsilon_0}\begin{bmatrix}-r_{22}E_y + r_{13}E_z & -r_{22}E_x & r_{42}E_x\\ -r_{22}E_x & r_{22}E_y + r_{13}E_z & r_{42}E_y\\ r_{42}E_x & r_{42}E_y & r_{33}E_z\end{bmatrix}$$

then use Equation 3.1 for the index ellipsoid to find

$$\begin{aligned}\varepsilon_0\sum_{i,j=1}^{3} K_{ij}c_ic_j = x^2\left(\frac{1}{n_o^2} - r_{22}E_y + r_{13}E_z\right) + y^2\left(\frac{1}{n_o^2} + r_{22}E_y + r_{13}E_z\right) + z^2\left(\frac{1}{n_e^2} + r_{33}E_z\right)\\ - xy\left(2r_{22}E_x\right) + yz\left(2r_{42}E_y\right) + xz\left(2r_{42}E_x\right) = 1.\end{aligned}$$

3.2.2 Index Ellipse for z-Propagation in $LiNbO_3$

It now helps define some further properties of our waveguide, to simplify the index ellipsoid. In particular, the waveguide is designed to propagate light along the z-axis, so we can remove the elements that don't contribute to permittivity in the xy-plane, that is we can set $z = 0$. Additionally, for our application the electric field will not be applied along the z-axis, meaning we can set $E_z = 0$. These changes result in a 2-dimensional ellipse, instead of the usual 3-dimensional ellipsoid, given by

$$x^2\left(\frac{1}{n_o^2} - r_{22}E_y\right) + y^2\left(\frac{1}{n_o^2} + r_{22}E_y\right) - xy\left(2r_{22}E_x\right) = 1. \tag{3.2}$$

Using our knowledge about the index ellipsoid, we can see that with a nonexistant electric field, the principle axes of the crystal are aligned along the natural principle axes,

and the index ellipse actually describes a circle.

$$\frac{x^2}{n_o^2} + \frac{y^2}{n_o^2} = 1. \tag{3.3}$$

This means the fast and slow axes propagate the phase of the light at the same velocity: there is no birefringence.

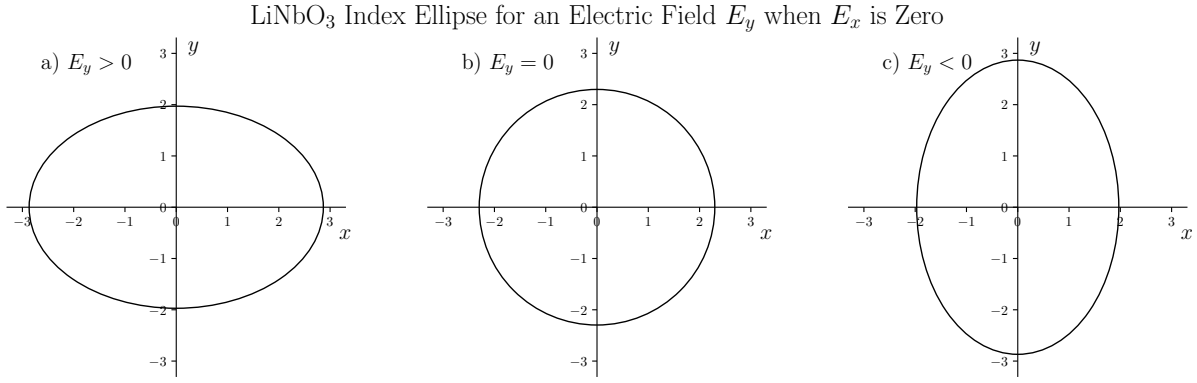

Figure 3.2: The index ellipse for lithium niobate in the presence of a y-directed electric field. In a), the fast axis is vertical and the slow axis is horizontal, meaning the vertical polarization of a propagating light wave will travel through the material faster than the horizontal component. The ellipse in b) is actually a circle, so lithium niobate is not birefringent for light traveling along z (out of the page) when E_y is zero. Making E_y negative as in c) results in the fast and slow axes switching such that the horizontal component of a propagating light wave will travel faster than the vertical component.

When an electric field is applied only along the y-axis, that is E_y becomes non-zero, the principle axes stay the same, however the equation becomes an ellipse compressed or stretched in the vertical ($\hat{y}$) direction.

$$x^2\left(\frac{1}{n_o^2} - r_{22}E_y\right) + y^2\left(\frac{1}{n_o^2} + r_{22}E_y\right) = 1 \tag{3.4}$$

In this case we can define different indices of refraction for the $\hat{x}$ and $\hat{y}$ directions like

$$\begin{aligned} \frac{1}{n_x^2} &= \frac{1}{n_o^2} - r_{22}E_y \\ \frac{1}{n_y^2} &= \frac{1}{n_o^2} + r_{22}E_y \end{aligned} \quad \longrightarrow \quad \begin{aligned} n_x &= \frac{n_o}{\sqrt{1 - r_{22}E_y n_o^2}} \\ n_y &= \frac{n_o}{\sqrt{1 + r_{22}E_y n_o^2}} \end{aligned},$$

allowing us to see that as E_y is increased, the denominator of n_x will decrease while the denominator of n_y will increase, therefore increasing n_x and decreasing n_y. A lower n results in a faster phase velocity for light, meaning that for high E_y, the y-axis will be the fast axis, while the x-axis will be the slow axis. If the polarity of E_y is switched, that is it is increased in the negative direction, the fast and slow axes will switch. These results for different values of E_y are pictured in Figure 3.2.

When an electric field is applied along the $\hat{x}$ direction, a different picture emerges. The index ellipse reduces to

$$\frac{x^2}{n_o^2} + \frac{y^2}{n_o^2} - xy\,(2r_{22}E_x) = 1.$$

It is clear that in this case, if we were to work backward to find the corresponding coefficients in the $\overline{\overline{\epsilon}}$ matrix, it would no longer be diagonal, meaning the principle axes have changed. Observe that by applying the transformation

$$x = \frac{1}{\sqrt{2}}\,(x' - y')\,, \qquad y = \frac{1}{\sqrt{2}}\,(x' + y')\,,$$

to the index ellipse, we arrive at a new index ellipse equation

$$x'^2\left(\frac{1}{n_o^2} - r_{22}E_x\right) + y'^2\left(\frac{1}{n_o^2} + r_{22}E_x\right) = 1.$$

Intuitively, the transformation sets up the (x', y') axes rotated counter-clockwise relative to the (x, y) axes by an angle of $\frac{\pi}{4}$. After the transformation, the index ellipse is diagonal with respect to the original x and y axes and features its principal axes along $\hat{x}'$ and $\hat{y}'$. By a similar line of reasoning as presented above for n_x and n_y, we find that the fast axis is along the $\hat{y}'$ direction when a positive electric field is applied along $\hat{x}$, $E_x > 0$, while the slow axis is along $\hat{x}'$. This follows from an analogous analysis of n_x' and n_y' and is shown in Figure 3.3.

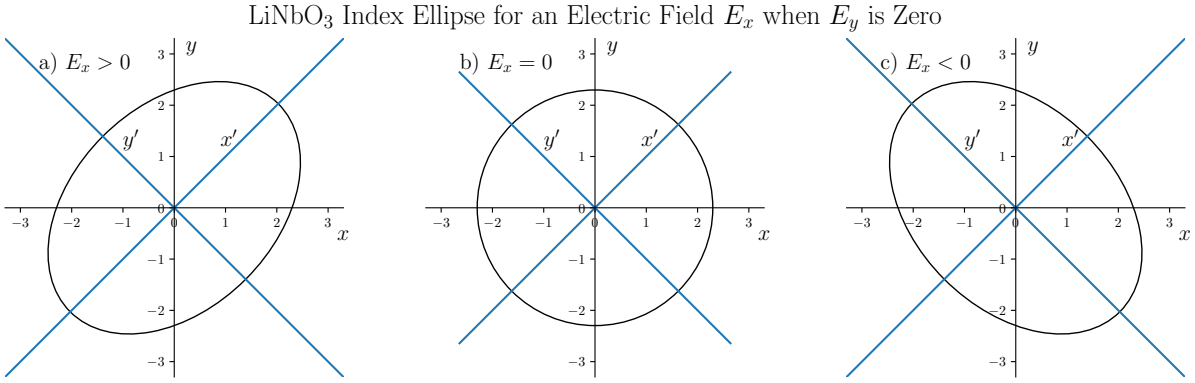

Figure 3.3: Applying an electric field along x causes the principal axes of the index ellipse to be rotated.

$$\begin{aligned} \frac{1}{n_x'^2} &= \frac{1}{n_o^2} - r_{22}E_x \\ \frac{1}{n_y'^2} &= \frac{1}{n_o^2} + r_{22}E_x \end{aligned} \quad \longrightarrow \quad \begin{aligned} n_x' &= \frac{n_o}{\sqrt{1 - r_{22}E_x n_o^2}} \\ n_y' &= \frac{n_o}{\sqrt{1 + r_{22}E_x n_o^2}} \end{aligned}$$

Using E_x and E_y as two control knobs it is possible to completely control the angle θ between the slow axis and $\hat{x}$. Since an ellipse is symmetric across its major and minor axes, rotations of $n\pi$ are indistinguishable, where $n \in \mathbb{Z}$ is an integer value. Figure 3.4 shows how the index ellipse can be rotated through an angle of π by setting E_y to a positive value, followed by E_x, then setting each of them negative in that same order.

Additionally, increasing the magnitudes of E_x and E_y causes an increasing phase difference to accumulate between the fast and slow components of a propagating light beam. Choosing the right values for E_x and E_y, it is possible to delay the phase of the component along the slow axis by exactly half of a wavelength, creating a have-wave plate rotated at an arbitrary angle θ. The next section builds on this concept to show how, by changing θ with respect to time, it is possible to make the half-wave plate spin.

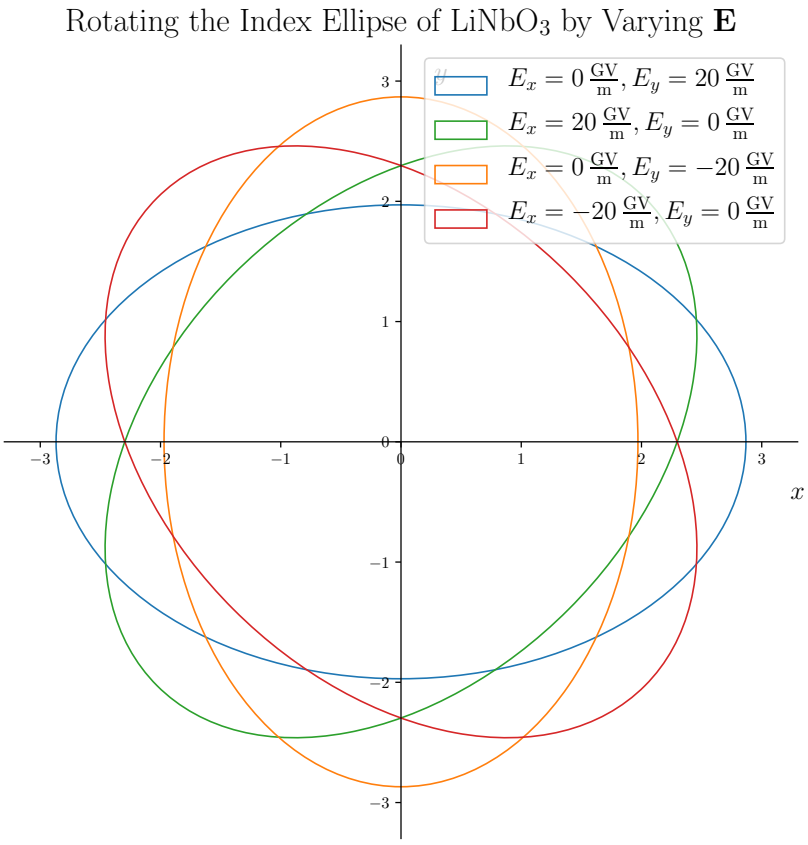

Figure 3.4: The index ellipse of $LiNbO_3$ can be rotated through an angle of π by varying each of E_x and E_y in sequence. Only ellipses where a single $\hat{x}$ or $\hat{y}$ component of electric field is non-zero are shown. Intermediate angles with the same birefringence not featured in the diagram can be formed by creating a linear combination of electric field along $\hat{x}$ and $\hat{y}$ so long as the total electric field, that is the Euclidean norm of $\mathbf{E} = \left[\begin{smallmatrix} E_x \\ E_y \end{smallmatrix}\right]$ given by $\|\mathbf{E}\| = \sqrt{E_x^2 + E_y^2}$, is held constant.

3.3 Rotating Half-Wave Plate

In the previous section we developed the mathematical tools required to describe a lithium niobate waveguide, and found that it is possible to create birefringence by applying an electric field in the xy-plane when light travels along $\hat{z}$. In this section, the goal is to determine what the field must look like if we want to fix the index ellipse's eccentricity but continually rotate it in time with some frequency ω_r. In other words, we want to make the ellipse's angle equal to $\theta = \omega_r t$ and hold $\|\mathbf{E}\|$ constant.

Before jumping in, however, it is worth taking a moment to discuss some motivation for this device. To do so, it helps to understand the polarization of light. For an electromagnetic wave propagating in free space, the polarization describes the ordered direction of the wave's electric field over adjacent wavelengths in a region of space. When light is polarized, its electric field has a pattern in space that repeats as one goes from one wavelength to the next. For example, the electric field vector for linearly polarized light propagating toward z, when projected onto the xy-plane, always points along a single direction $\hat{\mathbf{r}}(\alpha) = (\cos\alpha\,\hat{x}, \sin\alpha\,\hat{y})$. The magnitude of the projection varies depending on the choice of z and time t with a sinusoidal scalar amplitude $E(z,t) = A\cos(\omega t - k_z z)$ giving $\mathbf{E} = E\hat{\mathbf{r}}$.

Light from the sun and from most common light sources like light bulbs is unpolarized, in that the direction of the electric field at a certain place and moment in time is unpredictable and therefore doesn't have the order in its electric field as just described for polarized light. It is possible to polarize unpolarized light by using a polarizing filter, which rejects electromagnetic radiation unless its electric field is parallel to the permitted axis. This restores order in the electric field, so the output of a polarizing filter is linearly polarized light.

3.3.1 Jones Calculus

It helps to introduce some mathematical notation for describing light. Jones calculus, from ref. [72], is applicable in our case, where a beam with some wavevector $(0, 0, k_z)$ and a particular frequency ω propagates in the $+\hat{z}$ direction of the lab frame (toward an observer).

In an isotropic material, its electric field will reside in the xy-plane. Our propagating wave can then be generally written

$$\begin{bmatrix} A_{0x}e^{i(\omega t - k_z z + \phi_x)} \\ A_{0y}e^{i(\omega t - k_z z + \phi_y)} \end{bmatrix} = \begin{bmatrix} A_{0x}e^{i\phi_x} \\ A_{0y}e^{i\phi_y} \end{bmatrix} e^{i(\omega t - k_z z)}$$

where A_{0x} is the amplitude of the sinusoidally varying electric field in the $\hat{x}$ direction, while ϕ_x is its phase offset. A negative phase $\phi_x < 0$ represents a delay on the x-component's amplitude since for a chosen absolute phase one needs to advance time a little to offset increasingly more negative values of ϕ_x. A_{0x} and ϕ_x are both real. The same hold true for the variables in the $\hat{y}$ direction. It is worth noting that the Collett convention is used here for the phase term $\omega t - k_z z$ instead of the alternative Hecht convention of $k_z z - \omega t$.

Consider first the case where the electric field only exists along the x-axis for all values of z. In the laboratory frame this would be horizontally polarized light, and can be described by the Jones vector $\epsilon_H = \left[\begin{smallmatrix} A_{0x}e^{i\phi_x} \\ 0 \end{smallmatrix}\right]$. Conventionally, one will define a reference intensity (equal to the sum of the squares of the components of $\mathbf{E}$) and phase relative to which the other electric fields will be taken. In our case, after normalization, we find that the horizontally polarized case is just $\epsilon_H = |H\rangle = \left[\begin{smallmatrix} 1 \\ 0 \end{smallmatrix}\right]$. The ket $|H\rangle$ is Dirac notation for a column vector. The orthogonal polarization to $|H\rangle$ is vertical in the lab frame, and only has an electric field along $\hat{y}$ for all values of z. Its Jones vector is $|V\rangle = \left[\begin{smallmatrix} 0 \\ 1 \end{smallmatrix}\right]$. Observe that $|H\rangle$ and $|V\rangle$ are linearly independent and form an orthonormal basis for the two-dimensional complex vector space $\mathbb{C}^2$ we're concerned with here.

So far, we have not encountered a case where the relative phase between the $\hat{x}$ and $\hat{y}$ components was important. Consider the Jones vector $|D\rangle = \frac{1}{\sqrt{2}}\left[\begin{smallmatrix} 1 \\ 1 \end{smallmatrix}\right]$. Since no phase difference exists between the horizontal and vertical components, this vector represents linearly polarized light with an equal component of electric field in the $\hat{x}$ and $\hat{y}$ directions. The factor of $\frac{1}{\sqrt{2}}$ appears because of the normalization condition. In this case, the linearly polarized light is diagonal, with the electric field's direction at an angle exactly $\frac{\pi}{4}$ from both the $\hat{x}$ and $\hat{y}$ axes. We can also define the antidiagonal Jones vector as $|A\rangle = \frac{1}{\sqrt{2}}\left[\begin{smallmatrix} 1 \\ -1 \end{smallmatrix}\right]$. Again, $|D\rangle$ and $|A\rangle$ are linearly independent, and form another orthonormal basis for $\mathbb{C}^2$.

Finally, we come to an example with a relative phase shift between the horizontal and vertical components of the electric field. Circularly polarized light has an electric field

vector whose length is constant for a given pair of space and time values (z, t), but whose angle swings around the propagation axis.

For fixed moment in time, this can be pictured as a corkscrew pattern. Our Jones vectors use a right handed coordinate system as viewed from $z = +\infty$, so a right-handed circularly polarized beam, whose most positive $\hat{y}$ component is delayed by a quarter wave length with respect to the position of the most positive field on $\hat{x}$, is written $|R\rangle = \frac{1}{\sqrt{2}} \left[\begin{smallmatrix} 1 \\ e^{-i\frac{\pi}{2}} \end{smallmatrix} \right] = \frac{1}{\sqrt{2}} \left[\begin{smallmatrix} 1 \\ -i \end{smallmatrix} \right]$. This can be visualized by pointing one's right thumb in the $+\hat{z}$ direction with extended fingers along $+\hat{x}$. Assuming that one's hand is fixed at a position z where the electric field is initially at its maximum along $\hat{x}$, by making a fist, one's fingertips trace out the tip of the electric field vector as time advances: the positive $\hat{y}$ component is delayed with respect to $\hat{x}$. Conversely, a left-handed circularly polarized beam is $|L\rangle = \frac{1}{\sqrt{2}} \left[\begin{smallmatrix} 1 \\ i \end{smallmatrix} \right]$.

Any lossless optical rotator or retardation plate can be represented by a 2×2 unitary matrix, called a Jones matrix. The unitary property enforces its lossless quality, in that the total intensity of the beam before and after the optical component will be preserved. The matrix representing our plate of interest, the half-wave plate, can be decomposed in to a phase difference along a specific set of axes, $W(\phi) = \left[\begin{smallmatrix} e^{-i\phi/2} & 0 \\ 0 & e^{i\phi/2} \end{smallmatrix} \right]$ and a rotation into the axes of interest $R(\theta) = \left[\begin{smallmatrix} \cos\theta & -\sin\theta \\ \sin\theta & \cos\theta \end{smallmatrix} \right]$. The phase difference ϕ is applied by delaying the component along $\hat{x}$ by $\frac{\phi}{2}$ and advancing the component along $\hat{y}$ by an equal amount. The rotator rotates a particular vector counter-clockwise by the angle θ. Thus we find the expression for a half wave plate rotated with its slow axis at an angle θ with respect to $\hat{x}$ to be

$$
\begin{aligned}
\mathrm{HWP}(\theta) &= \mathrm{R}(\theta)\mathrm{W}(\pi)\mathrm{R}(-\theta) \\
&= \begin{bmatrix} \cos\theta & -\sin\theta \\ \sin\theta & \cos\theta \end{bmatrix} \begin{bmatrix} e^{-i\frac{\pi}{2}} & 0 \\ 0 & e^{i\frac{\pi}{2}} \end{bmatrix} \begin{bmatrix} \cos(-\theta) & -\sin(-\theta) \\ \sin(-\theta) & \cos(-\theta) \end{bmatrix} \\
&= \begin{bmatrix} e^{-i\frac{\pi}{2}}\cos\theta & -e^{i\frac{\pi}{2}}\sin\theta \\ e^{-i\frac{\pi}{2}}\sin\theta & e^{i\frac{\pi}{2}}\cos\theta \end{bmatrix} \begin{bmatrix} \cos\theta & \sin\theta \\ -\sin\theta & \cos\theta \end{bmatrix} \\
&= \begin{bmatrix} e^{-i\frac{\pi}{2}}\cos^2\theta + e^{i\frac{\pi}{2}}\sin^2\theta & e^{-i\frac{\pi}{2}}\cos\theta\sin\theta - e^{i\frac{\pi}{2}}\cos\theta\sin\theta \\ e^{-i\frac{\pi}{2}}\cos\theta\sin\theta - e^{i\frac{\pi}{2}}\cos\theta\sin\theta & e^{-i\frac{\pi}{2}}\cos^2\theta + e^{i\frac{\pi}{2}}\sin^2\theta \end{bmatrix} \\
&= \begin{bmatrix} \cos\frac{\pi}{2} - i\sin\frac{\pi}{2}\cos 2\theta & -i\sin\frac{\pi}{2}\sin 2\theta \\ -i\sin\frac{\pi}{2}\sin 2\theta & \cos\frac{\pi}{2} + i\sin\frac{\pi}{2}\cos 2\theta \end{bmatrix} \\
&= \begin{bmatrix} -i\cos 2\theta & -i\sin 2\theta \\ -i\sin 2\theta & i\cos 2\theta \end{bmatrix} \\
&= -i \begin{bmatrix} \cos 2\theta & \sin 2\theta \\ \sin 2\theta & -\cos 2\theta \end{bmatrix}
\end{aligned}
$$

Again, the input variable θ is the angle between the slow axis and $\hat{x}$. The fourth step used the double angle formulas and collected the conjugate exponential terms into sines and cosines. Only the final step made use of the specific value of the phase delay, and we could have equivalently used a generic phase ϕ instead.

To perform a sanity check, let's pick an angle for θ and observe how our half-wave plate modifies different input polarizations. Try $\theta = 0$, which represents a half-wave plate whose slow axis is along $\hat{x}$. In this case, any $\hat{x}$ component of an incoming beam's electric field should be delayed by a phase of $\phi = \pi$ with respect to the $\hat{y}$ component. A Jones matrix is applied to a Jones vector by multiplying on the left. Therefore, for an arbitrary normalized input $|\psi\rangle = \alpha\,|H\rangle + \beta\,|V\rangle$, where $\alpha, \beta \in \mathbb{C}$ and $|\alpha|^2 + |\beta|^2 = 1$, we have

$$
\mathrm{HWP}(0)\,|\psi\rangle = -i \begin{bmatrix} 1 & 0 \\ 0 & -1 \end{bmatrix} \begin{bmatrix} \alpha \\ \beta \end{bmatrix} = \begin{bmatrix} -i\alpha \\ i\beta \end{bmatrix}.
$$

It is clear that the $\hat{x}$ component acquires a phase of $-i = e^{-i\frac{\pi}{2}}$, and is therefore delayed by $\phi_x = -\frac{\pi}{2}$, whereas the $\hat{y}$ component is advanced by $\frac{\pi}{2}$, or in other words $\phi_y = \frac{\pi}{2}$. The

total phase difference acquired by passing through the half-wave plate then is a total of π, representing a half wavelength, as desired.

Consider now the effect of rotating the half wave plate counterclockwise at some frequency ω_r, such that $\theta = \omega_r t$. The resulting Jones matrix is

$$\mathrm{RHWP}(\omega_r) = -i \begin{bmatrix} \cos 2\omega_r t & \sin 2\omega_r t \\ \sin 2\omega_r t & -\cos 2\omega_r t \end{bmatrix},$$

and we can inspect its effect on an incoming circularly polarized beam. The calculation looks like

$$\mathrm{RHWP}(\omega_r)\,|R\rangle = -i \begin{bmatrix} \cos 2\omega_r t & \sin 2\omega_r t \\ \sin 2\omega_r t & -\cos 2\omega_r t \end{bmatrix} \frac{1}{\sqrt{2}} \begin{bmatrix} 1 \\ -i \end{bmatrix} = \frac{-ie^{-i2\omega_r t}}{\sqrt{2}} \begin{bmatrix} 1 \\ i \end{bmatrix} = -ie^{-i2\omega_r t}\,|L\rangle\,.$$

Therefore, in passing through the rotating half wave plate, a right circularly polarized wave is turned into a left circularly polarized wave with an additional global phase. The global phase consists of a fixed component, $-i$, and a time-dependent component, $e^{-i2\omega_r t}$. Working backwards to find the electric fields of the wave results in the Jones vector

$$\begin{bmatrix} A_0 \\ A_0 e^{i\frac{\pi}{2}} \end{bmatrix} e^{i((\omega - 2\omega_r)t - k_z z - \frac{\pi}{2})}. \tag{3.5}$$

The resulting wave has had its frequency converted to the a new, lower frequency $\omega_c = \omega - 2\omega_r$. Working through the same process for an input of $|L\rangle$ gives

$$\mathrm{RHWP}(\omega_r)\,|L\rangle = -i \begin{bmatrix} \cos 2\omega_r t & \sin 2\omega_r t \\ \sin 2\omega_r t & -\cos 2\omega_r t \end{bmatrix} \frac{1}{\sqrt{2}} \begin{bmatrix} 1 \\ i \end{bmatrix} = \frac{-ie^{i2\omega_r t}}{\sqrt{2}} \begin{bmatrix} 1 \\ i \end{bmatrix} = -ie^{i2\omega_r t}\,|R\rangle\,.$$

We find that in this case the polarization is once again changed to the its orthogonal pair, however the rotation of the half-wave plate has added energy to the light.

Our objective is to accomplish this same result using the litium niobate waveguide as discussed in section 3.2. The following section studies how such a device needs to be driven to achieve a rotating half-wave plate effect.

3.3.2 Electrically Driving a $LiNbO_3$ Rotating Half-Wave Plate

Now that we have a direction in sight, we must find what electrical amplitudes to apply to our lithium niobate waveguide such that its optical axes rotate at a frequency ω_r. The constraint is that the index ellipse's eccentricity remains constant throughout the rotation.

Recall the general form for the index ellipse in lithium niobate from equation 3.2:

$$x^2\left(\frac{1}{n_o^2} - r_{22}E_y\right) + y^2\left(\frac{1}{n_o^2} + r_{22}E_y\right) - xy\left(2r_{22}E_x\right) = 1.$$

We must find a general set of principle axes which diagonalizes the index ellipse. They will take the form

$$x = x'\cos\theta - y'\sin\theta, \qquad y = x'\sin\theta + y'\cos\theta$$

where again θ is the angle by which the (x', y') axes are rotated counterclockwise with respect to (x, y). The resulting index ellipse in the (x', y') coordinate system is

$$\begin{aligned} &x'^2\left(\cos^2\theta(n_o^{-2} - r_{22}E_y) + \sin^2\theta(n_0^{-2} + r_{22}E_y) - \sin(2\theta)r_{22}E_x\right) \\ &+ y'^2\left(\sin^2\theta(n_o^{-2} - r_{22}E_y) + \cos^2\theta(n_0^{-2} + r_{22}E_y) + \sin(2\theta)r_{22}E_x\right) \\ &+ 2r_{22}x'y'\left(E_y\sin 2\theta - E_x\cos 2\theta\right) = 1, \end{aligned}$$

and by setting $E_y\sin 2\theta = E_x\cos 2\theta$ we can eliminate the cross term and resolve the principle axes. Therefore, $E_x = E_y\frac{\sin 2\theta}{\cos 2\theta}$, and we are left with

$$x'^2\left(\frac{1}{n_o^2} - \frac{r_{22}E_y}{\cos 2\theta}\right) + y'^2\left(\frac{1}{n_o^2} + \frac{r_{22}E_y}{\cos 2\theta}\right) = 1.$$

We can interpret the result as follows. The principle axes of lithium niobate can be set to an arbitrary angle θ with respect to the laboratory frame. The birefringence of the waveguide, given by the orientation and eccentricity of the index ellipse, then depends on both the angle θ and the applied electric field in the $\hat{y}$ direction E_y. The choice for the electric field along $\hat{x}$ is fixed by the relationship $E_x = E_y\frac{\sin 2\theta}{\cos 2\theta}$.

For our rotating wave plate to feature a constant phase delay throughout its entire operation we know that the eccentricity of the ellipse must remain independent of θ. This

will only be true if

$$\begin{aligned} E_y &= E_0 \cos 2\theta \\ E_x &= E_y \frac{\sin 2\theta}{\cos 2\theta} = E_0 \sin 2\theta \end{aligned} \qquad \longrightarrow \qquad x'^2 \left(n_o^{-2} - r_{22} E_0\right) + y'^2 \left(n_o^{-2} + r_{22} E_0\right) = 1.$$

Additionally, since we want our rotating half-wave plate's principle axes to change with time, we can plug in $\theta = \omega_r t$ and arrive at our final result for the shape of the applied electric field

$$E_x = E_0 \sin 2\omega_r t, \qquad E_y = E_0 \cos 2\omega_r t.$$

The final requirement our rotating half-wave plate must satisfy is that it should in fact be a half-wave plate. The total phase delay for the lithium niobate device is a function of the index ellipse, which describes the speed at which different linear polarization components travel in the material, and device length L, or how long the light travels in the material for. Since device length is typically fixed, the half-wave condition can be met by choosing a value for E_0 that gives the desired difference in index of refraction for the fast and slow axes. We can calculate $n_{x'}$ and $n_{y'}$ to help determine the best choice of E_0.

$$\begin{aligned} \frac{1}{n_{x'}^2} &= n_o^{-2} - r_{22} E_0 \\ \frac{1}{n_{y'}^2} &= n_o^{-2} + r_{22} E_0 \end{aligned} \qquad \longrightarrow \qquad \begin{aligned} n_{x'} &= \frac{n_o}{\sqrt{1 - r_{22} E_0 n_o^2}} \\ n_{y'} &= \frac{n_o}{\sqrt{1 + r_{22} E_0 n_o^2}} \end{aligned}$$

$$\Delta n = n_{x'} - n_{y'} = \frac{n_o}{\sqrt{1 - r_{22} E_0 n_o^2}} - \frac{n_o}{\sqrt{1 + r_{22} E_0 n_o^2}}$$

Then, using the equation for phase retardation given by $\Gamma = \frac{\omega}{c}\left(n_s - n_f\right) L$, where c is the speed of light in free space and n_s and n_f are the indices of refraction for the slow and fast axes, and setting $\Gamma = \pi$ for a half-wave delay we find

$$\frac{1}{\sqrt{1 - r_{22} E_0 n_o^2}} - \frac{1}{\sqrt{1 + r_{22} E_0 n_o^2}} = \frac{c\pi}{L\omega n_o} \tag{3.6}$$

.

This equation can be solved numerically to determine the right E_0 to use for the waveguide in question. As an example, using a device length of $L = 3\,\text{cm}$ and light with a

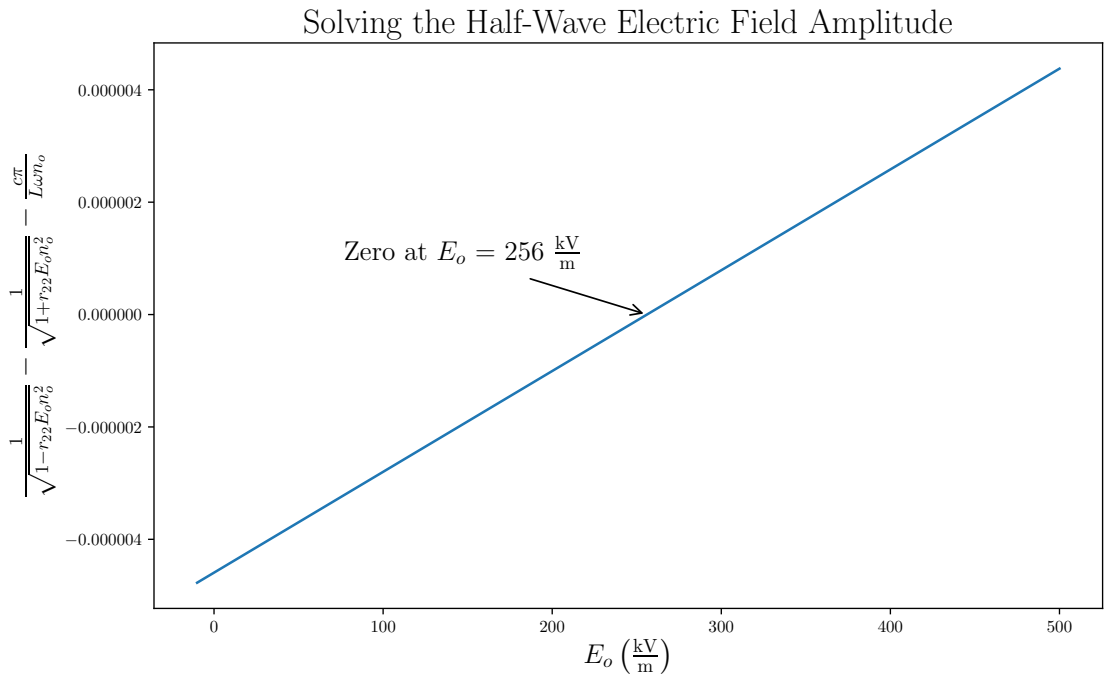

Figure 3.5: The numerical solution for E_0 is shown for a device length of $L = 3$ cm and 633 nm light. This is done by plotting the indicated equation and looking for a zero crossing. In this case the result is $E_0 = 256\ \frac{\mathrm{kV}}{\mathrm{m}}$.

wavelength $\lambda = 633\,\mathrm{nm}$, we find the required electric field strength is $E_0 = 256\,\frac{\mathrm{kV}}{\mathrm{m}}$. The solution is pictured in Figure 3.5

At this point all of the required constraints for the rotating half-wave plate have been satisfied. The main conclusion is that applying an in-quadrature electric field with magnitude E_0 given by Equation 3.6 and frequency $2\omega_r$ will cause an incident circularly polarized beam to be shifted in frequency by $2\omega_r$ and reversed in polarization.

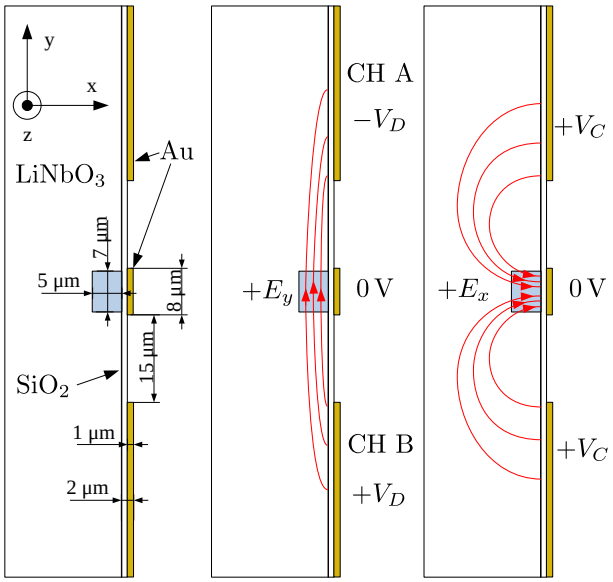

Figure 3.6: A to-scale drawing of the SRICO EOM. [Left] Dimensions of the device. [Center] A differential voltage creates a field in the y direction. [Right] Conversely, an x-directed field is created with a common voltage. An insulating layer of silicon dioxide separates the electrodes from the lithium niobate crystal.

3.4 SRICO Device

Chapter 4 and chapter 5 show experimental results of frequency shifting using an electro-optically modulated rotating half-wave plate. The EOM in question was a prototype produced by SRICO[1]. A schematic of the device's electrode configuration is shown in Figure 3.6.

The image shows the crystal as looking at one of its faces. The waveguided region is shaded in blue and sits just underneath a gold ground electrode. The top and bottom electrodes are driven independently. When the electrodes have opposite voltages they create a y-directed electric field in the waveguiding region, whereas a common voltage on both induces an x-directed electric field, indicated by the red lines.

Axes are indicated on the figure and show the choice of xyz. It has been conveniently chosen to be the same as xyz in the lab frame. Positioned looking at the page the reader is thus placed at the observing position of $z = +\infty$, consistent with the earlier analysis in this section. Applying a positive voltage to channel B in the differential case thus creates a positive electric field in the y direction.

Given the configuration of the electrodes it should not be expected that a similar-strength common or differential voltage each create the same magnitude field in the waveguide region. It is instead expected that much larger differential voltages are required to maintain the constant magnitude of the **E** field as compared to common voltage, $V_D > V_C$. However, the in-quadrature condition for the E field can be maintained even if the voltage amplitudes required are not equal so long as the correct phase delay between the signal on A and B is chosen.

[1] `https://www.srico.com`

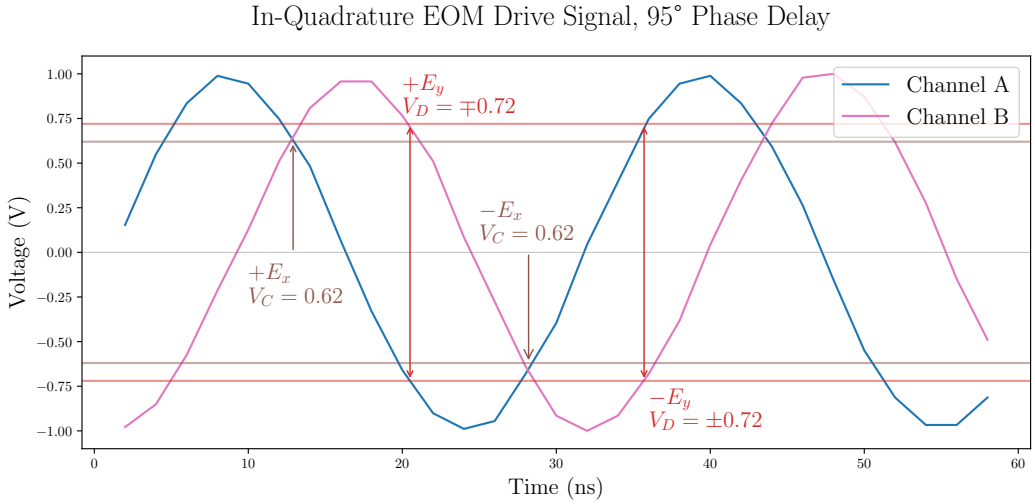

Figure 3.7: An in-quadrature drive signal for channels A and B.

$$\begin{aligned} E_x &= |E|\cos(2\omega_r t) = \alpha V_C \\ E_y &= |E|\sin(2\omega_r t) = \beta V_D \end{aligned} \longrightarrow \begin{aligned} V_C &= \frac{|E|}{\alpha}\cos(2\omega_r t) \\ V_D &= \frac{|E|}{\beta}\sin(2\omega_r t) \end{aligned}$$

$$\begin{aligned} V_A &= V_C - V_D \\ V_B &= V_C + V_D \end{aligned} \longrightarrow \begin{aligned} V_A &= |E|\sqrt{\frac{1}{\alpha^2}+\frac{1}{\beta^2}}\cos\left(2\omega_r t - \arctan\frac{\alpha}{\beta}\right) \\ V_B &= |E|\sqrt{\frac{1}{\alpha^2}+\frac{1}{\beta^2}}\sin\left(2\omega_r t + \arctan\frac{\alpha}{\beta}\right) \end{aligned}$$

This way the voltage magnitude on channel A and B can be equal, but the corresponding ratio of common and differential voltages are adjustable. The phase adjustment required is dictated by the ratio of α to β as shown.

The graph in Figure 3.7 displays a sinusoidal signal that has been found to produce good results with the procedure in subsection 4.4.1. The frequency is set to 325 MHz, and channel B is delayed by a 95° phase shift. The common and differential voltage points are indicated, along with the electric field direction they create.

Following the significant points it can be seen that the electric field in the waveguide region rotates counter clockwise in the lab frame at positive angular velocity $2\omega_r$, making

the half-wave plate rotate at one-half that, or ω_r. Referring back to Equation 3.5 it can be seen that a counter-clockwise rotation like this is expected to reduce the frequency of right-hand circularly polarized light by $2\omega_r$, which will be found is the exact result observed in subsection 4.4.2.

3.5 Conclusion

It has long been known that by rotating a half-wave plate one can change the frequency of electromagnetic radiation. In 1947, Fox put forward a variable microwave phase changer built on this principle [73], however mechanically rotating the waveguide limited the frequency by which waves could be up- or down-converted. Use of the electro-optic effect for this purpose was demonstrated in 1962 in ref. [74], however peak-to-peak voltages of 2000 V were required, again limiting the usability of frequency conversion.

A different approach is to use a device like Qin *et al.* tested in ref. [75]. They demonstrated successful frequency conversion of 100 MHz and 2 GHz, for 780 nm light, with a voltage of 18 V. In the 2 GHz case, their extinction ratio between the desired peak and the first harmonic was greater than 20 dB. While 2 GHz is still a very small frequency shift in optical terms, it is enough to be applied in experiments involving quantum optics.

In particular, quantum dots are capable of producing entangled photon pairs through a process known as the biexciton-exciton cascade. Due to unavoidable imperfections resulting from the fabrication process, a fine structure is induced in the otherwise degenerate exciton levels, causing a precession of the excitonic state for an unpredictable duration before the exciton spontaneously decays. This causes a large proportion of the emitted entangled photon pairs to be unusable, as they are not all a consistent Bell state. Since the fine structure for some quantum dots is only on the order of 800 MHz [67] it can be corrected for with an electro-optically controlled rotating half-wave plate [1]. While the theory supports this, the real truth will emerge from the experiment!

Chapter 4

Frequency Shifting a Narrow-Band Laser

The first experimental step toward frequency-shifting photons from a quantum dot is to demonstrate the proof-of-principle on a monochromatic beam of light. To that end, this chapter presents the building blocks for operating the EOM, and shows how it affects near-infrared light from a narrow-band laser. First, the EOM is driven with slowly varying voltages to help gain an understanding of its operating principles, and then higher frequency RF signals are used to create a rotating half-wave plate as described in chapter 3. Data collected from both experiments is analyzed and discussed herein.

The EOM was produced by SRICO[1].

4.1 Experimental Setup

The objective of this chapter is to show that an EOM can indeed convert the frequency of light up or down by a precise and controllable amount ω_0. To begin, the experiment requires a light source with a well-defined frequency. A detector for measuring the light's intensity at the output of the EOM is also necessary.

[1] `https://www.srico.com`

As presented in chapter 3, a direct current (DC) voltage on the EOM's electrodes causes birefringence in the crystal, which makes it act like a waveplate of some retardance at some angle. The experimental setup must allow us to quantify both the retardance and angle with respect to applied electrode voltages.

Once it has been demonstrated that the EOM can indeed behave like a half-wave plate under DC conditions, and that the angle of the waveplate's fast axis can be set arbitrarily, we can proceed with an experiment studying the EOM's behavior under alternating current (AC) drive signals. According to the theory, it should be possible to then observe the up- or down-conversion of light from our monochromatic source.

Many components required for these two experiments are similar. In particular, a Thorlabs DBR852P narrow-band near-infrared diode laser was selected as the light source. Its linewidth is 10 MHz, and the wavelength can be tuned using temperature adjustments around 852 ± 0.7 nm. This wavelength is near enough the QD's exciton line, which sits at 892.3 nm. The EOM's waveguide was designed to be single mode for both the laser and the quantum dot's exciton emission.

Both the DC and AC experiments require precise control and measurement of polarization, and as such a selection of polarizing beam splitters (PBSs), HWPs, and quarter-wave plates (QWPs) were acquired. The PBSs were purchased from Thorlabs (PBS252), and are broadband optical components transmitting only one polarization with an extinction ratio of 1000:1. The waveplates are achromatic, and are designed for light between 700 and 1000 nm.

In order to set the beam's path, irises were also ordered and put on the optical table. Their function was twofold: they provided a way align the beam when placing mirrors, and also acted as spatial filters for the stray light exiting the EOM's crystal. Coupling in and out of the waveguide on the EOM is discussed further in section 4.2.

Finally, in each experiment, the output signal must be measured. Since the laser's output power is on the order of milliwatts, it is detectable by a standard photodiode. To collect polarization tomography data from the DC voltage experiment, one amplified photodiode was used.

The AC experiment additionally required a way to quantify the spectral components of

the light following propagation through the EOM. The right tool for the job is a scanning Fabry-Perot (FP) interferometer. For this experiment, an FP with an free spectral range (FSR) of 1.5 GHz was sufficient, since the target value for ω_0 is no more than 0.5 GHz, which is less than half the FSR. The result is that our desired signal's sidebands will not overlap with the sidebands from the next neighboring peak in the output signal from the scanning FP. A second run of this same experiment using an FP with a 10 GHz FSR is also discussed.

Both the DC and AC experiments first require light coupled into the waveguide on the EOM, a topic which the next section addresses.

4.2 Waveguide Coupling

The most basic experiment with the EOM involves sending light through its waveguide and observing the mode. Once this step is complete, voltages can be applied to the EOM's electrodes and the polarization change can be quantified.

Before any other experiment with the EOM can be run, it must be shown that light from the laser can be coupled into the waveguide and the result observed. To do so, the EOM was mounted on a five-axis stage with a 3 cm lens positioned at the waveguide's output to collimate the beam. A microscope objective lens (Olympus LMPLN5XIR) was mounted on an additional four-axis stage in front of the EOM to focus the incoming beam onto the waveguide's front facet. Both stages and coupling lenses can be seen in Figure 4.1.

The stages were mounted on a portable optical breadboard making it easy to build the preliminary experimental setup for the EOM on an auxiliary optical table before transitioning the EOM and associated coupling optics to the optical table housing the quantum dot. Form-factor measurements were taken so as to minimize the adjustments necessary for the transition: the beam height on the two tables was chosen to be the same and was based on the height of the spectrometer inputs on the main optical table, while the width and length of the breadboard were chosen as a function of the space available. This accelerated integration of the EOM into the experiment performed in chapter 5.

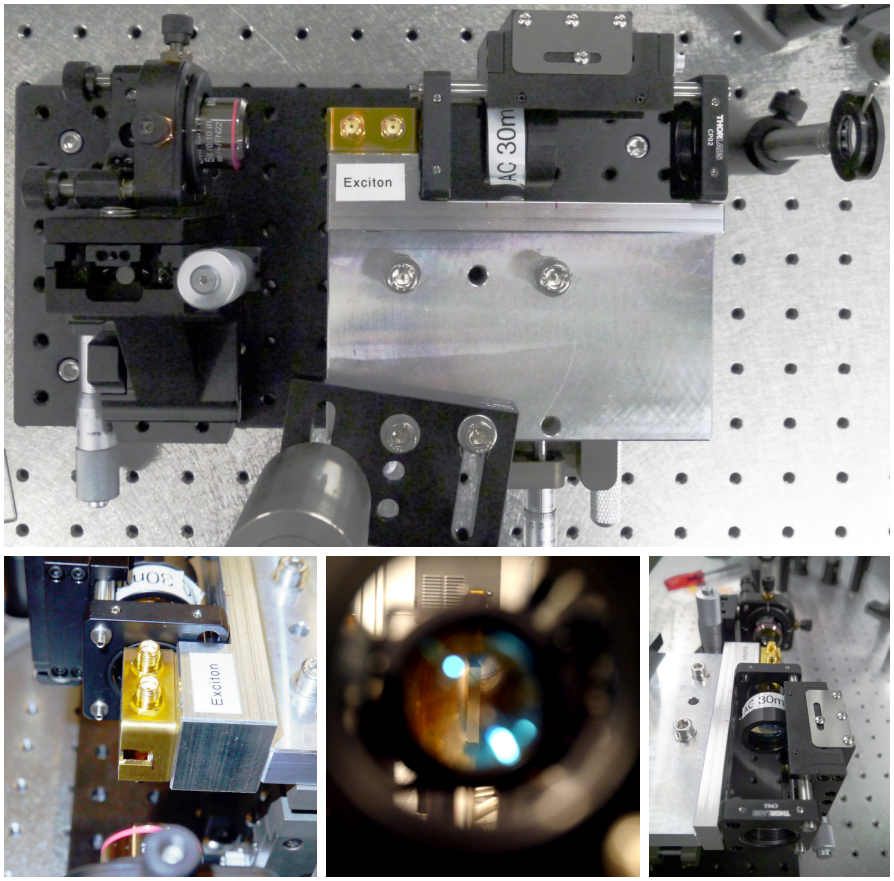

Figure 4.1: Pictures of the EOM on its 5 axis stage.

In order to maximize coupling efficiency, the mode field diameter (MFD) of the incoming beam must match that of the waveguide, and the numerical aperture (NA) of the objective lens must be greater than or equal to that of the waveguide. Coupling efficiency is less of a concern for the experiments using the narrow-band laser since a strong output signal can still be observed even if the mode overlap is partially mismatched. When studying the exciton emission from the quantum dot, however, a mismatch in MFD will result in a large reduction in counts, and the characteristics of the coupling optics must be carefully calculated. See section section 5.1 for further discussion.

A camera was placed on the output side of the waveguide to help align the coupling

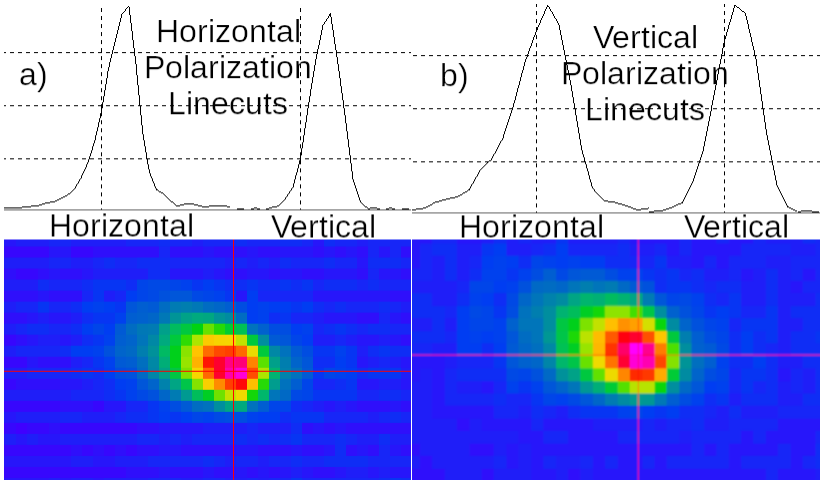

Figure 4.2: The output mode of the waveguide for horizontal and vertical input polarizations.

optics. In addition to making alignment easier, the camera also provided a view of the waveguide's mode. Figure 4.2 shows two focused images, one for each polarization, of the light after passing through the 3 cm collimating lens at the output of the waveguide.

The mode profile has a Gaussian shape, but features some asymmetry in the horizontal direction. In the images, the crystal-air interface is vertical, with air on the left and the crystal on the right. This contributes to the observed asymmetry since the change in index of refraction between the crystal and air is larger than the crystal in and out of the waveguide. Since the waveguide's output is not perfectly aligned with the centre of the 3 cm lens the mode's shape may additionally be skewed. As expected, the vertical cuts for both polarizations are symmetric. The image for the vertical polarization looks larger because of the image's crop factor, but the two polarizations are largely consistent in size and mode profile.

After confirming it was possible to couple light into the waveguide, the next step was to test the electro-optic effect by applying slowly-varying voltages to the electrodes. The next section presents the procedure and results.

4.3 DC Electrode Drive Signals

4.3.1 Experimental Setup

The first milestone for creating a rotating HWP is to determine what voltage is required to induce a relative phase shift of π of one polarization component with respect to the other. The resultant voltage, termed V_π, will then be used to specify the amplitude for the in-quadrature AC drive signals.

As explained in chapter 3, the EOM has three electrodes running along the length of the waveguide. The centre electrode is soldered to the metal case of the EOM, and provides a ground reference. The two outer electrodes have an SMA connector on each end of them, so can be configured with a source on one side and a load on the other, or can be driven in an open circuit configuration. For the DC experiment the open circuit configuration was chosen: the two terminals were tied together and connected to a signal generator. This means minimal current would flow through the device during the experiment. An alternative configuration connecting just one pin for each electrode and allowing the other to float would give an equivalent result.

A schematic showing the DC experiment is given in Figure 4.3. The two electrodes, labeled Channel A and Channel B, are drawn with independent voltage sources, which is necessary for inducing a specific effective waveplate birefringence and angle. For practicality, only two polarization tomography experiments were performed.

The first applies a common voltage to both Channel A and Channel B, $V_B = V_A$, where Channel A is considered the master and Channel B the slave. This is done by using a single voltage source with a T junction to split the signal. The second experiment applies equal and opposite voltages to the two electrodes $V_B = -V_A$. An inverting op-amp circuit was used to create the signals in this differential configuration. In the common case the master voltage was swept through a range of $-7.5\,\mathrm{V} \leq V_A \leq 7.5\,\mathrm{V}$, while in the differential case a range of $-10\,\mathrm{V} \leq V_A \leq 10\,\mathrm{V}$ was used.

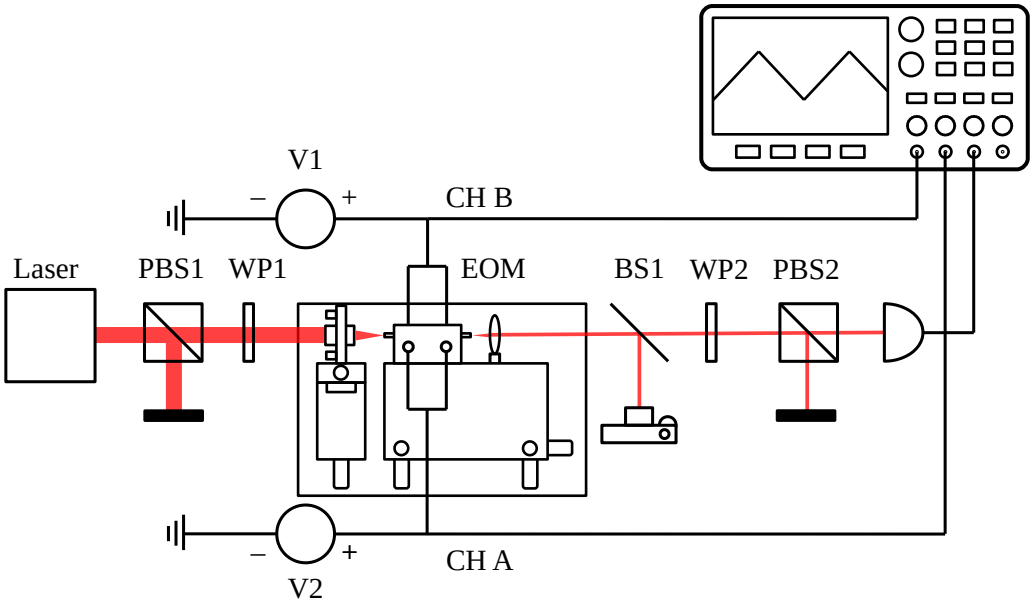

Figure 4.3: The experimental setup for a DC drive voltage.

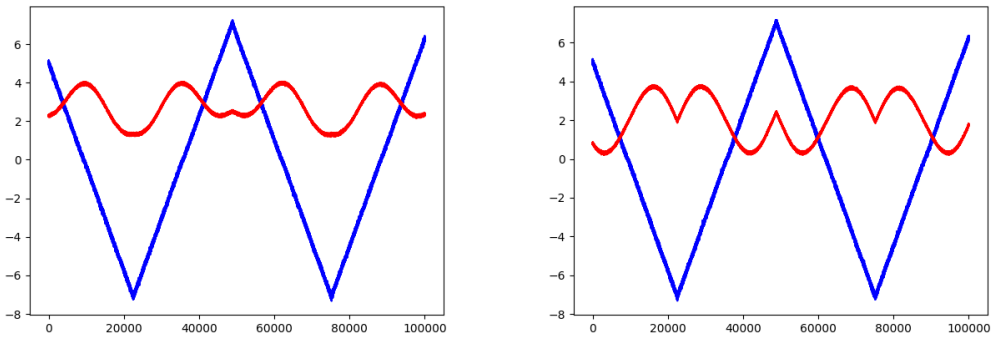

Figure 4.4: Optical intensity (red line) when sending in $|H\rangle$ and measuring $|H\rangle$ (left) or measuring $|L\rangle$ (right) while varying the common voltage (blue line) on the EOM.

4.3.2 Results

A sample graph of a simple result is shown in Figure 4.4. In total 18 different measurements were made, each time sending in one of $\{|H\rangle, |D\rangle, |R\rangle\}$ and measuring from $\{|H\rangle, |V\rangle, |D\rangle, |A\rangle, |R\rangle, |L\rangle\}$. Using the raw data it was possible to reconstruct the state of the output signal for each input and voltage. The graphs in Figure 4.6 show the output polarizations for the device in both the common and differential drive configuration for varying voltages. The top rows show a 3D visualization of how the EOM squeezes the polarization when voltage is varied, while the bottom rows present the data in graphical form for easier analysis.

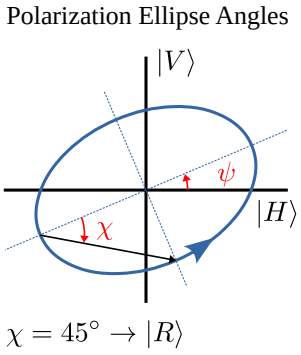

Figure 4.5: The angles ψ and χ define the polarization ellipse for completely polarized light. Positive χ is more right circularly polarized than left, as indicated by the arrow on the ellipse.

In the graphs one can see both the polarization angle ψ and its ellipticity χ. As seen in Figure 4.5, the linear polarizations have $\chi = 0°$, while right circularly polarized light is characterized by $\chi = 45°$ and left circular is $\chi = -45°$. With respect to the linear polarizations, horizontal is $\psi = 0°$, diagonal is $\psi = 45°$, antidiagonal is $\psi = -45°$, and vertical is $\psi = \pm 90°$.

The first observation is that in each measurement the data at zero voltage matches. This makes sense and boosts our confidence in the data since it is the one voltage point that appears on both graphs. In addition, it is seen that only $|H\rangle$ emerges without much change when zero volts is applied whereas $|D\rangle \rightarrow |R\rangle$ and $|R\rangle \rightarrow |A\rangle$. This is very valuable information since immediately it can be seen that the waveguide has some built-in birefringence, and since it takes one basis vector almost exactly to another it is relatively easy to reason about.

In this case, to take $|D\rangle$, a linear polarization, to $|R\rangle$, a circular polarization, the birefringence must contribute a phase delay of around $\frac{\pi}{4}$, equivalent to a quarter waveplate. In addition, the effective quarter waveplate's angle must be 45° with respect to the linear polarization of $|D\rangle$, thus aligned either along the x- or y-axis parallel or perpendicular to $|H\rangle$. This makes sense since $|H\rangle \rightarrow |H\rangle$ at $V = 0$.

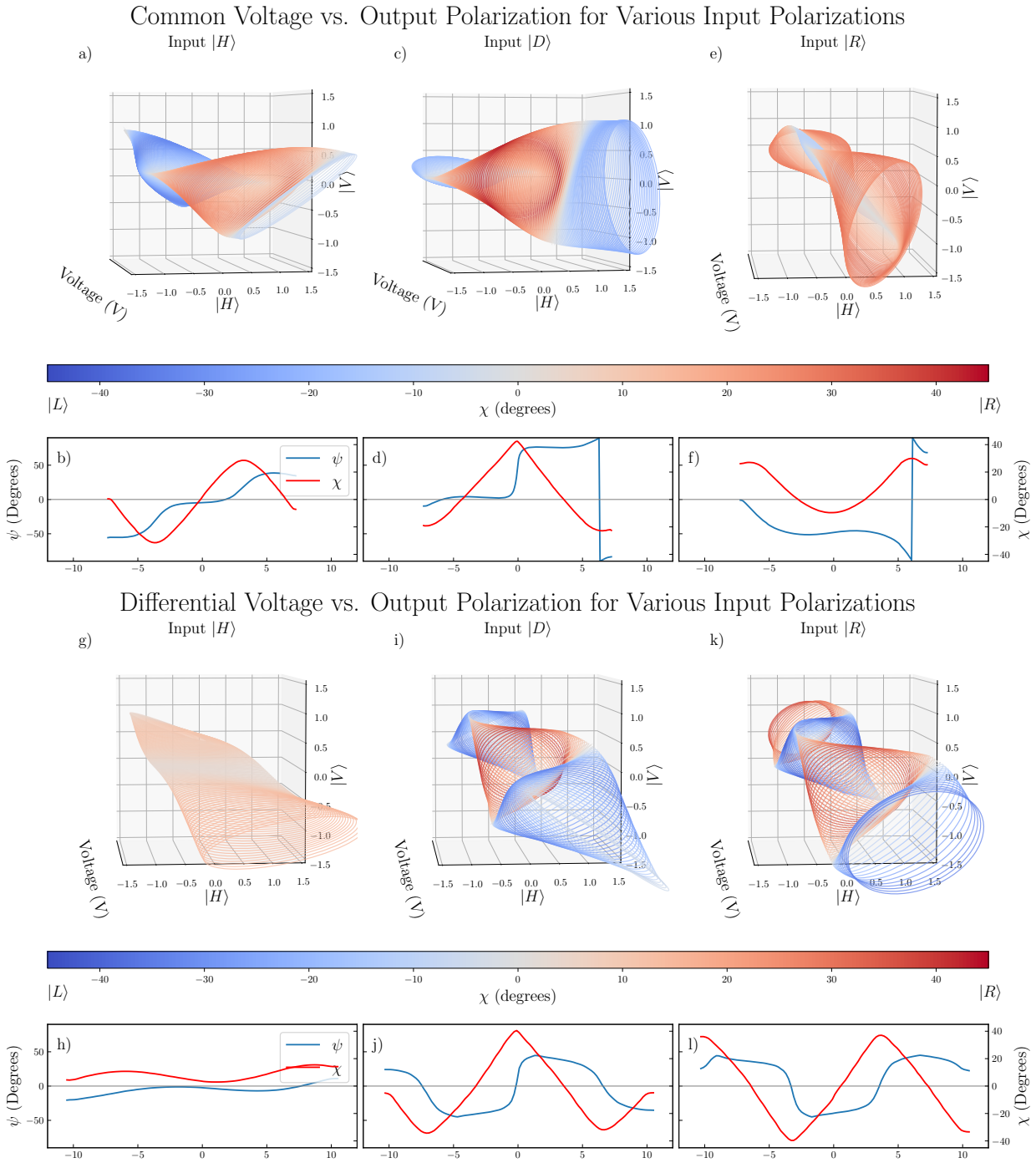

Figure 4.6: Polarization transformation plots for various input polarizations when the DC voltage on the EOM is varied in the common electrode configuration.

By looking at the plot for $|R\rangle$ at zero volts it can be found that the effective quarter waveplate's slow axis is vertical in the lab frame, along y, or in other words parallel to $|V\rangle$. If it were parallel to x instead, the output for the $|R\rangle$ case would be polarized in $|D\rangle$, not $|A\rangle$ as is observed. Note that the orientation of the fast and slow axes is not surprising, given the symmetry of the waveguide and the fact that the crystal is mounted with its longer face dimension along y in the lab frame. It is however surprising that the magnitude of the delay introduced by the birefringence is so close to a $\frac{\pi}{2}$ shift.

The second observation is that the polarization hardly changes angle or ellipticity with a differential voltage applied to the electrodes when $|H\rangle$ is sent in. This means that the axes along which the birefringence is changing in this case must be well aligned along $|H\rangle$. Since the differential voltage creates an electric field in the lab's y direction, it can be determined that this choice of y coincides with the y shown in Figure 3.2 along the crystal's natural principle axes. Thus, the conclusion is that the orientation of the axes of the crystal's xyz-axes coincide with the choice of xyz in the lab frame.

Finally, the graphs in Figure 4.6 can be used to extract the information about V_π. Since it is clear there is a built-in birefringence in the device, the value of V_π can only be found, using the collected data, along the direction of said birefringence. This is because applying an electric field along that same axis can cancel the built-in birefringence almost exactly. This roughly happens where $|D\rangle \to |D\rangle$ and $|R\rangle \to |R\rangle$. Reading directly from the plots, the differential voltage at which this occurs is $V_{A0} = 3\,\mathrm{V}$. Equivalently, the voltage that leads to a π phase delay is $V_{A\pi} = -3V$, at which point $|D\rangle \to |A\rangle$ and $|R\rangle \to |L\rangle$ while $|H\rangle$ is largely unchanged.

The voltage necessary for a half-wave phase delay with the electric field applied in the y direction is therefore the total voltage it takes to go from zero phase delay to a π delay, thus $V_\pi = V_{A0} - V_{A\pi} = 6V$.

From the electrode configuration of the device it is a reasonable assumption that a similar or lower voltage would be required along x for the same effect, but this information is not readily available from the data as collected. The way to determine this is to again run the tomography measurement with voltage sweeps but with an additional fixed voltage offset of $V_A = 3\,\mathrm{V}$ and $V_B = -3\,\mathrm{V}$ to cancel the built-in birefringence.

With the target drive voltage $V_\pi = 6\,\mathrm{V}$ in hand, the experiment can be reconfigured to test whether a laser can indeed be shifted in frequency as predicted by the theory. This is the topic of the following section.

4.4 AC Electrode Drive Signals

As presented in chapter 3, $LiNbO_3$ can be used to create a rotating half-wave plate which in turn acts as a frequency shifter on circularly polarized light. This section aims to provide a demonstration of exactly this phenomenon using light from a narrow-band laser. The experimental configuration is presented in subsection 4.4.1 along with a short discussion of the challenges encountered. Section 4.4.2 then shows two sets of collected results and provides a commentary about them.

4.4.1 Experimental Setup

The experimental setup for frequency shifting a laser is very similar to that used for the DC case in section 4.3. In this case the only polarizations required are circular, either right or left, both for sending into the EOM as well as for observing at the output. As such, a PBS and QWP1 are placed before the EOM, with QWP1 set with its slow axis at 45° with respect to $\hat{x}$. This configuration produces right-hand circular light as defined in subsection 3.3.1. Alternatively QWP1 can be turned around to instead have its slow axis at 135° with respect to $\hat{x}$, which produces left-hand circular light.

A camera is again placed at the output of the EOM to help maintain light coupling into the waveguide. After the camera, the beam is sent either directly to a scanning FP interferometer, or to the FP after a QWP2 and a PBS. With the PBS and QWP2 in place only the circular components of the beam will be allowed to pass depending on how QWP2 is set. When it has its slow axis at 45° it will take $|R\rangle \rightarrow |V\rangle$ which will then be reflected by the PBS. This configuration thus measures $|L\rangle$, the remaining component. In contrast, setting the angle of QWP2 to 135° measures $|R\rangle$.

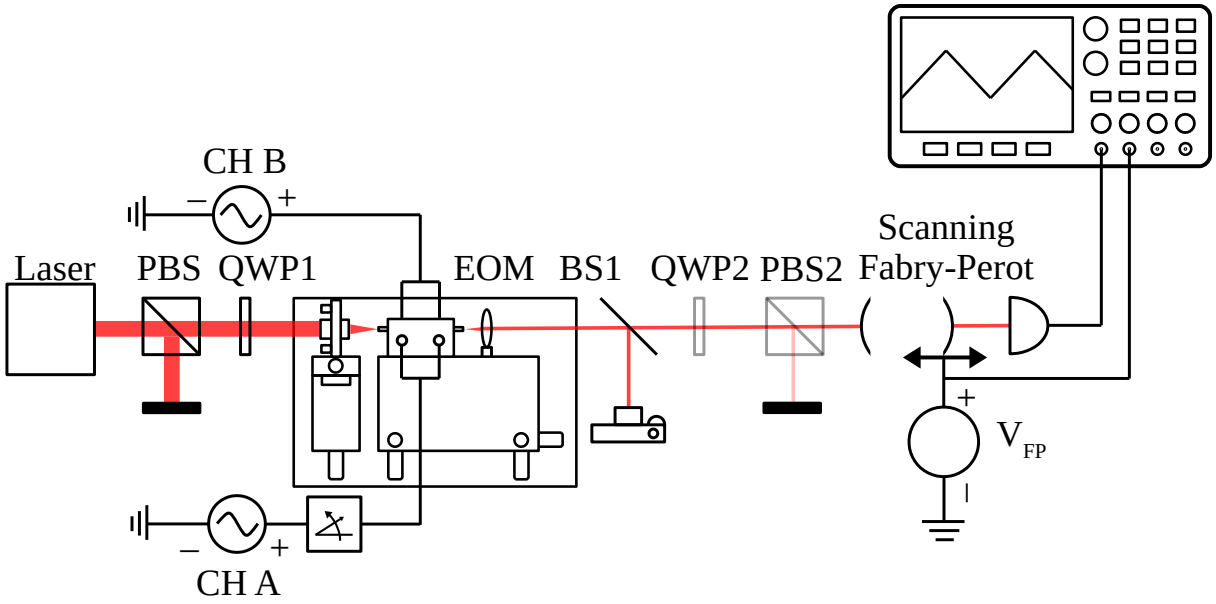

Figure 4.7: Experimental schematic for frequency shifting the narrow-band laser.

The scanning FP interferometer is used to investigate the spectral composition of a beam of light. It generates interference inside the cavity, allowing, in the ideal case, only light with an integer multiple of half wavelengths to positively interfere and thus be transmitted. Assuming the cavity length is such that a particular beam of monochromatic light is transmitted, the cavity can be expanded by exactly a half wavelength for the same beam to be transmitted once again. This distance is called the FSR, and is specified by the FP manufacturer.

In practice, since the cavity has a confocal design, the actual distance between supported modes is a quarter wavelength and it is this confocal-FSR that is quoted. For practical purposes this does not change the analysis, as eliminating the transmission peaks from the additional confocal modes requires extremely precise mode matching to the cavity and is unlikely to happen.

Two FP cavities are available for use in the experiment, one with a (confocal) FSR of 1.5 GHz and the other with 10 GHz. The 1.5 GHz FP gives much nicer resolution for

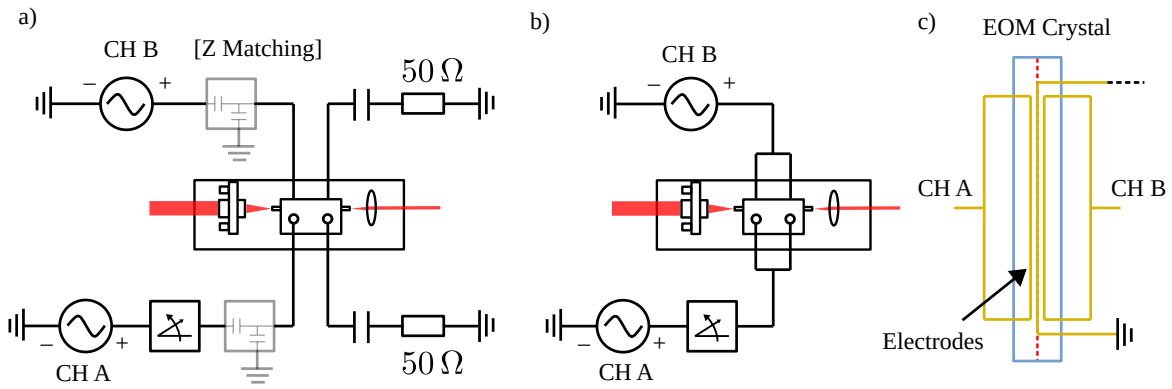

Figure 4.8: Electronic configuration attempts for create the rotating half-wave plate. a) Co-propagating wave configuration with the electrical drive on one end of the electrode and an isolated 50 Ω terminator on the other. An impedance matching circuit is shown in pale and can be included or removed. b) Electrodes tied together and driven from both terminals in unison. c) Close-up schematic of the $LiNbO_3$ crystal with the three electrodes patterned on it. The centre electrode overlaps the waveguide and is the ground reference. In this case the inputs and outputs of each electrode are connected together, the same as in b).

narrow peaks like the laser in this experiment, so it was chosen for collecting the initial dataset.

The analysis in chapter 3 made clear that the two electrodes must be driven in quadrature, with the sinusoidal signal on one advanced or delayed by 90° with respect to the other. The ideal configuration is thus as shown in Figure 4.8a, with the channel inputs connected to two signal generators, each equipped with a DC offset in order to compensate for the built-in waveguide birefringence of the EOM. Channel B additionally has a variable phase delay which can be used to adjust it relative to Channel A. The electrode outputs are then passed through a DC block and a 50 Ω load to ground. The purpose of the block is to prevent the constant flow of direct current through the electrodes on the EOM when a DC offset is used.

The electronic components used in the final experimental setup are shown in Figure 4.9.

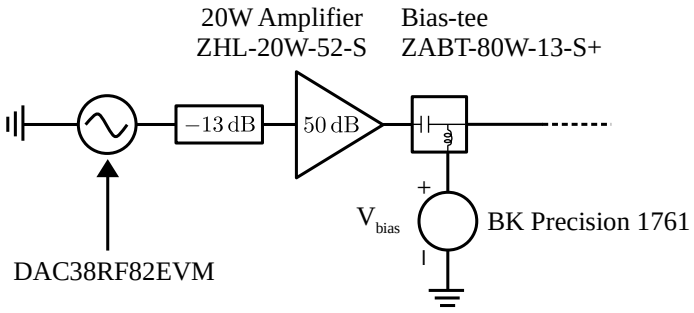

Figure 4.9: The components used for generating the RF signal on the waveguide. From left to right the components are a Texas Instruments Digital to Analog Converter Evaluation Module, an interchangeable attenuator, a 20 W high power amplifier, and finally a bias-tee with a DC voltage source.

As illustrated, a 20 W (43 dBm) 50 dB amplifier boosts the signal from the digital-to-analog converter (DAC) after some attenuation, required to avoid over-driving the amplifier. Since the DAC can output at most 1.733 dBm, a −10 dB attenuator followed by a 50 dB amplification leads to an output power of less than 42 dBm, which is within the rated 43 dBm. A −13 dB attenuator is shown in the diagram, though it is interchangeable and is considered one of the parameters of the experiment. The DAC can produce arbitrary signals with frequency components up to 2.66 GHz, and was configured as a sine wave generator using the PyDualDDS code written by Andreas Fognini [76].

With that said, the initial experiments presented in this section make use of a less-powerful 2 W (33 dBm) 29 dB Mini-Circuits ZHL-1-2W+ which can be driven directly from the DAC.

In a perfect world all of the components in the circuit would be rated for 50 Ω minimizing standing waves and promoting optimal power transfer. The EOM was supposed to also have been designed for 50 Ω, however in configuring the electronics it was found that a lot of power was being reflected from the EOM's input port. Nonetheless, the full experiment was run by sending circularly polarized light into the waveguide, driving the electrodes in quadrature, and analyzing the whole signal at the output with the scanning FP. It was observed that roughly 10% of the laser's power was shifted into a sideband, and the

sideband was either higher or lower in energy depending on whether right- or left-circularly polarized light was used, consistent with the theory.

An RF spectrum analyzer was acquired and used to verify the impedance of the EOM. The discovery was that ports A and B had slightly different impedances, and neither was near the expected $50\,\Omega$. The measured values at 400 MHz were instead $Z_A = 18.5 + j18.0\,\Omega$ and $Z_B = 22.3 + j28.5\,\Omega$. Thus, the standing wave ratios for electrodes A and B are $\mathrm{VSWR}_A = 3.1$ and $\mathrm{VSWR}_B = 3.09$ and the reflection coefficients are $\Gamma_A = 0.5122$ and $\Gamma_B = 0.5114$ respectively. Thus, at the boundary, 51% of the voltage magnitude was being reflected back to the source – quite a lot. In addition, it was theorized that the voltage that was entering the device dropped along the length of the electrode due to its resistance.

Based on this hypothesis, the EOM was connected such that the electrode input and output were driven by the same signal, as shown in Figure 4.8b and c. The theory is that since the electrodes are essentially open circuits the device should then not consume any real power but there should nonetheless be large voltage fluctuations on the electrodes. This in turn leads to a large electric field in the waveguide region as required. It should then be possible to place a voltage antinode at the interface by adjusting the length of the transmission line connected to the device or alternatively changing the driving frequency.

Using the configuration as in Figure 4.8b an increase the optical power conversion was observed, up to 50% at maximum amplification with the 2 W amplifier. Note that this approach can only be used for sub-gigahertz driving frequencies before the electric field begins to vary appreciably as the optical field travels through the device. Operation above gigahertz is still viable, but requires co-propagating electric and optical waves. Recommended reading for this scenario is ref. [77] chapter 9.

Despite the new electrical configuration it was apparent that insufficient electric field was being created in the waveguide region. An impedance matching circuit was created for the EOM in order to bring its impedance closer to $50\,\Omega$ therefore reducing reflections. Smith charts are shown in Figure 4.10 with the impedance matching circuits attached to both channel A and channel B, as shown in Figure 4.8a. By using the circuit it was possible to bring the device very close to $50\,\Omega$ matched with $Z_A = 52.8 - j3.7\,\Omega$ and $Z_B = 51.0 + j7.3\,\Omega$. This change created an increase in converted light once again, with

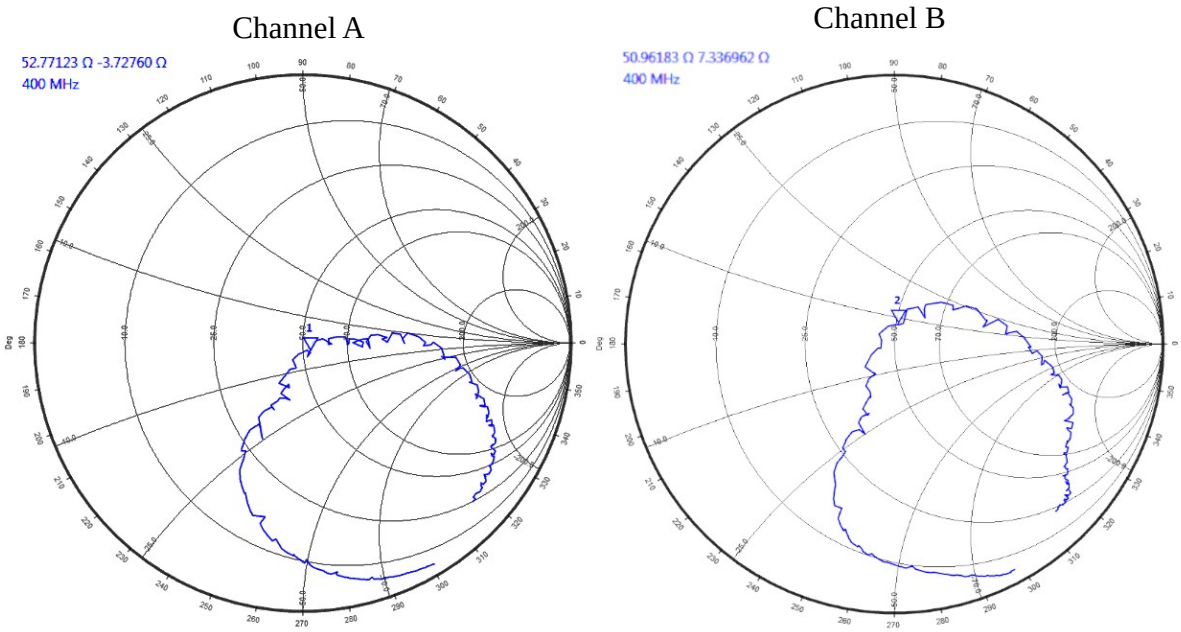

Figure 4.10: Impedance of the EOM with an impedance matching circuit for both channel A and channel B. The desired drive frequency is 400 MHz, which was chosen as the centre of the sweep which ranges from 300 MHz through 500 MHz.

up to 75% of the optical power in the desired sideband.

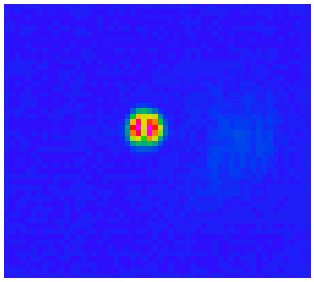

Figure 4.11: Multimode beam after overheating the electrodes by impedance matching.

Unfortunately, this experiment also caused the device to become extremely hot. Temperatures at the surface of the crystal were in excess of 110 °C, as measured by an infrared thermometer. Following this experiment the conversion efficiency dropped significantly and it was eventually determined that the waveguide on the chip now supported multiple optical modes, as seen in Figure 4.11.

The source of the problem was determined to be the thickness of the gold electrodes on the crystal surface. While initially thought to be 10 µm, it was established that only 1 µm had been deposited which caused Joule heating at the drive voltages required for complete frequency shifting with the co-propagating wave configuration. The excess heat caused the waveguide dopant to diffuse further into the crystal, leading to multimode operation

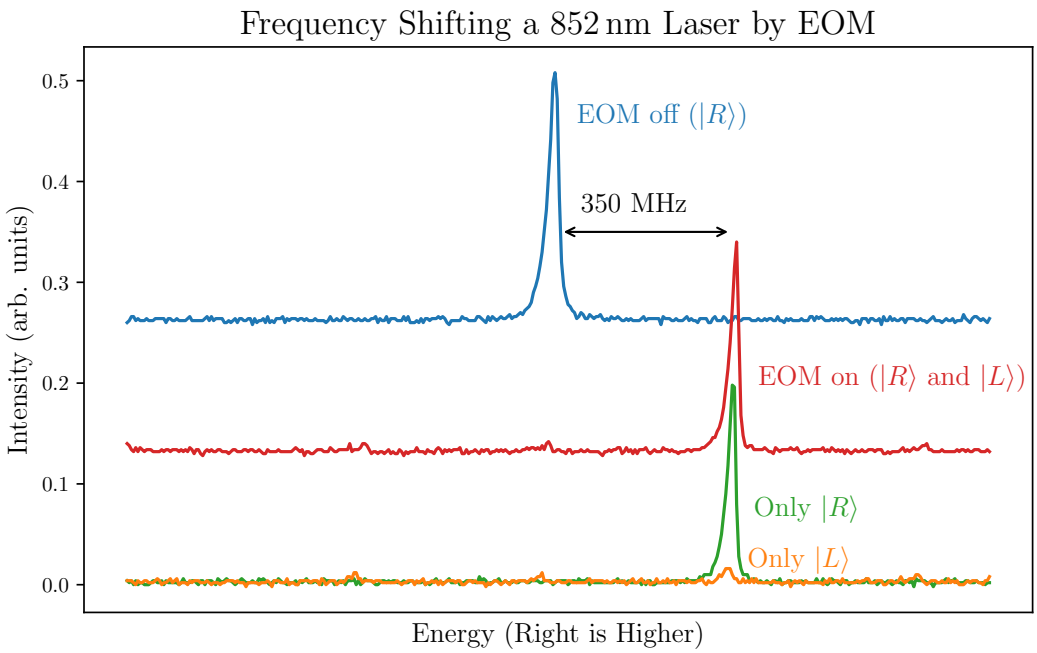

Figure 4.12: Shifting the laser line to the right by 350 MHz. This data is collected using a Fabry-Perot cavity with a 1.5 GHz free spectral range, meaning the peak separation is very clearly visible.

and decreased performance.

Since the device didn't accumulate heat when driven with the electrodes tied together as in Figure 4.8b, this configuration was used along with larger amplifiers to reach the necessary V_π electrode voltage in spite of the significant electrical reflection.

4.4.2 Results

With the more powerful 20 W amplifiers in place the full experiment was run again. The DC offsets on channel A and channel B were precisely tuned and the curve in Figure 4.12 obtained. The parameters for the experiment were 0.257 $\mathrm{mV_{RMS}}$ (1.209 dBm, 0.95 in the

code) input at 350 MHz, a 36 dB amplification, channel A and channel B DC offset of $V_{\mathrm{A,DC}} = -13.19\,\mathrm{V}$ and $V_{\mathrm{B,DC}} = 15.73\,\mathrm{V}$, and a phase offset between channel A and B of 350°. The frequency was chosen to be 350 MHz by trial and error, optimizing for conversion efficiency.

The blue curve is the signal from the 1.5 GHz FP with no electro-optic modulation or polarization filtering. Conversely, the red line shows the effect with the EOM running. Almost all of the power is shifted to a higher energy, although a small peak is visible at the centre as well as on the side opposite. Using the value specified for FSR and the next neighboring peak as a reference (not shown), it was verified that the frequency shift is 352(4) MHz, in excellent agreement with the expected frequency shift of 350 MHz. Each point in the dataset represents a 4 MHz wide frequency bin.

The area in the higher-energy sideband was calculated to be 92.6% [63], a very good conversion efficiency. Adding the QWP and PBS helped resolve the polarization components in the sideband, showing that the light is still predominantly circularly polarized. The expected findings did not match what is observed, though, as the polarization in the shifted beam remained right-hand circular, whereas left-hand circular was expected. It is hypothesized that this observation results from the very high DC offsets applied to each channel – each is well above what was determined to offset any waveguide birefringence in subsection 4.3.2. In addition, the phase difference between the channels is far from an in-quadrature drive.

The experiment was run a second time with different parameters in order to identify whether the polarization handedness could be made to match expectations, and to demonstrate that conversion is possible into the lower-energy sideband. This time the lower resolution 10 GHz FP cavity was used. The findings are shown in Figure 4.13, which incorporates a sweep through the full cavity FSR.

The parameters for the experiment better matched what is expected for the creation of a rotating half-wave plate. The input voltage amplitude from the source is $0.254\,\mathrm{mV_{RMS}}$ (1.107 dBm, 0.93 in the code) while the amplification is set at 37 dB using 13 dB of attenuation before the amplifier. A 105° phase was chosen between channel A and channel B. The DC offsets were adjusted to $V_{\mathrm{A,DC}} = -4.79\,\mathrm{V}$ and $V_{\mathrm{B,DC}} = 10.22\,\mathrm{V}$. Again, right-circularly

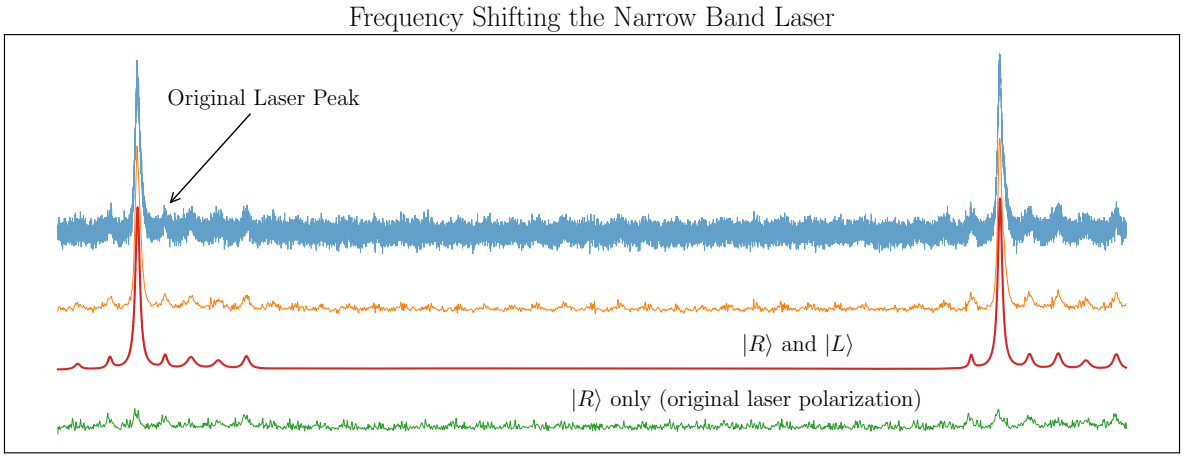

Figure 4.13: Shifting the laser line lower in energy (to the left) by 325 MHz. A scan of the full FSR of the FP cavity is pictured, allowing the magnitude of frequency shifting to be determined. The figure shows the original data with no polarization filtering (blue), the same curve after denoising (orange) and a fit using a combination of Lorentzians (red). In addition, the green line shows the right circularly polarized component of the other curves. The original laser center is the fourth peak from the right side in each peak group, indicated. As measured, the shifted peak is 319.4(7) MHz lower in energy than the original center as extracted from the left peak grouping.

polarized light was used at the EOM's input.

Much more noise is observable in the data set from Figure 4.13 than was seen in Figure 4.12. The reason for this is a change in the detection system. In short, an amplified photodiode was used and the signal was captured in free space. This change was compounded by a lower input laser intensity for the experiment. Details on the free-space measurement scheme are described further in chapter 5.

The graphic shows four curves, vertically offset from one another. The top three curves represent the same data, at various stages of processing. The raw signal is shown on top in blue. It was interpolated using a polynomial spline in order to denoise the data, which is shown just below in orange. From the denoised data it was possible to extract a fitted curve using a series of Lorentzian peaks, shown in red.

The data for the top three curves was collected while the EOM was running and without any polarization filtering in place on the output side. Contrary to the data collected in Figure 4.12, this time the optical power was transferred to a lower energy sideband, showing that the EOM can both up- and down-convert light.

Another difference between the two results is that when the right-circular polarized component of the output signal is isolated, shown in the bottom-most curve in green, it contains very little optical power: the majority of the power is left-circular. This matches with the expectations from the theory in chapter 3. For this reason, these results are considered an upgrade with respect to those collected in Figure 4.12.

Obviously, though, the EOM's parameters were not as optimized this time since it is apparent that a lot of optical power is shifted into the other harmonics. It is believed that further tuning of the parameters can fully resolve this.

Since it has now been proven that the EOM can be used to frequency shift light, chapter 5 goes on to explore the effect when the same technique is applied to individual photons.

Chapter 5

Converting Individual Photons

The central objective of this thesis is to demonstrate experimental evidence that a rotating half-wave plate can tune the energy of a photon. This chapter brings together the building blocks from each of the previous chapters to show that it is indeed possible, and discusses the associated successes and challenges.

The first step toward frequency shifting individual photons is to maximize the number of photons that travel through the EOM. Section 5.1 focuses on this aspect of the experiment and discusses the design of the coupling optics and shows a calculation of coupling efficiency. The next milestone is to measure the fine structure splitting of the QD's exciton, which is presented in section 5.2. Finally, with a target in mind, the QD's single photon emission is shifted by the same technique demonstrated in chapter 4.

5.1 Photon Coupling

5.1.1 Designing for Optimal Coupling

In section 4.2 the topic of coupling light into the EOM's waveguide was discussed, however the abundance of optical power from the laser made real coupling optimization unnecessary. Given that the current objective is to experiment with the quantum dot's single photon

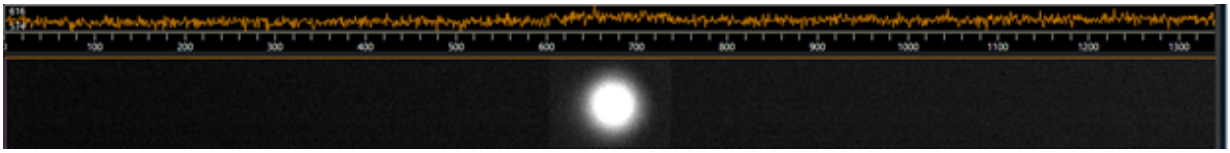

Figure 5.1: An image of the quantum dot's emission profile taken by the CCD camera in a spectrometer. The input slit was fully opened. Performing a Gaussian fit reveals that the e^{-2} mode field diameter is 1.48 mm.

emission, more care must be taken to ensure that the largest number of photons possible make it through the EOM. Optimizing the counts like this directly reduces the measurement time needed for any given experiment involving single photons and the EOM.

Importantly, one can choose the coupling optics to specifically make sure the modes of the waveguide and the exciton's beam are ideally matched. To do so, it is important to know what the exciton's beam size is and what the mode field of the waveguide looks like along with its MFD. Since the waveguide is single mode for our operating wavelength around 892 nm, the ideal mode field matching can be done given the waveguide's NA. With this knowledge, it is possible to proceed with designing the optical configuration at the input of the waveguide.

The exciton's beam size can be measured by sending a collimated beam from the QD into a spectrometer with a charge coupled device (CCD) camera installed. If the spectrometer's input slit is opened wide enough that the full beam can propagate through, one can determine the mode field diameter by capturing the profile of the spot as seen on the CCD. For a spot with a Gaussian intensity profile, one can then measure the mode field radius as the distance between the beam's centre and a point $\frac{1}{e^2}$ times the mode's intensity at the centre point. The MFD is then twice this radius. For our QD, the exciton's mode field diameter as just defined is 1.48 mm, and a picture captured by the CCD camera is shown in Figure 5.1.

Next, the NA of the waveguide must be determined. This data is provided by the device manufacturer, and has been taken as the average over four test samples with 7 µm waveguides identical to that in the EOM. Based on their measurements, it was found that the mode field is elliptical with an ellipticity of 1.5, and the corresponding MFD is

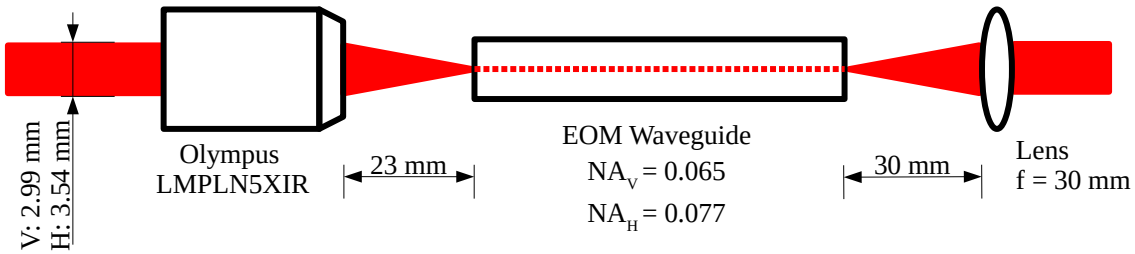

Figure 5.2: Coupling light in and out of the EOM's's waveguide.

11.7 µm along the vertical direction in our lab frame, and 7.7 µm along the horizontal direction. This corresponds to vertical and horizontal values for NA of $\mathrm{NA}_V = 0.065$ and $\mathrm{NA}_H = 0.077$ respectively. As discussed in section 4.2, the mode profile is the same for both $|H\rangle$ and $|V\rangle$ polarizations, not to be confused with H and V as used to describe the horizontal and vertical extents of the waveguide's NA. Surrounding context should make the meaning of H and V clear throughout this text.

It is now possible to choose a microscope objective lens for the input coupling to the EOM. It must have high transmittance for near-infrared light, a relatively long focal length, or working distance (WD), to ease alignment and focus adjustments, and an NA greater than $\mathrm{NA}_H = 0.077$, the larger of the two NAs. The right lens is an Olympus LMPLN5XIR, which has an NA of 0.1, a 23 mm WD, and around 93% transmittance at 892 nm.

The coupling optics for the waveguide are pictured in Figure 5.2. In particular, the objective lens on the input side is shown, as is the 30 mm collimating lens at the waveguide's output. The horizontal and vertical $\frac{1}{e^2}$ mode field diameters before entering the objective lens are shown, which were back calculated from the waveguide's NA values using the formula $\mathrm{MFD} = 2 \times \mathrm{NA} \times f$. The results are $\mathrm{MFD}_H = 2 \times 0.077 \times 23\ \mathrm{mm} = 3.54\ \mathrm{mm}$ and $\mathrm{MFD}_V = 2 \times 0.065 \times 23\ \mathrm{mm} = 2.99\ \mathrm{mm}$.

Now that a target input beam size has been found, the exciton's original beam size must be expanded to create an ideal matching. In the process, though, the emission from the QD must be passed through a transmission grating in order to spatially separate the exciton from the biexciton. The grating in question (LightSmyth T-1500-875) has 1500

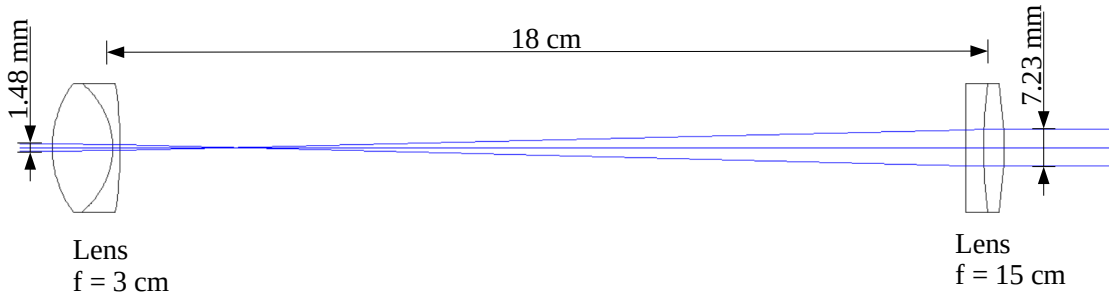

Figure 5.3: An OSLO simulation showing the 5x beam expanding telescope. Passing the quantum dot's emission through these lenses changes the beam size from 1.48 mm to 7.23 mm.

grooves per millimeter, is designed for near-infrared light at 875(20) nm, and, critically, has an equal efficiency for all polarizations. Before passing through the grating, the beam from the QD is expanded by 5× with a telescope consisting of two lenses: a 3 cm lens at the input and a 15 cm lens at the output. The telescope expands the original 1.48 mm beam to 7.23 mm, as pictured in Figure 5.3.

The purpose of the transmission grating is to create different paths for the exciton and biexciton. Only the exciton's path is used for the single photon frequency shifting experiment, but both paths will be required when implementing the full universal fine-structure eraser for perfect entanglement. Even though the biexcitons will be discarded in this experiment, the transmission grating is a key component of the optical setup since it prevents the other optical frequencies emitted from the QD, nanowire, and substrate from coupling into the EOMs waveguide: they will no longer be properly mode matched.

Since the two beams propagate with a very slight angle between them after the grating, they must travel a relatively long distance before becoming ideally separated. Passing them each through the same 1 m lens will allow the beams enough space to diverge, while also focusing them in unison so they can be cleanly sent in opposite directions. The actual separation is done using a knife-edge right-angle prism mirror (Thorlabs MRAK25-E03) set at the focal point of the 1 m lens. Figure 5.4 shows the components used to separate the exciton and biexciton.

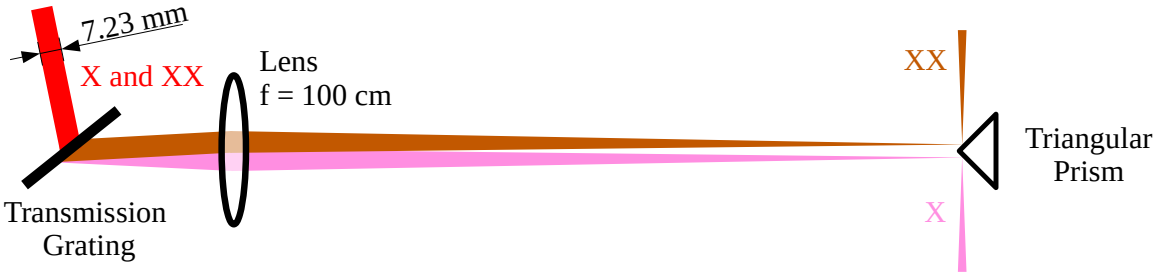

Figure 5.4: Separating the exciton (X) and biexciton (XX) with a transmission grating, one metre lens, and a triangular prism.

Now the final design step can be resolved: set the beam size after the knife-edge prism to the 2.99 mm or 3.54 mm required for optimal coupling to the EOM. Simulations with OSLO determine the right choice is to place a 40 cm lens one focal length away from the knife-edge prism. This creates a beam size of 2.85 mm, which is close to the required vertical beam size of 2.99 mm. A set of cylindrical lenses can then be used to create the elliptical beam shape, expanding the horizontal MFD to 3.36 mm; again, this is close to the 3.54 mm target beam diameter. Figure 5.5 shows the two lenses and beam shaper in action.

5.1.2 Testing Coupling Efficiency

With the optical components determined, testing the setup required three actions. The first is to excite the quantum dot and measure the number of exciton counts per second when sent directly to a spectrometer. This measured number will be the benchmark for counts received through the EOM's waveguide. Once the benchmark is done, the exciton counts are again optimized on the path passing through the waveguide. Finally, the losses for each component in the system are determined from theoretical values and used to compute the total loss for the EOM.

The main challenge in measuring the frequency shift of single photons is to acquire a

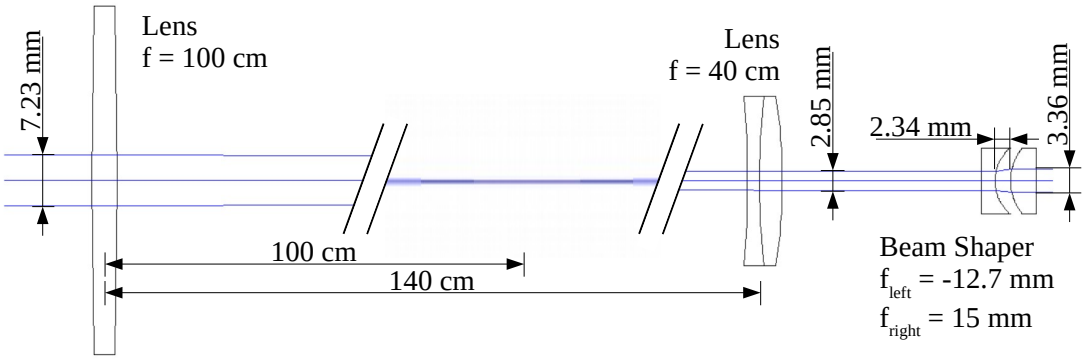

Figure 5.5: A 40 cm lens sets the beam size to 2.85 mm after it has been focused and split by the knife-edge prism. Two cylindrical lenses then shape the mode field to match the ellipticity of the EOM's waveguide.

strong signal once they are sent through a FP interferometer. Since the interferometer passes only a fraction of the photons' linewidth at any instant, the most important criteria for the quantum dot's emission is total counts per second.

A selection of excitation schemes have been studied for quantum dots [59], including above bandgap excitation at 830 nm, quasi-resonant at 870 nm, and resonant excitation near 893 nm. The highest counts are achieved using the above-band scheme, with an 830 nm continuous wave laser. Optimizing the exciton counts on a spectrometer just after passing through the 5x telescope results in the spectrum initially presented in Figure 2.13, reproduced in Figure 5.6 for convenience. The high rate of exciton detection events per second is evident on this graph, shown for the "X" line as 625100 cps at the peak. A total count rate of 1440960 cps is calculated by integrating the exciton line.

Of greater interest, though, is the spectrum after the beam is coupled through the waveguide on the EOM's lithium niobate crystal. In particular, the measured number of counts per second should remain high, and all the emission with exception of the exciton should be filtered out. Figure 5.7 presents the spectrum collected directly after the collimating lens at the output of the waveguide. Notably, the exciton counts are very high with

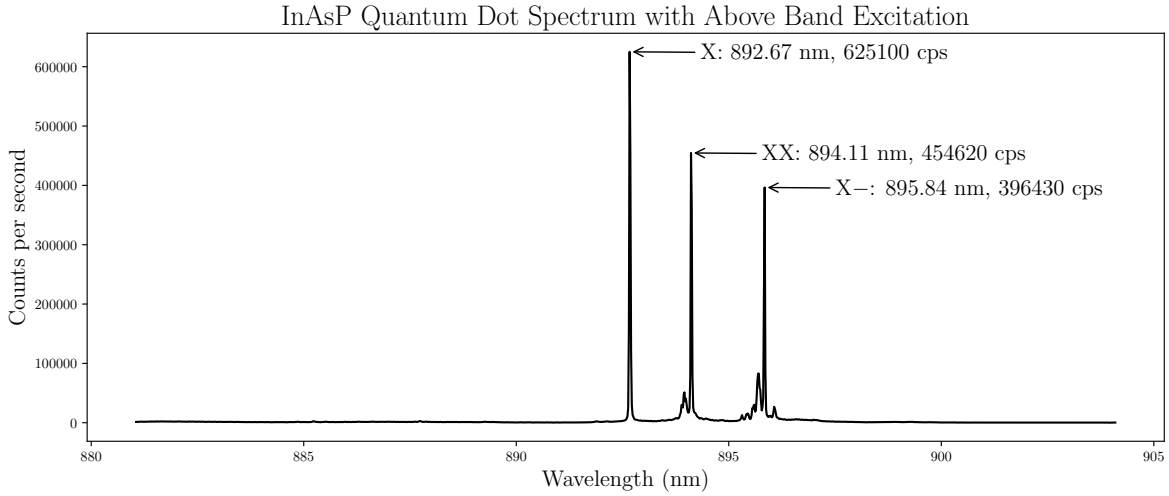

Figure 5.6: Spectrum collected from the quantum dot using above band excitation at 830 nm. The exciton line is labeled "X" and is measured with a peak at 625 thousand times per second on the CCD camera. When integrated, which represents the total counts per second for the exciton line, 1440960 counts per second are observed.

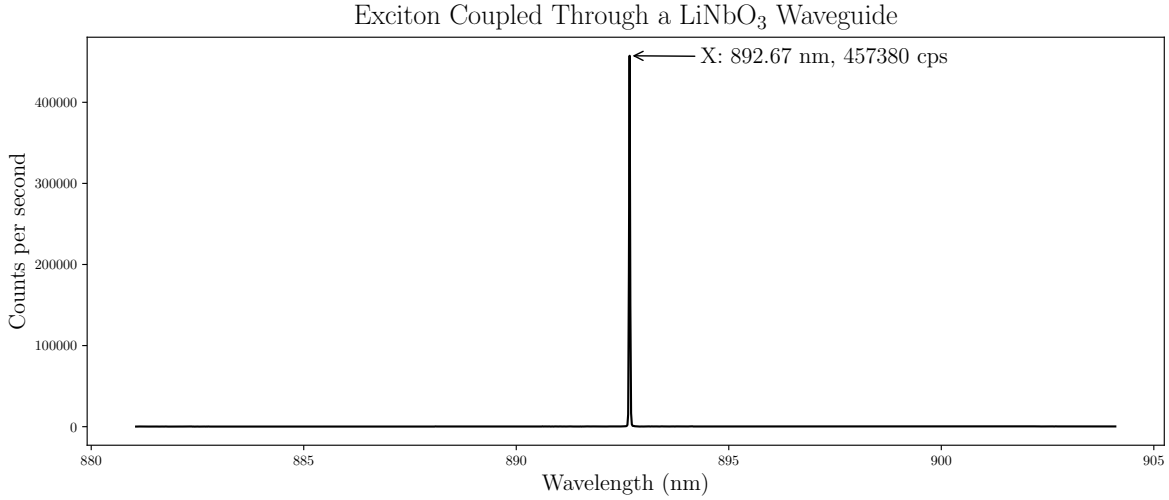

Figure 5.7: A sharp line showing that the exciton is the only spectral portion of the quantum dot's signal that passes through the EOM's waveguide. Its peak is at 457 thousand counts per second, observed on the spectrometer's CCD camera. The integrated area of the exciton line gives 836940 counts per second.

457380 detection events per second at the peak and an integrated count rate of 836940. In addition, the exciton line appears as the only feature in the spectrum, which is a desirable property.

When considering optical losses, it is worth noting that the data collected in Figure 5.7 also required that the exciton pass through the transmission grating, the additional 1 m and 40 cm lenses, and the microscope objective, in addition to the EOM. In contrast, these optical elements were bypassed for the data shown in Figure 5.6. Note that the cylindrical lens beam shaper was not used, and is left as a future refinement to further optimize the number of detection events on the EOM's path.

Table 5.1 presents each of the optical components in the setup along with their theoretical efficiencies. There are two paths of importance: one directly from the cryostat housing the quantum dot to the spectrometer and the second from the cryostat, through the EOM and its associated optics, and then to the spectrometer. The optics from the cryostat are common to both paths, and the calculated CPS along this common path is shown above the first centred horizontal line in the table. The rows below the line have their columns split into either the direct path or the path through the EOM, appropriately.

The exciton counts per second at the spectrometer are known for both of the paths in question from their measurement using the spectrometer's CCD. Those numbers are entered in the last row of Table 5.1. The count rate measured in the direct path is used to calculate most of the other rates in the table, including the common path from the cryostat. The count rate at the input to the EOM is also calculated using the counts measured on the direct path by propagating the calculated count rate from the first location common along both paths through to the EOM using the theoretical efficiencies.

The result is 1091851 counts per second at the EOM's input and 938769 counts per second at the output, for a calculated optical efficiency of 86%. This figure includes both the losses from coupling as well as optical losses from propagation through the lithium niobate crystal, and is sufficiently high to allow good data collection, as will be shown in section 5.2. As such, with a good signal from the quantum dot observable through the EOM, the next step is to configure an FP interferometer in order to analyze the exciton's spectral composition more precisely.

Component	Theoretical Efficiency	Calculated CPS		Note
		Direct	via EOM	
Cryostat aperture		2631526		Both paths are identical to start
70/30 Beam Splitter	0.65	1710492		
Mirrors (2x)	0.9506	1626036		
5× Telescope	0.9865	1604158		
			↑	
Mirrors (2x)	0.9506	1524952	→ 1524952	Counts calculated using direct path
Mirrors (2x)	0.9506	1449658	↓	
Grating	0.95		1448704	
Mirrors (2x)	0.9506		1377175	
100 cm Lens	0.95		1308316	
Prism and Mirror	0.9506		1243718	
40 cm Lens and Mirror (2x)	0.9440		1174033	
Olympus Objective Lens	0.93		1091851	Forward calculation from direct path
Electro-Optic Modulator	0.8600 (calculated)		938769	Back calculation from measurement
3 cm Lens	0.9925		931729	
Mirrors (4x)	0.9037		841992	
		↑	↑	
Spectrometer Input Lens	0.994	1440960	836940	Measured CPS used to back calculate

Table 5.1: Overall efficiency of the EOM is calculated from integrated exciton count rate data in the direct path to the spectrometer as compared with that from the path via the EOM. Measured count rates are taken from the data in Figure 5.6 and Figure 5.7, and appear in the last row of the table. Theoretical component efficiencies are then used to calculate the photon count rates at the input and output of the EOM by following the indicating arrows. The resultant EOM input and output count rates are coloured red in the table, as is the calculated overall 86% optical efficiency of the EOM, found from their ratio.

5.2 Measuring the Exciton Fine Structure

The overarching objective of this thesis is to demonstrate that a rotating half wave plate can be used to correct for the exciton's FSS in a InAsP quantum dot, which will render the quantum entanglement present in every emitted photon pair usable in real applications.

Previous studies have measured the FSS in the particular QD under study to be $\delta = 795.52(35)\,\mathrm{MHz}$ [67]. This section studies another method of measuring the FSS by using an FP cavity and shows that the results obtained largely agree.

The FP was already introduced in subsection 4.4.2, and a similar strategy will be used to collect the data herein. The photodetector built in to the FP is not able to detect photons in the single-photon regime, so the experimental method that follows differs somewhat and is the topic of the following section.

5.2.1 The Fabry-Perot Interferometer

The selection of scanning FP interferometers from Thorlabs is limited to two at our wavelength of interest which primarily differ in their FSR: one has an FSR of 1.5 GHz (Thorlabs SA200-8B) and the other 10 GHz (Thorlabs SA210-8B). The choice should be made based on the linewidth of the signal one desires to measure. A high-finesse cavity with a 1.5 GHz FSR is great for resolving closely spaced peaks with narrow linewidth, such as the narrow-band diode laser used in chapter 4. Studies on other InAsP quantum dots reveal that the exciton's linewidth is on the order of 1 GHz, which is too broad for the 1.5 GHz cavity. Luckily, the 10 GHz option is a good choice for accomodating the exciton's wider line.

Each of the two FPs come with a built-in photodiode which one can connect to an oscilloscope for fast experimentation. Indeed, this is how the curves in subsection 4.4.2 were collected, and works so long as the light source has sufficient intensity. Unfortunately, the QD's exciton line is not intense, so a different detection scheme must be devised. Luckily, the photodiode can be removed from the FP housing, which makes it possible to re-collimate the transmitted photons for detection by an avalanche photodiode (APD). Figure 5.8 shows the 10 GHz FP aligned in the beam's path as it travels toward the spectrometer.

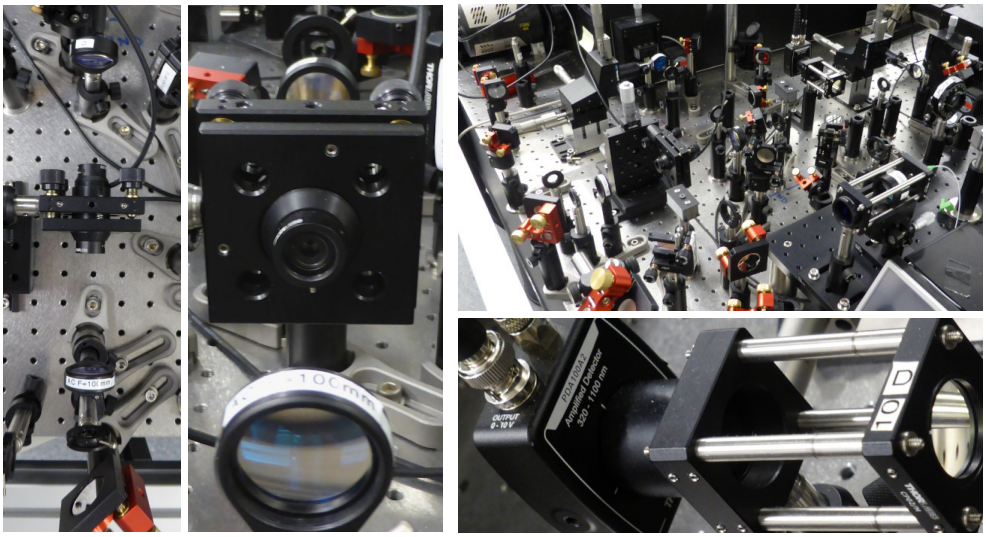

Figure 5.8: Images of the 10 GHz Fabry-Perot interferometer and the two 10 cm lenses used to focus the beam in and out. The FP was aligned directly with the spectrometer (seen in the top right photo, at far right). An amplified photodetector was used to measure the output signal from the FP (bottom right).

Aligning the FP cavity was made relatively easy by using the diode laser from chapter 4 as a guide. First, the laser was coupled into the EOM's waveguide and then sent directly to the spectrometer. This reference path was marked with three irises, visible in Figure 5.8. Two 10 cm lenses are required for focusing the beam into and out of the centre of the FP cavity, and were placed 20 cm apart along the path, with the beam passing straight through the centre of each. They were adjusted until the beam was again aligned through the reference irises. Finally, the FP was placed at the focal point exactly half way between the two lenses.

The FP's built-in photodiode was placed at its output in order to gain crude alignment. The method was to adjust the position of two translation stages and the FP's tip/tilt kinematic mount while scanning the cavity length until a clean peak was observed on the photodiode, as pictured in Figure 5.9a). Once a good position was found, the build-in photodiode was removed and the beam was sent to the spectrometer's CCD camera for fine tuning.

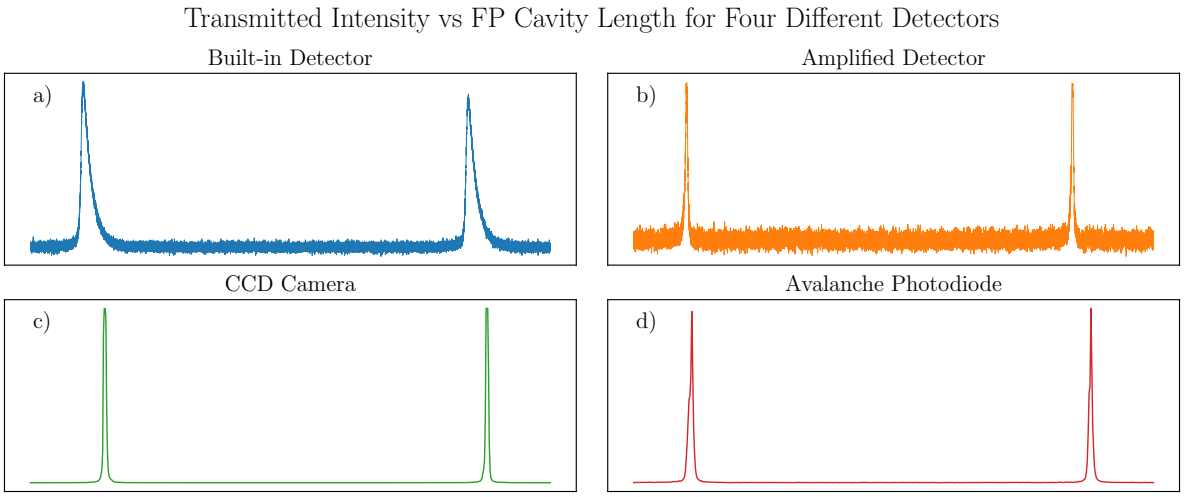

Figure 5.9: Detecting the intensity of light transmitted through the 10 GHz FP on four different photodetectors as cavity length is changed. The light source is the narrow band 852 nm diode laser used in chapter 4. Each plot shows a pair of peaks which correspond to adjacent modes in the confocal FP cavity.

In total, the experimental setup has four different detectors that can be used with the signal transmitted through the FP: the built-in detector, the free-space amplified detector (Thorlabs PDA100A2) pictured at bottom right in Figure 5.8, the spectrometer's CCD camera, and the APD at the spectrometer's second output port. To verify that the experimental setup is consistent, it should be possible to reproduce a similar curve to that seen on the FP's built-in photodetector by using each of the other detectors. The four plots shown in Figure 5.9 qualitatively compare these curves.

It is clear that each of the three additional detectors in Figure 5.9 b), c), and d) produces a curve resembling that of the original built-in detector in a), and immediately some qualitative differences become evident. The first observation is that the line shape in a) has a large tail to the right, whereas the other three do not. The tail is exponential in character and represents the recovery time of the detector once a high output is produced. Each of the amplified detector, CCD camera, and APD are able to reset much more quickly and therefore output narrower peaks with much nicer symmetry.

Also of interest is the large noise character for both detectors in a) and b). Both the CCD and APD are very well isolated from ambient light yet are very sensitive, and are thus able to create a very clean signal. The trade-off, however, is that they do not provide feedback to an experimenter very quickly: the graphs in c) and d) take a few seconds to produce even for a light source of ample intensity like the diode laser. This is the reason for which an amplified photodetector is included in the experiment: it can provide the graph in b) with an update rate of 40 Hz or more. Configuring the EOM's parameters so as to create a rotating half-wave plate requires this instantaneous feedback.

Finally, each of the graphs in b), c), and d) show a similar curve shape. Specifically, it is worth noting that the width of the peaks as compared to the peak spacing is consistent for all three. Since each of the detectors are very responsive, the measured linewidth should be a convolution of the laser's linewidth, specified as 10 MHz, and the FP's resolution, which is 67 MHz. In this case, the FP's resolution will be the dominant contributor to measured linewidth.

With the alignment of the FP complete and the setup's integrity verified, the spectral decomposition of the exciton line can now be studied.

5.2.2 Fine Structure Measurement

The significant building blocks for measuring the exciton's fine structure have at this point been assembled, and in order to collect the appropriate data it suffices to repeat the experiment in subsection 5.2.1 many times over using various polarizations of light from the quantum dot instead of the laser.

Since the polarization of the photons emitted by the two exciton recombination pathways discussed in the section 2.3 are linear and orthogonal, passing the beam from the quantum dot through a polarizing filter performs a projective measurement onto a linear polarization basis rotated by some controllable angle α with respect to the lab frame. Each of the pathways has a slightly different energy which should be possible to observe using the scanning FP interferometer. This is expected because the FP's resolution is 67 MHz, while the FSS as previously measured is an order of magnitude larger at $\sim$800 MHz.

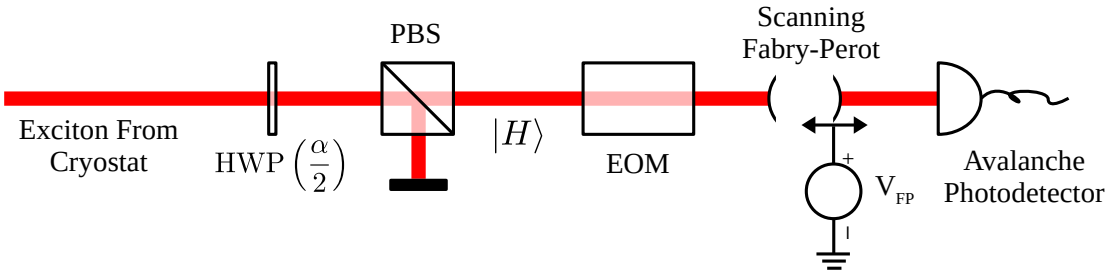

Figure 5.10: Experimental setup used to measure the exciton's FSS. Since the two biexciton-exciton recombination pathways result in orthogonal polarizations and slightly different energies, it is expected that the transmitted signals for various angles $\alpha/2$ of the HWP will show a slight shift relative to each other.

The polarization selection is done by using a polarizing beamsplitter placed immediately at the exit of the cryostat, which only allows the polarization state $|H\rangle$ horizontal in the lab frame to pass. As viewed from the observer positioned at $+\infty\ \hat{z}$, $|H\rangle$ is the linear polarization defined with the propagating wave's electric field vector parallel to the lab floor and pointing to the right, which corresponds with the positive direction along the x-axis. Consistent with a right handed coordinate system, $|V\rangle$ is the orthogonal linear polarization and has its electric field vector pointing toward the lab ceiling, positive along the y-axis.

A HWP placed just before the PBS rotates a precise linear polarization to $|H\rangle$, allowing the polarization measured to be deliberately selected. For example, to measure $|V\rangle$, which has its electric field vector rotated by $\alpha = \frac{\pi}{2}$ counterclockwise around $+\hat{z}$, one would position the HWP with its slow axis at an angle of $\frac{\alpha}{2} = \frac{\pi}{4}$ with respect to the x-axis. Similarly, the diagonal and antidiagonal polarizations $|D\rangle$ and $|A\rangle$ can be measured by rotating the HWP's slow axis to $\frac{\pi}{8}$ and $\frac{3\pi}{8}$ respectively. Functionally, the HWP/PBS combination acts like a polarizing filter, except where most polarizers cause a slight beam deflection, the wave-plate and beam cube do not. This is important because the tolerance on beam location for optimal coupling into the EOM's waveguide as discussed in section 5.1 is extremely tight.

The diagram in Figure 5.10 shows the components involved in measuring the exciton's FSS. The HWP and PBS are used for polarization selection, as just discussed, while the scanning FP cavity and APD are studied in subsection 5.2.1. The EOM is included in the experiment simply because it will become useful when actually shifting the exciton's frequency. Running the current experiment while passing the photons through the EOM's waveguide further validates that a sufficiently strong signal is present to proceed with the frequency shifting explored in section 5.3.

With everything in place, ten measurements were taken for polarization angles varying from $\alpha = 0°..180°$ in 20° increments. Figure 5.11a) shows the fitted datapoints from the ten different angles for FP voltages between $0 \leq V_{\text{FP}} \leq 10$. Photon counts were collected from the APD during a 0.4 s integration time every 0.03 V and are plotted with higher counts further right on the x-axis. The trials took under 3 minutes each and are offset from one another for clarity.

The easiest data to extract from the ten plots in Figure 5.11a) is the relationship between energy and the voltage applied to the FP. Visible in each plot is a repeating pattern, a similar characteristic as was found in Figure 5.9. In this case the peaks ★ and ❖ are much broader as compared to their spacing, and their centres can be found by doing a least-squares fit to a set of peaks with Voigt profiles. The best-fit curve for each dataset is shown as a solid line, and each Voigt component is also plotted in dashes.

The difference between centres for ★ and ❖ is, just as in subsection 5.2.1, equivalent to an energy difference of one FSR, or 10 GHz for this FP. The corresponding voltages are distilled in Table 5.2, given as negative values since higher voltages represent a lower cavity resonance energy for the same mode. On average, one volt is equivalent to a shift in energy of $\Delta E = -2.030\,\text{GHz}$.

The next interesting feature of Figure 5.11a) is that the curves for different polarizations appear shifted with respect to one another. Centre values and linewidths for the peaks marked ★ and ❖ are plotted respectively in Figure 5.11b) and c) along with their 1σ confidence intervals. In both cases the peaks exhibit similar changes with respect to polarization: the energy for angle 100° is highest (its peaks' centres are lowest overall in terms of FP voltage), while the energy for 0° and 180° are lowest. The peak energies for

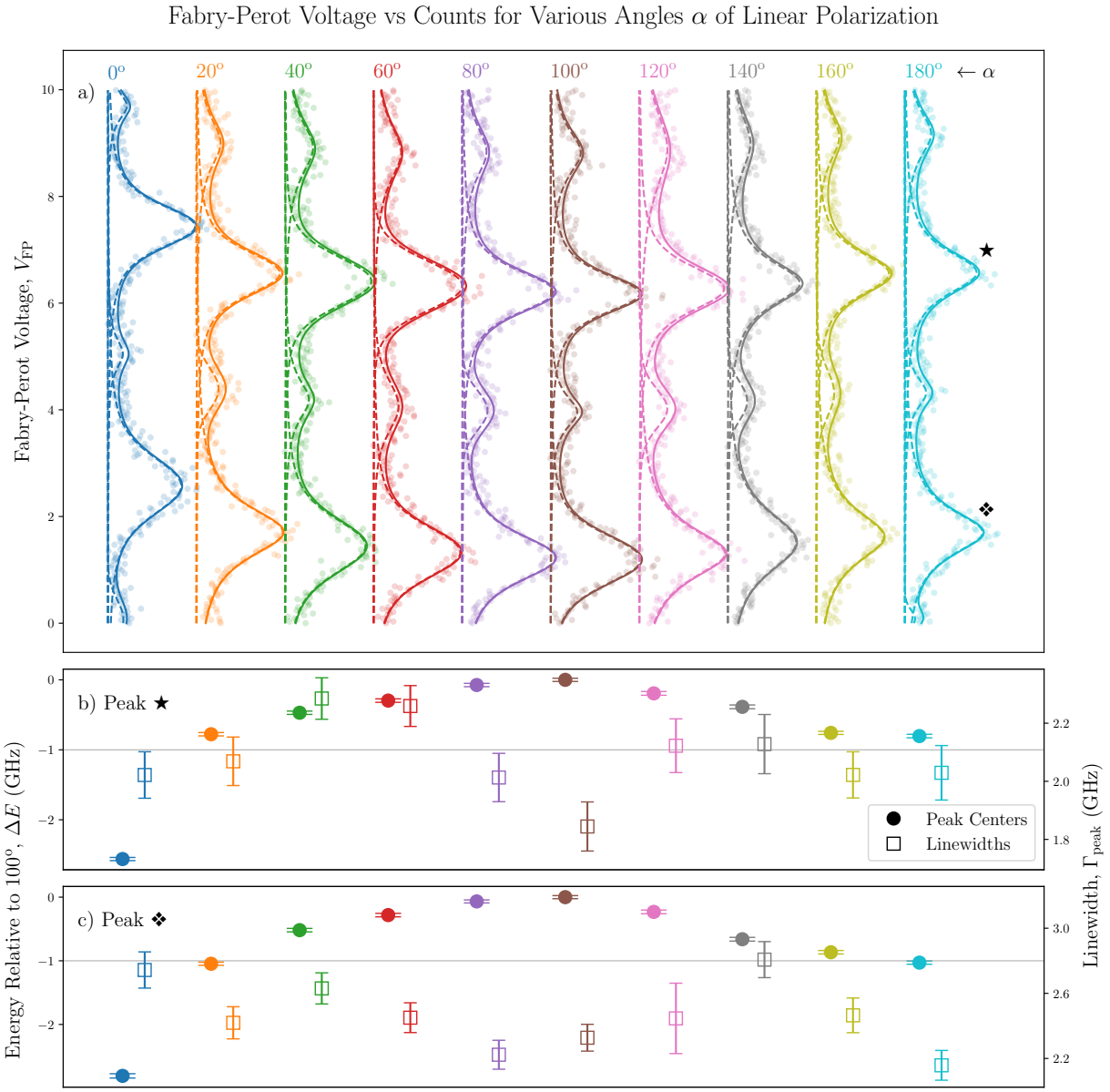

Figure 5.11: One scan of the Fabry-Perot for various input polarization angles. See main text for detailed discussion.

Polarization Angle	0°	20°	40°	60°	80°	100°	120°	140°	160°	180°	Average
Volts per 10 GHz	-4.862	-4.852	-4.960	-4.991	-4.987	-4.984	-4.965	-4.848	-4.931	-4.873	-4.9253
GHz per Volt	-2.057	-2.061	-2.016	-2.004	-2.005	-2.006	-2.014	-2.063	-2.028	-2.052	-2.030

Table 5.2: Calculating the relationship between volts supplied to the scanning FP cavity and change in transmitted signal energy. The numbers in the Volts per 10 GHz column are the differences in voltage of the fitted peak centers for peaks ★ and ❖ in Figure 5.11. That separation corresponds to a change of energy equal to the FP's FSR, which is 10 GHz in this case. Note that higher voltages correspond to lower energy for the same FP mode, making the Volts per 10 GHz numbers negative.

the intermediate polarizations fall in the middle and form an almost sinusoidal pattern. Since the energy for the peak at 100° is a unique extremum in the dataset, it was chosen as the energy reference relative to which the energy of peaks in other polarizations are determined.

Additionally, the 100° dataset is special because it has the absolute lowest measured peak linewidth Γ_X for ★ at 1.840(85) GHz. The second absolute lowest is also ★ but for 80° at 2.01(8) GHz. Looking at peak ❖ for 80° and 100° shows the same characteristic smaller-than-average linewidth at 2.22(9) GHz and 2.33(8) GHz respectively, but peak ❖'s lowest overall linewidth is 2.16(9) GHz for the 180° line.

It is expected that the smallest linewidth will correspond to a maximum or minimum in terms of energy, since this will be the polarization setting that performs a projective measurement maximizing the probability of seeing only one of the two exciton recombination pathways. Looking at Figure 5.11b) and c), this appears to be the case with the narrow peaks for 0° and 180° ($|H\rangle$ and $-|H\rangle$ in the lab frame) corresponding to the lowest energies while 80° and 100° ($\pm 10°$ from $|V\rangle$) correspond to the highest. The relative energy measured for peak 0° appears to be an outlier because it doesn't fit the trend of the other nine datasets, including the redundant measurement for $|H\rangle$ at 180°, so it will be neglected in the calculation for the exciton's FSS.

It should be noted that there is no reason $|H\rangle$ and $|V\rangle$ in the lab frame should be the polarization eigenstates of the exciton. Due to the non-zero FSS and absence of birefringence in the nanowire waveguide [67], it is expected that the stationary polarization states

Pol. Angle	100°	180°	Measured FSS
$\Delta E_{\text{ Peak }\bigstar}$	0 GHz	−0.804(25) GHz	0.804(25) GHz
$\Delta E_{\text{ Peak }\text{❖}}$	0 GHz	−1.029(26) GHz	1.029(26) GHz

Table 5.3: The spacing in energy between the highest and lowest peaks for ★ and ❖. The highest energy peaks are in the 1.029(26) GHz 100° dataset, while the lowest energy peaks are in 180° (discounting the dataset collected for 0°, see main text). The associated polarizations are $|V\rangle + 10°$ and $|H\rangle$ in the lab frame respectively.

for the photons emitted by exciton's recombination are linear, but the fact that that set of linear bases largely agree with the chosen $|H\rangle$ and $|V\rangle$ bases in the lab frame means that the dipole created by the electron and hole in the quantum dot must be oriented just so.

Also, since $|H\rangle$ and $|V\rangle$ in the lab frame are the stationary states of the biexciton-exciton cascade, the wider peaks in the exciton spectrum for the curves corresponding to $|D\rangle$ and $|A\rangle$ at 45° and 135° should actually be the composition of two separate narrower peaks of similar amplitude: the one higher in energy for $|V\rangle$ and the one lower in energy for $|H\rangle$. In fact, using a little imagination, one can almost see the two peaks emerge in the datapoints for peak ★ at 60° and 140°, and likewise for ❖ at 40°. The Raleigh criterion requires that in order to be resolvable, two peaks of full-width at half maxmium Γ_{FWHM} must have their centres separated by at least Γ_{FWHM}. In our case, the lowest linewidth is $\Gamma_{|V\rangle} = 1.84\,\text{GHz}$, so the peaks energies must be at least this far apart for both to emerge.

This naturally leads to the fundamental question of this section: what is the separation in energy of the two exciton eigenstates? Answering that requires finding the energy difference between the two polarization eigenstates, which should also correspond to the largest and smallest energies measured. Those are found in the 100° and 180° measurements respectively. As in Figure 5.11b) and c), the energies given are relative to the peak centres found for the 100° polarization, and are tabulated in Table 5.3.

Depending on the choice of peak, we find that the FSS for the exciton is FSS = 0.804(25) GHz or FSS = 1.029(26) GHz. This is a positive result since it reaffirms the previous measurement of FSS equal to 795.52(35) MHz [67]. It also explains why the two individual peaks in the $|D\rangle$ and $|A\rangle$ datasets cannot be resolved: the fine structure splitting

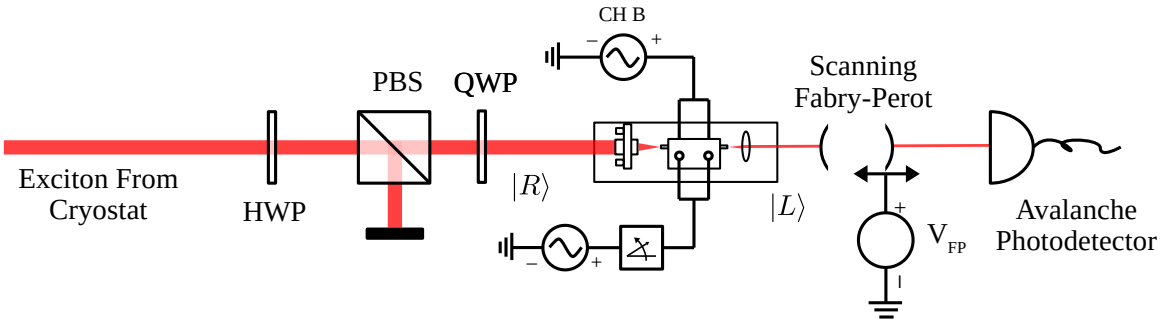

Figure 5.12: Experimental schematic for energy shifting the exciton using an EOM configured as a rotating half-wave plate.

is smaller than the exciton's linewidth $\Gamma_X \approx 2\,\text{GHz}$ by about half, so the Raleigh criterion is not met.

Note that in general this procedure cannot be used, as it will tend to underestimate the real FSS [19]. The reason is that although the QD's eigenstates are rectilinear, the nanowire may introduce a birefringence that causes them to be emitted elliptically. Thus, performing energy measurements in a strictly rectilinear basis will not capture the larger energy splitting that could be hiding in two orthogonal elliptically polarized states. Fortunately, the nanowire under study has been carefully grown such that it does not have any birefringence meaning the measurements as performed are representative.

With the encouragement that the experimental setup appears valid for accurately measuring small changes in the exciton's energy, we have reached the main undertaking of this thesis: demonstrating frequency shifting of single photons using a quickly rotating half-wave plate.

5.3 Frequency Shifting Single Photons

All of the relevant background material for frequency shifting single photons is now clear and the necessary experimental components are in place, so it is appropriate to commence

the true test. The key components for the experiment are organized as pictured in Figure 5.12. The PBS and QWP are used to create right-circularly polarized light, while the HWP is rotated until the counts on the APD are maximized.

Performing the maximization like this does not necessarily select one of the two branches of the biexciton-exciton cascade, since the optical components between the cryostat and the HWP/PBS combination are equivalent to a unitary operation and do not necessarily maintain what were the horizontal and vertical polarizations when the FSS measurement was done in section 5.2. In this case this isn't a concern: the result is that the measured exciton linewidth will be composed of the two slightly-different exciton energies and thus be broader than in the ideal case. A demonstration of frequency shifting will still be possible, though.

To first get an idea of what successful frequency shifting would look like, an exciton line shape was extracted with a least-squares Voigt fit to a data set collected from the FP. This line shape will then be used for a simulation.

In order to create a reasonable simulated shift, data was extracted from the second dataset in subsection 4.4.2. Using the left-hand bank of seven Lorentzian peaks in the fit from Figure 4.13 (red line), a convolutional kernel was created. The kernel is the result of integrating the area of each of the seven peaks and concentrating them at the peaks' respective centers, followed by a normalization step. The reasoning is that the observed linewidth in Figure 4.13 is primarily due to the 67 MHz resolution of the FP cavity, and thus the peaks' widths can be reasonably compressed.

The convolutional kernel was then applied to the exciton lineshape, as shown in blue in Figure 5.13. The convolutional kernel is displayed in the inset, also in blue, along with the original Lorentzian fit in orange. After convolving the exciton with the kernel, the result of which is shown in red, a new fit was done with another Voigt profile, dashed brown. Its centre as well as the original centre are drawn on the graph, and it was found that the difference in energy between them is 137.5 MHz. In addition, the linewidth of the converted peak has been broadened. It was confirmed that the integrated area of the exciton peak before and after the operation is identical. Note that higher Fabry-Perot voltages correspond to lower energies, so a rightward shift is to a lower frequency.

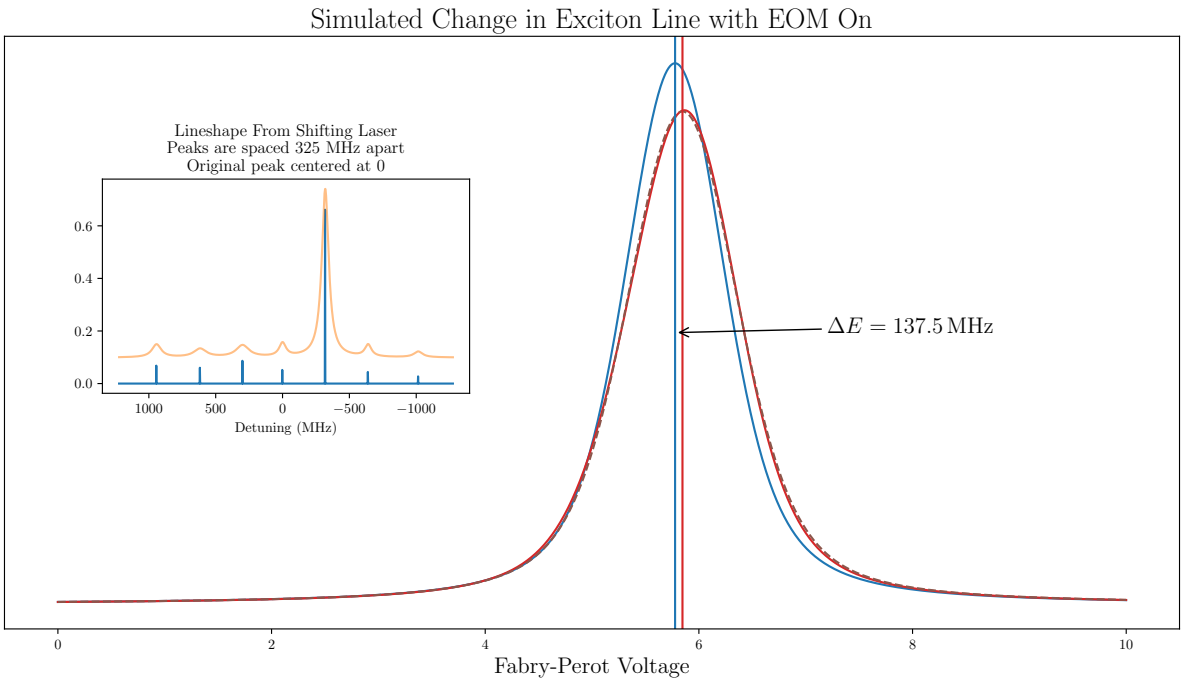

Figure 5.13: Simulating the expected frequency shift for the inset applied EOM signal from subsection 4.4.2.

A lower magnitude shift appeared in the simulated results than the expected 325 MHz at which the EOM was driven for the second dataset in subsection 4.4.2. The reason is clear from looking at the convolutional kernel, which on average shifts the energy to the right but also spreads it across a range of 2 GHz. This same energy spreading was not apparent in the first dataset from subsection 4.4.2 shown in Figure 4.12, meaning an optimistic outlook is reasonable on the grounds that significant improvements can be made.

Single photon data was collected on the APD for photons traveling through the EOM, just as in subsection 5.2.2, over seven different runs of the experiment. The first data collection sequence was with the EOM off, while the second was with it turned on. The following five data sets then followed the off-on pattern. Each of the datasets was then analyzed with a least-squares fit to a series of Voigt lineshapes, from which the peak centres were extracted. Adjacent datasets were then plotted together along with the fits. The complete figure is shown in Figure 5.14.

In graph a), the first trial, the blue dataset was the first to be collected, while the red points were second. In graph b), the second trial, the red data points are the same as in graph a), as can be seen by looking at the peak centres. The blue points, however, corresponds to the third collection run. Following the pattern, graph c) features the same blue points as in graph b), but new red points. In total, six comparisons can be created from seven collection sequences. The purpose of interleaving results like this is to avoid an accidental bias introduced by experimental methods, providing better uniformity in the possible sources of noise and experimental error. In each case, the data points taken while the EOM is on are expected to be red shifted (to the right), and are thus appropriately colored.

The parameters for the experiment are very similar to those used for collecting the simulation's convolutional kernel. To be rigorously complete, the EOM was driven with $0.254\,\mathrm{mV_{RMS}}$ (1.107 dBm, 0.93 in the code) from the DAC with a 105° phase difference between channels A and B. The signal was amplified 37 dB, as in subsection 4.4.2. Channel A's offset was $V_{\mathrm{A,DC}} = -5.80\,\mathrm{V}$ while for channel B it was $V_{\mathrm{B,DC}} = 7.68\,\mathrm{V}$.

The quantum dot was excited using a Ti:Sapphire laser set to 830 nm with a laser power of 74.6 nW (174 nW displayed on the 70% monitoring output of a non-polarizing

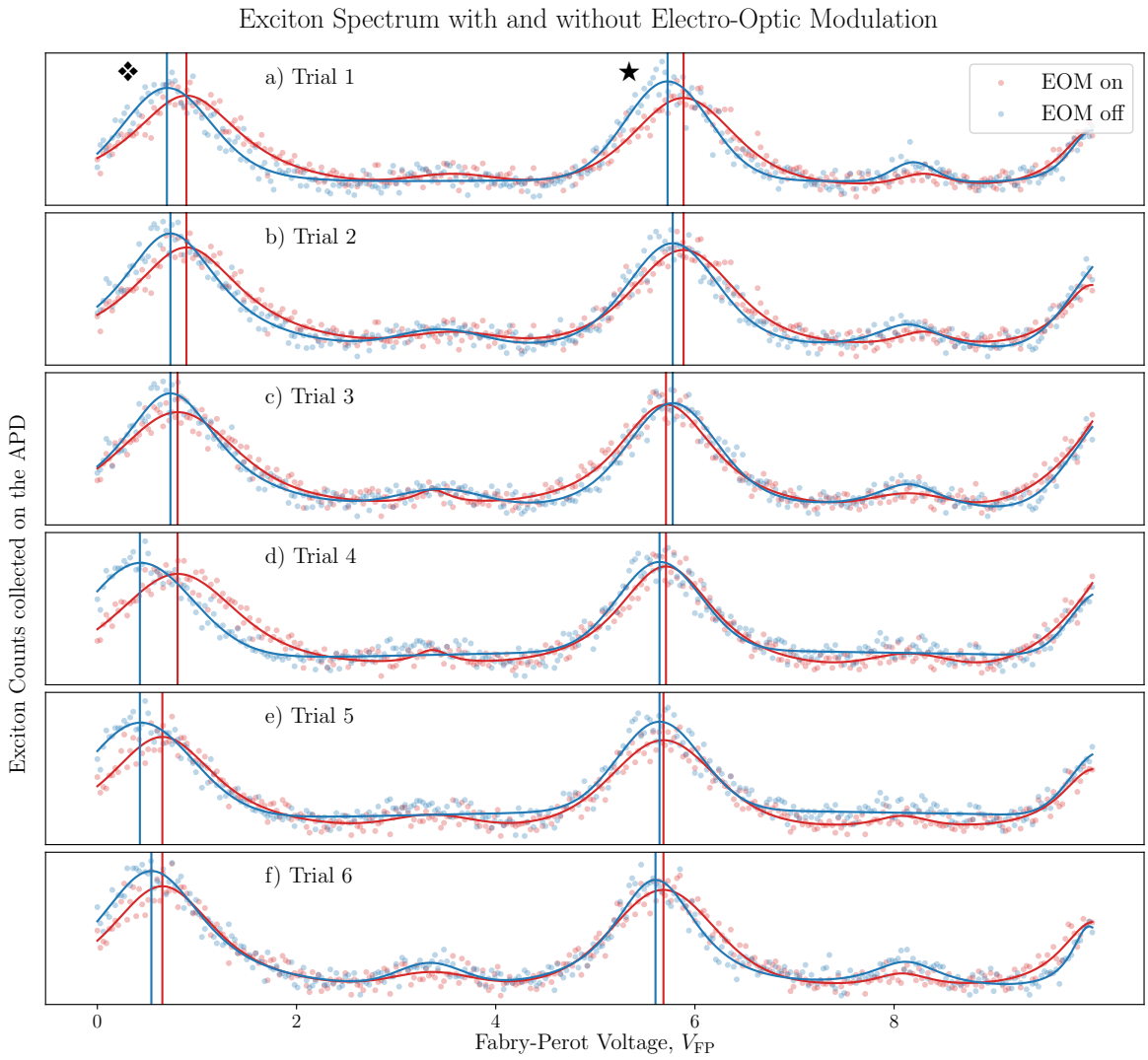

Figure 5.14: A sequence of trials with the EOM off and on. Critically, the centers for the red lines are consistently right of the blue centers, which is exactly what was predicted by the simulation in Figure 5.13. Every trial shares a dataset with the next, which can be seen by comparing the centre lines. For example Trial 1 and Trial 2 feature the same data for the EOM on, in red. This shows that the results are not an artifact of the measurement order.

Trial	1	2	3	4	5	6	Average
$\Delta E_{❖}$ (MHz)	-388.8	-318.6	-142.7	-751.2	-447.7	-218.9	-377.98
$\Delta E_{★}$ (MHz)	-318.8	-216.1	134.6	-128.8	-78.7	-158.7	-127.75
Combined:							-252.87

Table 5.4: Energy differences extracted from the peak centres of each trial. The negative signs denote a shift toward lower frequency with respect to the unshifted data.

beam splitter prior to entering the cryostat). The data points are spaced by positive increments of 0.03 V between 0 V and 10 V on the scanning FP piezo motor. Each cavity length was held steady for a 0.4 s integration time before advancing to the next higher voltage, for a total experiment time of around 3 min per collection sequence.

The 150 groove per mm grating was chosen in the spectrometer to maximize counts to the APD. A slit in front of the APD was opened to 70 µm, and positioned at 894.1 nm, corresponding to the exciton's wavelength. This is a different value than was found in the spectrum from Figure 5.7, and is due to the choice of grating and a slight wavelength mismatch between collection with the CCD and the APD.

In almost every case it is apparent that the centre of the peaks with the EOM running appear to the right of those when it isn't, consistent with the simulation. The one outlier is peak ★ in trial 3, where the red centre is left of the blue reference. Also consistent with the simulation is the broader average linewidth of the peaks in the red dataset. Another observation is that the peaks are more closely spaced for peak ★ than for peak ❖, and on average tend to drift toward the left across trials.

Extracting the energy difference between peaks just as was done in the simulation led to the values populated in Table 5.4. Taking the global average over the six comparisons, it is determined that the exciton line has indeed been down-converted by 252.87 MHz. This is confirmation that the rotating half-wave plate is functioning as a frequency shifter. However, this measured value is larger than the 137.5 MHz value that was expected based on the simulation in Figure 5.13. Instead, the average value for peak ★ matches much more closely with an average 127.75 MHz shift.

Interestingly, this observation is consistent with the measurements using the FP in

subsection 5.2.2, where peak ❖ had quite a large mismatch between the obtained and expected value, whereas peak ★ matched very well. The conclusion is that the FP collects more accurate results away from its starting voltage, which could be an artifact of hysteresis in the piezo cavity length adjuster. Thus, in the future the FP should be primed prior to running a data collection sequence. A direct consequence of this is the measurements relating the FP's free spectral range to energy may have a larger error on them since the first peak in the FSR pair may not be accurately positioned.

5.4 Conclusion

The conclusion that can be drawn from the data as analyzed is that an electro-optic modulator is indeed a viable method for controlling the energy of single photons. Though the frequency shift shown here is less than the 400 MHz required to correct for the exciton's fine structure, the theory and modeling very consistently matched with the results, providing high confidence that refinements in the technique can indeed be used to perfectly correct for the quantum dot's FSS. As such, it is expected that application of this technique will restore perfect entanglement for photon pairs created by the biexciton-exciton cascade, favourably positioning this on-demand source of entangled photons for use in ground-breaking future quantum technologies.

References

[1] A. Fognini, A. Ahmadi, S. J. Daley, M. E. Reimer, and V. Zwiller, "Universal fine-structure eraser for quantum dots," *Opt. Express*, vol. 26, no. 19, pp. 24 487–24 496, Sep 2018. [Online]. Available: http://www.opticsexpress.org/abstract.cfm?URI=oe-26-19-24487

[2] A. Einstein, "On a heuristic point of view about the creation and conversion of light," *Annalen der Physik*, vol. 322, no. 6, pp. 132–148, 1905. [Online]. Available: https://onlinelibrary.wiley.com/doi/abs/10.1002/andp.19053220607

[3] J. C. Maxwell, "Viii. a dynamical theory of the electromagnetic field," *Philosophical Transactions of the Royal Society of London*, vol. 155, pp. 459–512, 1865. [Online]. Available: https://doi.org/10.1098/rstl.1865.0008

[4] D. F. V. James, P. G. Kwiat, W. J. Munro, and A. G. White, "Measurement of qubits," *Phys. Rev. A*, vol. 64, p. 052312, Oct 2001. [Online]. Available: https://link.aps.org/doi/10.1103/PhysRevA.64.052312

[5] M. A. Nielsen and I. L. Chuang, *Quantum circuits.* Cambridge University Press, 2010, p. 171–215.

[6] J. F. Clauser, "Experimental distinction between the quantum and classical field-theoretic predictions for the photoelectric effect," *Phys. Rev. D*, vol. 9, pp. 853–860, Feb 1974. [Online]. Available: https://link.aps.org/doi/10.1103/PhysRevD.9.853

[7] G. H. Nussbaum and F. M. Pipkin, "Correlation of photons in cascade and the coherence time of the 6^3p_1 state of mercury," *Phys. Rev. Lett.*, vol. 19,

pp. 1089–1092, Nov 1967. [Online]. Available: https://link.aps.org/doi/10.1103/PhysRevLett.19.1089

[8] A. Aspect, P. Grangier, and G. Roger, "Experimental tests of realistic local theories via bell's theorem," *Phys. Rev. Lett.*, vol. 47, pp. 460–463, Aug 1981. [Online]. Available: https://link.aps.org/doi/10.1103/PhysRevLett.47.460

[9] H. J. Kimble, M. Dagenais, and L. Mandel, "Photon antibunching in resonance fluorescence," *Phys. Rev. Lett.*, vol. 39, pp. 691–695, Sep 1977. [Online]. Available: https://link.aps.org/doi/10.1103/PhysRevLett.39.691

[10] N. B. Manson, J. P. Harrison, and M. J. Sellars, "Nitrogen-vacancy center in diamond: Model of the electronic structure and associated dynamics," *Phys. Rev. B*, vol. 74, p. 104303, Sep 2006. [Online]. Available: https://link.aps.org/doi/10.1103/PhysRevB.74.104303

[11] L. M. Pham, "Magnetic field sensing with nitrogen-vacancy color centers in diamond," Ph.D. dissertation, Harvard University, 2013.

[12] C. Kurtsiefer, S. Mayer, P. Zarda, and H. Weinfurter, "Stable solid-state source of single photons," *Phys. Rev. Lett.*, vol. 85, pp. 290–293, Jul 2000. [Online]. Available: https://link.aps.org/doi/10.1103/PhysRevLett.85.290

[13] H. Bernien, B. Hensen, W. Pfaff, G. Koolstra, M. S. Blok, L. Robledo, T. H. Taminiau, M. Markham, D. J. Twitchen, L. Childress, and R. Hanson, "Heralded entanglement between solid-state qubits separated by three metres," *Nature*, vol. 497, no. 7447, pp. 86–90, May 2013. [Online]. Available: https://doi.org/10.1038/nature12016

[14] E. Togan, Y. Chu, A. S. Trifonov, L. Jiang, J. Maze, L. Childress, M. V. G. Dutt, A. S. Sørensen, P. R. Hemmer, A. S. Zibrov, and M. D. Lukin, "Quantum entanglement between an optical photon and a solid-state spin qubit," *Nature*, vol. 466, no. 7307, pp. 730–734, Aug 2010. [Online]. Available: https://doi.org/10.1038/nature09256

[15] W. Pfaff, B. J. Hensen, H. Bernien, S. B. van Dam, M. S. Blok, T. H. Taminiau, M. J. Tiggelman, R. N. Schouten, M. Markham, D. J. Twitchen, and R. Hanson, "Unconditional quantum teleportation between distant solid-state quantum bits," *Science*, vol. 345, no. 6196, pp. 532–535, 2014. [Online]. Available: https://science.sciencemag.org/content/345/6196/532

[16] B. Hensen, H. Bernien, A. E. Dréau, A. Reiserer, N. Kalb, M. S. Blok, J. Ruitenberg, R. F. L. Vermeulen, R. N. Schouten, C. Abellán, W. Amaya, V. Pruneri, M. W. Mitchell, M. Markham, D. J. Twitchen, D. Elkouss, S. Wehner, T. H. Taminiau, and R. Hanson, "Loophole-free bell inequality violation using electron spins separated by 1.3 kilometres," *Nature*, vol. 526, no. 7575, pp. 682–686, Oct 2015. [Online]. Available: https://doi.org/10.1038/nature15759

[17] M. Törpe, "Energy gap vs. lattice constant," http://lab.frumania.com/wp-content/uploads/2010/06/bandgap_edit-1024x804.jpg, 2010, [Online; accessed December 4th, 2019]. [Online]. Available: http://lab.frumania.com/wp-content/uploads/2010/06/bandgap_edit-1024x804.jpg

[18] J. Márquez, L. Geelhaar, and K. Jacobi, "Atomically resolved structure of InAs quantum dots," *Applied Physics Letters*, vol. 78, no. 16, pp. 2309–2311, 2001. [Online]. Available: https://doi.org/10.1063/1.1365101

[19] T. Huber, A. Predojević, M. Khoshnegar, D. Dalacu, P. J. Poole, H. Majedi, and G. Weihs, "Polarization entangled photons from quantum dots embedded in nanowires," *Nano Letters*, vol. 14, no. 12, pp. 7107–7114, 2014, pMID: 25395237. [Online]. Available: https://doi.org/10.1021/nl503581d

[20] T. Heindel, S. Rodt, and S. Reitzenstein, "Single-photon sources based on deterministic quantum-dot microlenses," in *Quantum Dots for Quantum Information Technologies*, P. Michler, Ed. Cham: Springer International Publishing, 2017, pp. 199–232. [Online]. Available: https://doi.org/10.1007/978-3-319-56378-7_6

[21] F. Ding and O. G. Schmidt, "Polarization entangled photons from semiconductor quantum dots," in *Quantum Dots for Quantum Information Technologies*,

P. Michler, Ed. Cham: Springer International Publishing, 2017, pp. 235–266. [Online]. Available: https://doi.org/10.1007/978-3-319-56378-7_7

[22] S. L. Portalupi and P. Michler, "Resonantly excited quantum dots: Superior non-classical light sources for quantum information," in *Quantum Dots for Quantum Information Technologies*, P. Michler, Ed. Cham: Springer International Publishing, 2017, pp. 77–121. [Online]. Available: https://doi.org/10.1007/978-3-319-56378-7_3

[23] M. Müller, S. Bounouar, K. D. Jöns, M. Glässl, and P. Michler, "On-demand generation of indistinguishable polarization-entangled photon pairs," *Nature Photonics*, vol. 8, no. 3, pp. 224–228, Mar 2014. [Online]. Available: https://doi.org/10.1038/nphoton.2013.377

[24] H. Wang, Y.-M. He, T.-H. Chung, H. Hu, Y. Yu, S. Chen, X. Ding, M.-C. Chen, J. Qin, X. Yang, R.-Z. Liu, Z.-C. Duan, J.-P. Li, S. Gerhardt, K. Winkler, J. Jurkat, L.-J. Wang, N. Gregersen, Y.-H. Huo, Q. Dai, S. Yu, S. Höfling, C.-Y. Lu, and J.-W. Pan, "Towards optimal single-photon sources from polarized microcavities," *Nature Photonics*, vol. 13, no. 11, pp. 770–775, Nov 2019. [Online]. Available: https://doi.org/10.1038/s41566-019-0494-3

[25] P. Senellart, G. Solomon, and A. White, "High-performance semiconductor quantum-dot single-photon sources," *Nature Nanotechnology*, vol. 12, no. 11, pp. 1026–1039, Nov 2017. [Online]. Available: https://doi.org/10.1038/nnano.2017.218

[26] M. E. Reimer and C. Cher, "The quest for a perfect single-photon source," *Nature Photonics*, vol. 13, no. 11, pp. 734–736, Nov 2019. [Online]. Available: https://doi.org/10.1038/s41566-019-0544-x

[27] S. Aaronson and A. Arkhipov, "The computational complexity of linear optics," 2010.

[28] E. Knill, R. Laflamme, and G. J. Milburn, "A scheme for efficient quantum computation with linear optics," *Nature*, vol. 409, no. 6816, pp. 46–52, Jan 2001. [Online]. Available: https://doi.org/10.1038/35051009

[29] P. Kok, W. J. Munro, K. Nemoto, T. C. Ralph, J. P. Dowling, and G. J. Milburn, "Linear optical quantum computing with photonic qubits," *Rev. Mod. Phys.*, vol. 79, pp. 135–174, Jan 2007. [Online]. Available: https://link.aps.org/doi/10.1103/RevModPhys.79.135

[30] C. Santori, M. Pelton, G. Solomon, Y. Dale, and Y. Yamamoto, "Triggered single photons from a quantum dot," *Phys. Rev. Lett.*, vol. 86, pp. 1502–1505, Feb 2001. [Online]. Available: https://link.aps.org/doi/10.1103/PhysRevLett.86.1502

[31] C. Santori, D. Fattal, J. Vučković, G. S. Solomon, and Y. Yamamoto, "Indistinguishable photons from a single-photon device," *Nature*, vol. 419, no. 6907, pp. 594–597, Oct 2002. [Online]. Available: https://doi.org/10.1038/nature01086

[32] Y.-M. He, Y. He, Y.-J. Wei, D. Wu, M. Atatüre, C. Schneider, S. Höfling, M. Kamp, C.-Y. Lu, and J.-W. Pan, "On-demand semiconductor single-photon source with near-unity indistinguishability," *Nature Nanotechnology*, vol. 8, no. 3, pp. 213–217, Mar 2013. [Online]. Available: https://doi.org/10.1038/nnano.2012.262

[33] X. Ding, Y. He, Z.-C. Duan, N. Gregersen, M.-C. Chen, S. Unsleber, S. Maier, C. Schneider, M. Kamp, S. Höfling, C.-Y. Lu, and J.-W. Pan, "On-demand single photons with high extraction efficiency and near-unity indistinguishability from a resonantly driven quantum dot in a micropillar," *Phys. Rev. Lett.*, vol. 116, p. 020401, Jan 2016. [Online]. Available: https://link.aps.org/doi/10.1103/PhysRevLett.116.020401

[34] N. Somaschi, V. Giesz, L. De Santis, J. C. Loredo, M. P. Almeida, G. Hornecker, S. L. Portalupi, T. Grange, C. Antón, J. Demory, C. Gómez, I. Sagnes, N. D. Lanzillotti-Kimura, A. Lemaítre, A. Auffeves, A. G. White, L. Lanco, and P. Senellart, "Near-optimal single-photon sources in the solid state," *Nature Photonics*, vol. 10, no. 5, pp. 340–345, May 2016. [Online]. Available: https://doi.org/10.1038/nphoton.2016.23

[35] D. Huber, M. Reindl, Y. Huo, H. Huang, J. S. Wildmann, O. G. Schmidt, A. Rastelli, and R. Trotta, "Highly indistinguishable and strongly entangled photons

from symmetric gaas quantum dots," *Nature Communications*, vol. 8, no. 1, p. 15506, May 2017. [Online]. Available: https://doi.org/10.1038/ncomms15506

[36] O. Benson, C. Santori, M. Pelton, and Y. Yamamoto, "Regulated and entangled photons from a single quantum dot," *Phys. Rev. Lett.*, vol. 84, pp. 2513–2516, Mar 2000. [Online]. Available: https://link.aps.org/doi/10.1103/PhysRevLett.84.2513

[37] C. L. Salter, R. M. Stevenson, I. Farrer, C. A. Nicoll, D. A. Ritchie, and A. J. Shields, "An entangled-light-emitting diode," *Nature*, vol. 465, no. 7298, pp. 594–597, Jun 2010. [Online]. Available: https://doi.org/10.1038/nature09078

[38] J. Zhang, J. S. Wildmann, F. Ding, R. Trotta, Y. Huo, E. Zallo, D. Huber, A. Rastelli, and O. G. Schmidt, "High yield and ultrafast sources of electrically triggered entangled-photon pairs based on strain-tunable quantum dots," *Nature Communications*, vol. 6, no. 1, p. 10067, Dec 2015. [Online]. Available: https://doi.org/10.1038/ncomms10067

[39] Y. Chen, M. Zopf, R. Keil, F. Ding, and O. G. Schmidt, "Highly-efficient extraction of entangled photons from quantum dots using a broadband optical antenna," *Nature Communications*, vol. 9, no. 1, p. 2994, Jul 2018. [Online]. Available: https://doi.org/10.1038/s41467-018-05456-2

[40] M. A. M. Versteegh, M. E. Reimer, K. D. Jöns, D. Dalacu, P. J. Poole, A. Gulinatti, A. Giudice, and V. Zwiller, "Observation of strongly entangled photon pairs from a nanowire quantum dot," *Nature Communications*, vol. 5, no. 1, p. 5298, Oct 2014. [Online]. Available: https://doi.org/10.1038/ncomms6298

[41] J. Liu, R. Su, Y. Wei, B. Yao, S. F. C. d. Silva, Y. Yu, J. Iles-Smith, K. Srinivasan, A. Rastelli, J. Li, and X. Wang, "A solid-state source of strongly entangled photon pairs with high brightness and indistinguishability," *Nature Nanotechnology*, vol. 14, no. 6, pp. 586–593, Jun 2019. [Online]. Available: https://doi.org/10.1038/s41565-019-0435-9

[42] R. H. Brown and R. Q. Twiss, "Correlation between photons in two coherent beams of light," *Nature*, vol. 177, no. 4497, pp. 27–29, Jan 1956. [Online]. Available: https://doi.org/10.1038/177027a0

[43] P. Michler, A. Kiraz, C. Becher, W. V. Schoenfeld, P. M. Petroff, L. Zhang, E. Hu, and A. Imamoglu, "A quantum dot single-photon turnstile device," *Science*, vol. 290, no. 5500, pp. 2282–2285, 2000. [Online]. Available: https://science.sciencemag.org/content/290/5500/2282

[44] C. K. Hong, Z. Y. Ou, and L. Mandel, "Measurement of subpicosecond time intervals between two photons by interference," *Phys. Rev. Lett.*, vol. 59, pp. 2044–2046, Nov 1987. [Online]. Available: https://link.aps.org/doi/10.1103/PhysRevLett.59.2044

[45] S. Strauf, N. G. Stoltz, M. T. Rakher, L. A. Coldren, P. M. Petroff, and D. Bouwmeester, "High-frequency single-photon source with polarization control," *Nature Photonics*, vol. 1, no. 12, pp. 704–708, Dec 2007. [Online]. Available: https://doi.org/10.1038/nphoton.2007.227

[46] A. Dousse, J. Suffczyński, A. Beveratos, O. Krebs, A. Lemaître, I. Sagnes, J. Bloch, P. Voisin, and P. Senellart, "Ultrabright source of entangled photon pairs," *Nature*, vol. 466, no. 7303, pp. 217–220, Jul 2010. [Online]. Available: https://doi.org/10.1038/nature09148

[47] A. Muller, W. Fang, J. Lawall, and G. S. Solomon, "Creating polarization-entangled photon pairs from a semiconductor quantum dot using the optical stark effect," *Phys. Rev. Lett.*, vol. 103, p. 217402, Nov 2009. [Online]. Available: https://link.aps.org/doi/10.1103/PhysRevLett.103.217402

[48] R. B. Patel, A. J. Bennett, I. Farrer, C. A. Nicoll, D. A. Ritchie, and A. J. Shields, "Two-photon interference of the emission from electrically tunable remote quantum dots," *Nature Photonics*, vol. 4, no. 9, pp. 632–635, Sep 2010. [Online]. Available: https://doi.org/10.1038/nphoton.2010.161

[49] A. K. Nowak, S. L. Portalupi, V. Giesz, O. Gazzano, C. Dal Savio, P.-F. Braun, K. Karrai, C. Arnold, L. Lanco, I. Sagnes, A. Lemaître, and

P. Senellart, "Deterministic and electrically tunable bright single-photon source," *Nature Communications*, vol. 5, no. 1, p. 3240, Feb 2014. [Online]. Available: https://doi.org/10.1038/ncomms4240

[50] J. Zhang, E. Zallo, B. Höfer, Y. Chen, R. Keil, M. Zopf, S. Böttner, F. Ding, and O. G. Schmidt, "Electric-field-induced energy tuning of on-demand entangled-photon emission from self-assembled quantum dots," *Nano Letters*, vol. 17, no. 1, pp. 501–507, 2017, pMID: 27995799. [Online]. Available: https://doi.org/10.1021/acs.nanolett.6b04539

[51] L. Leandro, C. P. Gunnarsson, R. Reznik, K. D. Jöns, I. Shtrom, A. Khrebtov, T. Kasama, V. Zwiller, G. Cirlin, and N. Akopian, "Nanowire quantum dots tuned to atomic resonances," *Nano Letters*, vol. 18, no. 11, pp. 7217–7221, 2018, pMID: 30336054. [Online]. Available: https://doi.org/10.1021/acs.nanolett.8b03363

[52] R. Trotta, J. Martín-Sánchez, I. Daruka, C. Ortix, and A. Rastelli, "Energy-tunable sources of entangled photons: A viable concept for solid-state-based quantum relays," *Phys. Rev. Lett.*, vol. 114, p. 150502, Apr 2015. [Online]. Available: https://link.aps.org/doi/10.1103/PhysRevLett.114.150502

[53] Y. Chen, J. Zhang, M. Zopf, K. Jung, Y. Zhang, R. Keil, F. Ding, and O. G. Schmidt, "Wavelength-tunable entangled photons from silicon-integrated iii–v quantum dots," *Nature Communications*, vol. 7, no. 1, p. 10387, Jan 2016. [Online]. Available: https://doi.org/10.1038/ncomms10387

[54] R. Trotta, J. Martín-Sánchez, J. S. Wildmann, G. Piredda, M. Reindl, C. Schimpf, E. Zallo, S. Stroj, J. Edlinger, and A. Rastelli, "Wavelength-tunable sources of entangled photons interfaced with atomic vapours," *Nature Communications*, vol. 7, no. 1, p. 10375, Jan 2016. [Online]. Available: https://doi.org/10.1038/ncomms10375

[55] A. W. Elshaari, E. Büyüközer, I. E. Zadeh, T. Lettner, P. Zhao, E. Schöll, S. Gyger, M. E. Reimer, D. Dalacu, P. J. Poole, K. D. Jöns, and V. Zwiller, "Strain-tunable quantum integrated photonics," *Nano Letters*, vol. 18, no. 12, pp. 7969–7976, 2018, pMID: 30474987. [Online]. Available: https://doi.org/10.1021/acs.nanolett.8b03937

[56] A. Ulhaq, S. Weiler, S. M. Ulrich, R. Roßbach, M. Jetter, and P. Michler, "Cascaded single-photon emission from the mollow triplet sidebands of a quantum dot," *Nature Photonics*, vol. 6, no. 4, pp. 238–242, Apr 2012. [Online]. Available: https://doi.org/10.1038/nphoton.2012.23

[57] G. Bulgarini, M. E. Reimer, M. Bouwes Bavinck, K. D. Jöns, D. Dalacu, P. J. Poole, E. P. A. M. Bakkers, and V. Zwiller, "Nanowire waveguides launching single photons in a gaussian mode for ideal fiber coupling," *Nano Letters*, vol. 14, no. 7, pp. 4102–4106, 2014, pMID: 24926884. [Online]. Available: https://doi.org/10.1021/nl501648f

[58] S. Hepp, M. Jetter, S. L. Portalupi, and P. Michler, "Semiconductor quantum dots for integrated quantum photonics," *Advanced Quantum Technologies*, vol. 2, no. 9, p. 1900020, 2019. [Online]. Available: https://onlinelibrary.wiley.com/doi/abs/10.1002/qute.201900020

[59] T. M. Zhao, Y. Chen, Y. Yu, Q. Li, M. Davanco, and J. Liu, "Advanced technologies for quantum photonic devices based on epitaxial quantum dots," *Advanced Quantum Technologies*, vol. n/a, no. n/a, p. 1900034, 2019. [Online]. Available: https://onlinelibrary.wiley.com/doi/abs/10.1002/qute.201900034

[60] K. D. Jöns, L. Schweickert, M. A. M. Versteegh, D. Dalacu, P. J. Poole, A. Gulinatti, A. Giudice, V. Zwiller, and M. E. Reimer, "Bright nanoscale source of deterministic entangled photon pairs violating bell's inequality," *Scientific Reports*, vol. 7, no. 1, p. 1700, May 2017. [Online]. Available: https://doi.org/10.1038/s41598-017-01509-6

[61] T. Heindel, C. Schneider, M. Lermer, S. H. Kwon, T. Braun, S. Reitzenstein, S. Höfling, M. Kamp, and A. Forchel, "Electrically driven quantum dot-micropillar single photon source with 34% overall efficiency," *Applied Physics Letters*, vol. 96, no. 1, p. 011107, 2010. [Online]. Available: https://doi.org/10.1063/1.3284514

[62] S. Kreinberg, T. Grbešić, M. Strauß, A. Carmele, M. Emmerling, C. Schneider, S. Höfling, X. Porte, and S. Reitzenstein, "Quantum-optical spectroscopy of a two-level system using an electrically driven micropillar laser as a resonant

excitation source," *Light: Science & Applications*, vol. 7, no. 1, p. 41, Jul 2018. [Online]. Available: https://doi.org/10.1038/s41377-018-0045-6

[63] S. Daley, "Electro-optic rotating half-waveplate for a quantum dot fine-structure eraser," Master's thesis, University of Waterloo, 2019.

[64] D. Dalacu, K. Mnaymneh, X. Wu, J. Lapointe, G. C. Aers, P. J. Poole, and R. L. Williams, "Selective-area vapor-liquid-solid growth of tunable InAsP quantum dots in nanowires," *Applied Physics Letters*, vol. 98, no. 25, p. 251101, 2011. [Online]. Available: https://doi.org/10.1063/1.3600777

[65] D. Dalacu, K. Mnaymneh, J. Lapointe, X. Wu, P. J. Poole, G. Bulgarini, V. Zwiller, and M. E. Reimer, "Ultraclean emission from InAsP quantum dots in defect-free wurtzite inp nanowires," *Nano Letters*, vol. 12, no. 11, pp. 5919–5923, 2012, pMID: 23066839. [Online]. Available: https://doi.org/10.1021/nl303327h

[66] M. E. Reimer, G. Bulgarini, N. Akopian, M. Hocevar, M. B. Bavinck, M. A. Verheijen, E. P. Bakkers, L. P. Kouwenhoven, and V. Zwiller, "Bright single-photon sources in bottom-up tailored nanowires," *Nature Communications*, vol. 3, no. 1, p. 737, Mar 2012. [Online]. Available: https://doi.org/10.1038/ncomms1746

[67] A. Fognini, A. Ahmadi, M. Zeeshan, J. T. Fokkens, S. J. Gibson, N. Sherlekar, S. J. Daley, D. Dalacu, P. J. Poole, K. D. Jöns, V. Zwiller, and M. E. Reimer, "Dephasing free photon entanglement with a quantum dot," *ACS Photonics*, vol. 6, no. 7, pp. 1656–1663, 2019. [Online]. Available: https://doi.org/10.1021/acsphotonics.8b01496

[68] M. Bayer, G. Ortner, O. Stern, A. Kuther, A. A. Gorbunov, A. Forchel, P. Hawrylak, S. Fafard, K. Hinzer, T. L. Reinecke, S. N. Walck, J. P. Reithmaier, F. Klopf, and F. Schäfer, "Fine structure of neutral and charged excitons in self-assembled In(Ga)As/(Al)GaAs quantum dots," *Phys. Rev. B*, vol. 65, p. 195315, May 2002. [Online]. Available: https://link.aps.org/doi/10.1103/PhysRevB.65.195315

[69] R. Paschotta, "Fibre core," *RP Photonics Encyclopedia* [Online] https://www.rp-photonics.com/fiber_core.html, [Accessed: 7- Apr- 2018].

[70] S. Chuang, *Physics of Optoelectronic Devices*. New York: John Wiley & Sons, 1995.

[71] C. Q. *et al*, "Power-efficient electro-optical single-tone optical-frequency shifter using x-cut y-propagating lithium tantalate waveguide emulating a rotating half-wave-plate," in *Presented at Opt. Fib. Commun. Conf.*, 2017.

[72] R. Jones, "A new calculus for the treatment of optical systems," *J. Opt. Soc. Am.*, vol. 31, no. 7, pp. 488–493, 1941.

[73] A. Fox, "An adjustable wave-guide phase changer," *Proc. of the I.R.E.*, vol. 35, pp. 1489–1498, 1947.

[74] E. C. C. Buhrer, D. Baird, "Optical frequency shifting by electro-optic effect," *Appl. Phys. Lett.*, vol. 1, pp. 46–49, 1962.

[75] C. Q. *et al*, "Single-tone optical frequency shifting and nonmagnetic optical isolation by electro-optical emulation of a rotating half-wave plate in a traveling-wave lithium niobate waveguide," *IEEE Photon. J.*, vol. 9, no. 3, 2017.

[76] A. Fognini, "Pydualdds," 2018. [Online]. Available: https://github.com/afognini/PyDualDDS

[77] A. Yariv and P. Yeh, *Photonics: Optical Electronics in Modern Communications*. New York: Oxford University Press, 2006.

[78] M. Varnava, D. E. Browne, and T. Rudolph, "How good must single photon sources and detectors be for efficient linear optical quantum computation?" *Phys. Rev. Lett.*, vol. 100, p. 060502, Feb 2008. [Online]. Available: https://link.aps.org/doi/10.1103/PhysRevLett.100.060502

[79] P. Page and H. Pursey, "Tunable single sideband electro-optic ring modulator," *Optoelectronics*, vol. 2, pp. 1–4, 1970.

[80] J. Campbell and W. Steier, "Rotating-waveplate optical-frequency shifting in lithium niobate," *IEEE J. Quant. Elec.*, vol. 7, pp. 450–457, 1971.

[81] G. Sommargren, "Up/down frequency shifter for optical heterodyne interferometry," *J. Opt. Soc. Am.*, vol. 65, no. 8, pp. 960–961, 1975.

[82] B. Garetz and S. Arnold, "Variable frequency shifting of circularly polarized laser radiation via a rotating half-wave retardation plate," *Opt. Comm.*, vol. 31, no. 1, pp. 1–3, 1979.

[83] M. Kothiyal and C. Delisle, "Optical frequency shifter for heterodyne interferometry using counterrotating wave plates," *Opt. Lett.*, vol. 9, no. 8, pp. 319–321, 1984.

[84] L. Z. P. Gangding, H. Shangyuan, "Application of electro-optic frequency shifters in heterodyne interferometric systems," *Electron. Lett.*, vol. 22, no. 23, pp. 1215–1216, 1986.

[85] R. Noe and D. Smith, "Integrated-optic rotating waveplate frequency shifter," *Electron. Lett.*, vol. 24, no. 21, pp. 1348–1349, 1988.

[86] Z. A. G. Smith, D. Novak, "Technique for optical ssb generation to overcome dispersion penalties in fibre-radio systems," *Electron. Lett.*, vol. 33, no. 1, pp. 74–75, 1997.

[87] R. S. *et al*, "Evolution of entanglement between distinguishable light states," *Phys. Rev. Lett.*, vol. 101, no. 170501, 2008.

[88] S. Sanna and W. Schmidt, "Lithium niobate x-cut, y-cut, and z-cut surfaces from ab initio theory," *Phys. Rev. B*, vol. 81, no. 214116, 2010.

[89] P. Caroff, J. Bolinsson, and J. Johansson, "Crystal phases in iii–v nanowires: From random toward engineered polytypism," *IEEE Journal of Selected Topics in Quantum Electronics*, vol. 17, no. 4, pp. 829–846, July 2011.

[90] R. Singh and G. Bester, "Nanowire quantum dots as an ideal source of entangled photon pairs," *Phys. Rev. Lett.*, vol. 103, p. 063601, Aug 2009. [Online]. Available: https://link.aps.org/doi/10.1103/PhysRevLett.103.063601

[91] Z. He, J. Yang, L. Zhou, Y. Chen, T. Zhao, Y. Yu, and J. Liu, "Broadband photonic structures for quantum light sources," *Journal of Semiconductors*, vol. 40, no. 7, p. 071905, jul 2019. [Online]. Available: https://doi.org/10.1088%2F1674-4926%2F40%2F7%2F071905

[92] M. Reindl, K. D. Jöns, D. Huber, C. Schimpf, Y. Huo, V. Zwiller, A. Rastelli, and R. Trotta, "Phonon-assisted two-photon interference from remote quantum emitters," *Nano Letters*, vol. 17, no. 7, pp. 4090–4095, 2017, pMID: 28557459. [Online]. Available: https://doi.org/10.1021/acs.nanolett.7b00777

[93] T. Müller, J. Skiba-Szymanska, A. B. Krysa, J. Huwer, M. Felle, M. Anderson, R. M. Stevenson, J. Heffernan, D. A. Ritchie, and A. J. Shields, "A quantum light-emitting diode for the standard telecom window around 1,550 nm," *Nature Communications*, vol. 9, no. 1, p. 862, Feb 2018. [Online]. Available: https://doi.org/10.1038/s41467-018-03251-7

[94] F. Shahandeh, *The Resource Theory of Entanglement*. Cham: Springer International Publishing, 2019, pp. 61–109. [Online]. Available: https://doi.org/10.1007/978-3-030-24120-9_2

[95] S. Hill and W. K. Wootters, "Entanglement of a pair of quantum bits," *Phys. Rev. Lett.*, vol. 78, pp. 5022–5025, Jun 1997. [Online]. Available: https://link.aps.org/doi/10.1103/PhysRevLett.78.5022

[96] B. Lounis and W. E. Moerner, "Single photons on demand from a single molecule at room temperature," *Nature*, vol. 407, no. 6803, pp. 491–493, Sep 2000. [Online]. Available: https://doi.org/10.1038/35035032

[97] R. Hanbury Brown and R. Q. Twiss, "A test of a new type of stellar interferometer on sirius," *Nature*, vol. 178, no. 4541, pp. 1046–1048, Nov 1956. [Online]. Available: https://doi.org/10.1038/1781046a0

[98] D. Stoler, "Photon antibunching and possible ways to observe it," *Phys. Rev. Lett.*, vol. 33, pp. 1397–1400, Dec 1974. [Online]. Available: https://link.aps.org/doi/10.1103/PhysRevLett.33.1397

[99] L. Li, E. H. Chen, J. Zheng, S. L. Mouradian, F. Dolde, T. Schröder, S. Karaveli, M. L. Markham, D. J. Twitchen, and D. Englund, "Efficient photon collection from a nitrogen vacancy center in a circular bullseye grating," *Nano Letters*, vol. 15, no. 3, pp. 1493–1497, 2015, pMID: 25714414. [Online]. Available: https://doi.org/10.1021/nl503451j

[100] P. Michler, A. Imamoğlu, M. D. Mason, P. J. Carson, G. F. Strouse, and S. K. Buratto, "Quantum correlation among photons from a single quantum dot at room temperature," *Nature*, vol. 406, no. 6799, pp. 968–970, Aug 2000. [Online]. Available: https://doi.org/10.1038/35023100

[101] G. L. Tuin, "Optical characterization of wurtzite indium phosphide," Master's thesis, Lund University, 2010.

[102] M. Bayer, A. Kuther, A. Forchel, A. Gorbunov, V. B. Timofeev, F. Schäfer, J. P. Reithmaier, T. L. Reinecke, and S. N. Walck, "Electron and hole g factors and exchange interaction from studies of the exciton fine structure in $in_{0.60}ga_{0.40}As$ quantum dots," *Phys. Rev. Lett.*, vol. 82, pp. 1748–1751, Feb 1999. [Online]. Available: https://link.aps.org/doi/10.1103/PhysRevLett.82.1748

[103] R. Trotta, J. S. Wildmann, E. Zallo, O. G. Schmidt, and A. Rastelli, "Highly entangled photons from hybrid piezoelectric-semiconductor quantum dot devices," *Nano Letters*, vol. 14, no. 6, pp. 3439–3444, 2014, pMID: 24845369. [Online]. Available: https://doi.org/10.1021/nl500968k

[104] J. Wang, M. Gong, G.-C. Guo, and L. He, "Towards scalable entangled photon sources with self-assembled InAs/GaAs quantum dots," *Phys. Rev. Lett.*, vol. 115, p. 067401, Aug 2015. [Online]. Available: https://link.aps.org/doi/10.1103/PhysRevLett.115.067401

[105] A. Neville, C. Sparrow, R. Clifford, E. Johnston, P. M. Birchall, A. Montanaro, and A. Laing, "Classical boson sampling algorithms with superior performance to near-term experiments," *Nature Physics*, vol. 13, no. 12, pp. 1153–1157, Dec 2017. [Online]. Available: https://doi.org/10.1038/nphys4270

[106] E. Moreau, I. Robert, J. M. Gérard, I. Abram, L. Manin, and V. Thierry-Mieg, "Single-mode solid-state single photon source based on isolated quantum dots in pillar microcavities," *Applied Physics Letters*, vol. 79, no. 18, pp. 2865–2867, 2001. [Online]. Available: https://doi.org/10.1063/1.1415346

[107] C. Santori, D. Fattal, J. Vučković, G. S. Solomon, E. Waks, and Y. Yamamoto, "Submicrosecond correlations in photoluminescence from InAs quantum dots," *Phys. Rev. B*, vol. 69, p. 205324, May 2004. [Online]. Available: https://link.aps.org/doi/10.1103/PhysRevB.69.205324

[108] M. Pelton, C. Santori, J. Vucˇković, B. Zhang, G. S. Solomon, J. Plant, and Y. Yamamoto, "Efficient source of single photons: A single quantum dot in a micropost microcavity," *Phys. Rev. Lett.*, vol. 89, p. 233602, Nov 2002. [Online]. Available: https://link.aps.org/doi/10.1103/PhysRevLett.89.233602

[109] R. J. Glauber, "The quantum theory of optical coherence," *Phys. Rev.*, vol. 130, pp. 2529–2539, Jun 1963. [Online]. Available: https://link.aps.org/doi/10.1103/PhysRev.130.2529

[110] ——, "Coherent and incoherent states of the radiation field," *Phys. Rev.*, vol. 131, pp. 2766–2788, Sep 1963. [Online]. Available: https://link.aps.org/doi/10.1103/PhysRev.131.2766

[111] H. J. Kimble, "The quantum internet," *Nature*, vol. 453, no. 7198, pp. 1023–1030, Jun 2008. [Online]. Available: https://doi.org/10.1038/nature07127

[112] A. K. Ekert, "Quantum cryptography based on bell's theorem," *Phys. Rev. Lett.*, vol. 67, pp. 661–663, Aug 1991. [Online]. Available: https://link.aps.org/doi/10.1103/PhysRevLett.67.661

[113] X.-M. Jin, C.-Z. Peng, Y. Deng, M. Barbieri, J. Nunn, and I. A. Walmsley, "Sequential path entanglement for quantum metrology," *Scientific Reports*, vol. 3, no. 1, p. 1779, May 2013. [Online]. Available: https://doi.org/10.1038/srep01779

[114] D. Gottesman, T. Jennewein, and S. Croke, "Longer-baseline telescopes using quantum repeaters," *Phys. Rev. Lett.*, vol. 109, p. 070503, Aug 2012. [Online]. Available: https://link.aps.org/doi/10.1103/PhysRevLett.109.070503